論文 / 著書情報
Article / Book Information

題目(和文)	生体磁気計測に向けたダイヤモンド量子センサ
Title(English)	Diamond quantum sensors for biomagnetic field sensing
著者(和文)	西谷大祐
Author(English)	Daisuke Nishitani
出典(和文)	学位:博士(工学), 学位授与機関:東京工業大学, 報告番号:甲第12369号, 授与年月日:2023年3月26日, 学位の種別:課程博士, 審査員:波多野 睦子,中川 茂樹,宮本 恭幸,小寺 哲夫,岩﨑 孝之
Citation(English)	Degree:Doctor (Engineering), Conferring organization: Tokyo Institute of Technology, Report number:甲第12369号, Conferred date:2023/3/26, Degree Type:Course doctor, Examiner:,,,,
学位種別(和文)	博士論文
Type(English)	Doctoral Thesis

Diamond quantum sensors for biomagnetic field sensing

Daisuke Nishitani

March 1, 2023

Contents

List of Figures

List of Tables

Chapter 1

Introduction

1.1 Research Background

The number of vehicles produced in the world has been increasing steadily [1]. As the number of vehicles increases, there is a need to reduce environmental impact and traffic accidents. As shown in Figure 1, the number of fatalities from traffic accidents has been declining in developed countries, but the total number of fatalities is increasing in developing countries, where the market is growing [2, 3]. As a result, the market for advanced driving systems (ADAS) for driver safety and comfort has been growing in recent years. [4]. The driver monitor is a system that detects the driver's degree of concentration or doze-off based on the driver's facial expressions and displays warnings, etc., and is an important technology for ADAS systems. It is expected that autonomous driving will reduce the number of traffic accidents [5], but it will take time to spread because of the need to address technical issues (specific sensors, algorithms, etc.), reduce system costs, and develop infrastructure, etc. It is predicted that more than half of all registered vehicles will still require a driver to drive in 2040. [6].

Methods to reduce traffic accidents include vehicle periphery monitoring [7], driver sensing, and workload reduction [8]. An example of driver sensing technology is the commercialization of driver status monitors that recognize the driver's eyes and face to detect and warn of inattentiveness, look aside, and falling asleep at the wheel. Driving a car involves higher-order brain activity with information processes of cognition, judgment, and operation, and direct measurement of brain activity is ideal for driver sensing [9]. Sensing of brain activity can also detect in-vehicle comfort [10, 11] and the depth of occupant sleep [12]. Thus, this technology will remain

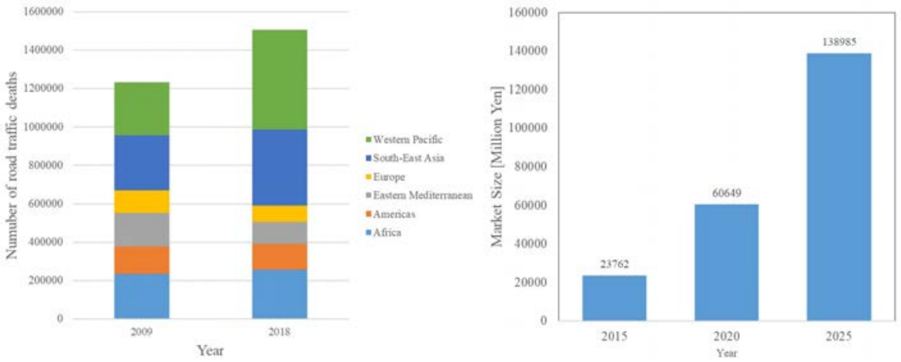

Figure 1.1: Number of traffic deaths by region and driver monitoring system market size. (a) Traffic fatalities are increasing in developing countries. (b) The market size of driver monitoring systems is expected to increase steadily.

necessary even when automated driving frees the driver from the wheel.

The following requirements are required for driver brain activity sensing

- Non-contact, non-binding sensing
- Real-time sensing
- Must be small enough to be installed in a car.

Brain activity sensing currently in use is based on contact or binding methods. Brain activity sensing in automobiles mainly uses Electro EncephaloGraphy (EEG) [13], which measures the potential generated by neural activity in the brain by contacting electrodes to the scalp, and Near-Infrared Spectroscopy (NIRS) [14], which measures the increase in hemoglobin caused by brain activity using near-infrared light, which is highly transparent to the body. In contrast to these methods, magnetoencephalography detects the magnetic field generated by neural activity in the brain and does not require the sensor to be in contact with the scalp. Since the magnetic permeability of a living body is constant regardless of the tissue, it is also advantageous in identifying areas of brain activity. However, the magnitude of magnetoencephalography is very small (sub-pT) [15], and sensors capable of detecting magnetoencephalography are limited. There are two types of sensors that can detect magnetoencephalograms: superconducting quantum interference devices (SQUIDs) that use superconducting Josephson junctions [16] and optically pumped atomic magnetometers (OPMs) that

Table 1.1: Sensor benchmark

	SQUID [22]	OPM [23]	NV
Operation condision	4.2 K	420 K	mK∼600 K
Sensitivity	$3\,\mathrm{fT}/\sqrt{\mathrm{Hz}}$	$<1\,\mathrm{fT}/\sqrt{\mathrm{Hz}}$	$15\,\mathrm{pT}/\sqrt{\mathrm{Hz}}$ [20]
Vector Imaging	–	–	✓
Linearlity	20 nT	3 nT	>10 mT [24–26]
Standoff distance	20 mm	6 mm	1 mm
Temporal resolution	$<$ ms	$<$ ms	$<$ ms
Sensor size	20 mm × 20 mm	12.4 mm× 16.6 mm× 24.4 mm	2mm× 2 mm× 0.2 mm

use optical pumping [17]. SQUIDs and OPMs are sensitive enough to detect magnetoencephalograms, but SQUIDs require cooling. SQUIDs require a magnetically shielded room because the sensor output saturates due to the limited magnetic flux allowed in the loop. On the other hand, OPM doesn't require cooling but for high sensitivity, the spin-exchange relaxation-free (SERF) condition, in which the relaxation due to spin-exchange collisions is negligible, must be maintained. NV centers in diamond have attracted much attention in recent years as magnetic sensors that can be operated at room temperature and have high spatial resolution, wide dynamic range, and high sensitivity [18, 19]. Although magnetic sensors using NV centers currently are not sensitive enough [20], theoretically they can achieve a sensitivity that can measure magnetoencephalography [21] and can be operated in an in-vehicle environment. The performance of these three sensors is shown in Table 1.1. We are considering the use of visual evoked magnetic field for brain activity sensing in automobiles. The requirements for magnetic sensors to measure visual evoked magnetic field are as follows.

- Magnetic sensitivity <1pT/√Hz
- Temporal resolution: 1 ms
- Spatial resolution: 1 cm or less
- Operating temperature -40°C to 80°C
- Linearity >10uT

1.2 Purpose of Research

The objective of this research is to construct a magnetic field measurement system that is robust against changes in the external environment, such as temperature, and suitable for long-term biological measurements, with the goal of monitoring the brain activity of drivers in automobiles. Conventional magnetic sensors using NV centers only detect the magnetic field generated when tissue extracted from a living body is stimulated. Therefore, as a feasibility study of biomagnetic measurement, we will construct a system to measure the cardiac magnetism of rats. The purpose of this measurement system is to identify issues and solutions for constructing a measurement system to stably measure biomagnetic fields over a long period of time. The objective is to solve these problems by analyzing and addressing noise factors that inhibit high sensitivity, and by providing feedback to temperature fluctuations that inhibit stable operation. In order to increase the sensitivity of magnetic sensors using NV centers, microwave antennas that match the measurement method are necessary. The conventional CW-ODMR method requires a large sensor volume to improve sensitivity. Therefore, we are developing antennas that can generate a uniform microwave magnetic field over a large volume. On the other hand, the Ramsey method, one of the pulse measurement methods that can achieve even higher sensitivity, requires the generation of a uniform and strong microwave magnetic field in the sensor volume. We will develop these microwave antennas using electromagnetic field analysis. Next, we aim to further increase the sensitivity for magnetoencephalography of small animals. In the conventional CW-ODMR method, sensitivity improvement is limited by optical and microwave broadening. The Ramsey method is a pulse measurement method that can fundamentally solve these problems, and combined with the microwave antenna mentioned above, it achieves a sensitivity of $10\,\mathrm{pT}/\sqrt{\mathrm{Hz}}$.

1.3 Research Outline

This thesis consists of five chapters.

Chapter 1 describes the importance of monitoring drivers, especially brain activity, in response to the current situation where traffic accidents in the automobile industry are not decreasing. In contrast to EEG and NIRS, which are used to monitor brain activity in automobiles, this thesis describes the potential of magnetoencephalography, which can monitor brain activity without contact and without binding. The magnitude of magnetoencephalography is very small (sub-pT), and expectations for NV centers that can detect magnetoencephalography in the automotive environment are discussed.

In Chapter 2, the theoretical background of the NV center in diamond and the noise sources in the actual measurement environment are summarized. The magnetic sensitivity of NV centers is determined by the theoretical limiting sensitivity and the magnitude of noise sources. Noise sources that interfere with the theoretical limiting sensitivity are organized and their countermeasures are summarized.

Chapter 3 describes the biomagnetic measurement system. In previous research, we have only removed tissue from a living body and detected the magnetic field produced by the response of the tissue to external stimuli. Therefore, we aimed to construct a system that can stably measure the cardiac magnetism of rats over a long period of time while keeping the living body alive. We achieved high sensitivity by combining the CW-ODMR method, a quantum protocol using energy level difference, with lock-in measurement and differential measurement. The biological temperature control system to maintain the living body slowly changes the temperature around the NV center and provides temperature noise. The slow temperature change was canceled by combining temperature feedback, resulting in a sensitivity of $140\,\mathrm{pT}/\sqrt{\mathrm{Hz}}$ and successful rat magnetocardiographic measurements and rat magnetocardiographic imaging. The influence of optical and microwaves on the CW-ODMR method is explained, and the effectiveness of increasing the sensor volume to improve sensitivity is described: an antenna capable of irradiating a uniform microwave field in a sensor volume of $1\,\mathrm{mm}^3$ is proposed and its evaluation results are presented.

Chapter 4 describes the design of the microwave antenna required to make the NV Center operate as a magnetic sensor. The Ramsey method with Double Quantum requires a strong, uniform, broad-band microwave field in the volume of the diamond used as the sensor. We found a inverted T-shaped antenna that could meet these requirements and confirmed that it could perform the Rabi measurements required for Double Quantum operation. Using this antenna, we constructed a measurement system to apply Double Quantum to the Ramsey method with a view to detecting magnetoencephalography. The Ramsey method overcomes the optical and microwave broadening that hinders the high sensitivity of CW-ODMR by temporally separating the optical excitation and readout by laser and the spin operation. In the conventional Ramsey method, measurement is performed using a high-speed digitizer, and the time variation of the fluorescence signal at the NV center is acquired for post-processing. Therefore, this method is not suitable for long-time and real-time measurements. In addition, the spin-state-dependent fluorescence of the NV center has an offset, which reduces the resolution of the spin-state-dependent fluorescence relative to the actual resolution of the Digitizer. Therefore, the combination of a lock-in measurement that detects only the AC signal makes it possible to detect the magnetic field in real time while maintaining the resolution. We succeeded in detecting the magnetic field in real time using this method.

Chapter 5 provides a summary and outlook of this thesis.

Chapter 2

Principles

2.1 Magnetic sensor with ensemble NV^- center

Quantum sensors are a method of measuring physical quantities using quantum phenomena [27]. The behavior based on quantum pheonomena is tied to physical constants, and its sensitivity can reach fundamental limits [21]. For these reasons, quantum sensors are being applied not only to fundamental science, but also to applied science and industry. Recently, magnetic sensors based on nitrogen-vacancy (NV^-) color centers in diamond have attracted much interest. The use of electron spins in NV centers to act as magnetic field sensors was proposed in 2008 and realized in a single NV center. The following year, it was realized in an ensemble NV center. Since then, there has been a lot of research on magnetic field sensors using NV centers. In the field of high-sensitivity magnetic field sensors, a detection of action potential of a single neuron using an ensemble NV center has been reported. In addition, a vector sensing of magnetic fields by using NV centers in four different directions has been reported.

2.2 Nitrogen Vacancy center physics

2.2.1 Structure of Nitrogen Vacancy center

NV centers have a structure in which nitrogen atoms replace carbon atoms in the diamond, and the adjacent carbon atoms become vacancies. The NV center can take four orientations depending on how the nitrogen and vacancies are arranged. Figure 2.1 shows the structure of NV centres in diamond crystals and the direction of the NV axis that NV centres can

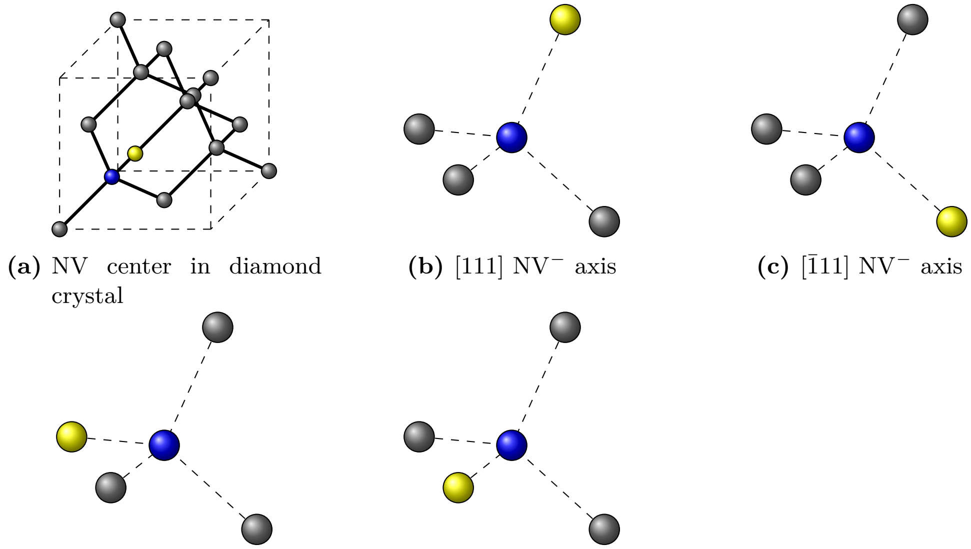
(a) NV center in diamond crystal **(b)** [111] NV$^-$ axis **(c)** [$\bar{1}$11] NV$^-$ axis **(d)** [1$\bar{1}$1] NV$^-$ axis **(e)** [1$\bar{1}$1] NV$^-$ axis

Figure 2.1: NV center strucure. Structure of NV centre in diamond crystals. The blue circles are vacancies and the yellow circles are nitrogen. NV centre can have axes in four directions.

take. The NV center takes the states of NV$^+$, which is positively charged, NV^0, which is electrically neutral, and NV$^-$, which is negatively charged. Since we only deal with the negatively charged state from now on, NV$^-$ is called NV or NV center.

2.2.2 Ground state Hamiltonian

The ground state Hamiltonian can be expressed as

$$H_{gs}/h = S \cdot \boldsymbol{D} \cdot S + S \cdot \boldsymbol{A} \cdot I + I \cdot \boldsymbol{Q} \tag{2.1}$$

where h is plank constant and S is electronic operator and I is nuclear spin operator. $\boldsymbol{D}$ is electron spin-spin interaction with fine structure tensor, $\boldsymbol{A}$ is electron nuclear interaction with hyper tensor, $\boldsymbol{Q}$ is nuclear electric quadruple interaction with quadruple tensor. NV center has C_{3v} symmetry, ground state Hamiltonian is expressed as [28],

$$H_{gs} = D(T)\hat{S}_z^2 + A_{\parallel}\hat{S}_z\hat{I}_z + A_{\perp}(\hat{S}_x\hat{I}_x + \hat{S}_y I_y) + P\hat{I}_z^2 \tag{2.2}$$

$D(T)$ is $m_s = 0$ and $m_s = \pm 1$ energy seperation called zero field splitting. In room temperature the value of $D(T) \approx 2.87$ GHz and it has temperature dependence $dD/dT = -74$ kHz/°C [29]. An additional hyperfine splitting $A_{\|}\hat{S}_z\hat{I}_z$ is due to nitrogen nuclear spin. $I = 1$, $A_{\|} \approx -2.14$MHz for ^{14}N and $I = 1/2$, $A_{\|} \approx -3.03$ MHz for ^{15}N [30, 31]. Transverse hyperfine coupling are $A_{\perp} = 2.70$ MHz for ^{14}N and $A_{\perp} = 3.65$ MHz for ^{15}N. While ^{14}N has an axial quadrupole coupling $P_{\|} = -5.01$ MHz, but ^{15}N has not [30–32].

With external magnetic field $\boldsymbol{B} = B_x, B_y, B_z$, NV$^-$ Hamiltonian Zeeman interaction terms are,

$$H_{zeeman}/h = \frac{g_e\mu_B}{h}(B_z\hat{S}_z + B_x\hat{S}_x + B_y\hat{S}_y) \tag{2.3}$$

where $g_e \approx 2.003$ is the NV$^-$ electronic g-factor and $\mu_B = 9.24 \times 10^{-24}$ J/T is the Bohr magneton. Crystal stress Hamiltonian terms are [33–36],

$$\begin{aligned} H_{stress}/h = M_z\hat{S_z}^2 + M_x(S_x^2 + S_y^2) + M_y(S_xSy + S_yS_x)+ \\ N_x(S_xS_z + S_zS_x) + N_y(S_yS_z + S_zS_y) \end{aligned} \tag{2.4}$$

Electric fields Hamiltonian terms are [37],

$$H_{electric}/h = d_{\|}E_zS_z^2 - d_{\perp}E_x(S_x^2 - S_y^2) + d_{\perp}E_y(S_xS_y + S_yS_x) \tag{2.5}$$

where M_z, M_x, M_y, N_x, N_y are spin strain coupling parameters. Electric dipole moments are $d_{\|} = 3.5 \times 10^{-3}$ Hz/(V/m) (axial) and $d_{\perp} = 0.17$ Hz/(V/m) (transverse) [33, 35, 38, 39]. The addition of these Hamiltonian terms results in the ground state Hamiltonian, which is shown below

$$\begin{aligned} H_{total}/h = D(T)\hat{S}_z^2 + A_{\|}\hat{S}_z\hat{I}_z + A_{\perp}(\hat{S}_x\hat{I}_x + \hat{S}_yI_y) + P\hat{I}_z^2 \\ + \frac{g_e\mu_B}{h}(B_z\hat{S}_z + B_x\hat{S}_x + B_y\hat{S}_y) \\ + M_z\hat{S}_z + M_x(S_x^2 + S_y^2) + M_y(S_xSy + S_yS_x) \\ + N_x(S_xS_z + S_zS_x) + N_y(S_yS_z + S_zS_y) \\ + d_{\|}E_zS_z^2 - d_{\perp}E_x(S_x^2 - S_y^2) + d_{\perp}E_y(S_xS_y + S_yS_x) \end{aligned} \tag{2.6}$$

The Hamiltonian and its eigenstates can be simplified if D is sufficiently large relative to the other terms. If the transverse magnetic fields B_x, B_y and the spin strain coupling parameter N_x, N_y are small compared to D and the magnetic field is non-zero, the contributions of the transverse electric field and the transverse strain E_x, E_y and M_x, M_y in the magnetic field along the NV symmetry axis are suppressed and for magnetic fields above a few Gauss, these terms are neglected in the Hamiltonian. The magnetic field along the symmetry axis is suppressed. The spin resonances between the

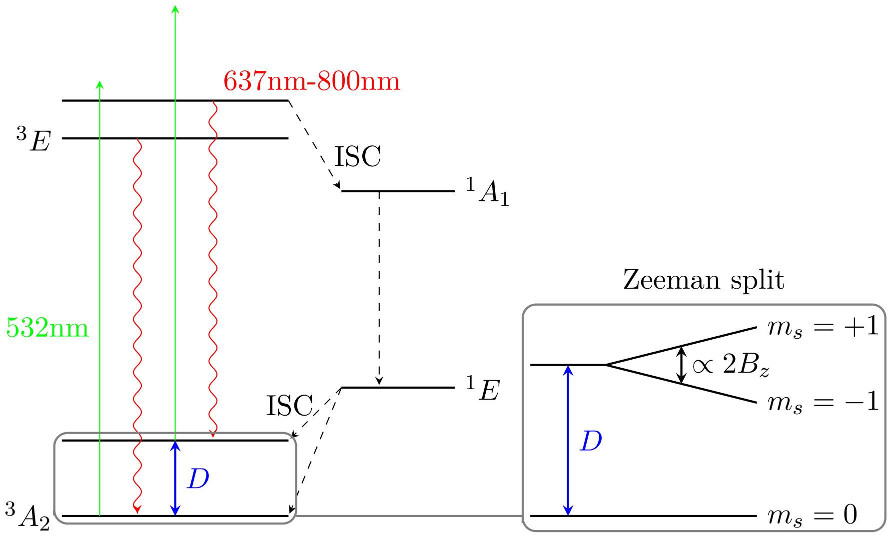

Figure 2.2: NV$^-$ center Energy Level Diagram

$m_s = 0$ and $m_s = \pm 1$ eigenstates in the above simplified Hamiltonian are shown below.

$$\nu_{\pm} = (D + M_z + d_{\parallel} E_z) \pm \frac{g_e \mu_B}{h} B_x \tag{2.7}$$

By irradiating microwave frequencies near the resonance frequency and monitoring the fluorescence from diamond, changes in the magnetic field can be detected by changes in the fluorescence. Also, by monitoring both the upper and lower resonance frequencies, it is possible to separate the changes in D, M_z, E_z and the magnetic field.

2.2.3 Energy levels and transition paths of NV centers

The energy levels of NV centers and their transition paths are shown below. The electron spin state of an NV center can be readout by the intensity of red fluorescence from the NV center. This method of reading out the electron spin state by light is called optical detection magnetic resonance (ODMR), and even a single electron spin can be detected. As shown in the figure 2.2, there are excitation, radiation, and non-radiation processes [40]. Electron spins in the ground triplet are excited by green light. Since the spin is conserved in this excitation process, the spin of $m_s = 0$ in the ground state is transferred to $m_s = 0$ in the excited state, and $m_s = \pm 1$ in the ground state is transferred to the transition to $m_s = \pm 1$ in the excited state. A 532 nm laser is commonly used as a green light source. Next, the relaxation process from the excited state to the ground state is described. There are two types of relaxation processes: direct transition with red fluorescence and indirect transition with invisible infrared radiation (non-radiation process). In the direct transition, the spin state is conserved as in the case of excitation by green light. As shown in the figure, the spectrum of red fluorescence from the direct transition has a sharp peak at 637 nm called the zero-phonon line. Between 637 nm and 800 nm of the zero-phonon line, a gentle spectral peak called the phonon sideband is observed. Next, we will discuss the non-radiative process. Non-radiative processes have different transition probabilities depending on the spin state. In this transition, the excited state relaxes from the triplet to the singlet, emits infrared radiation, and relaxes to the ground triplet. This transition from triplet to singlet is called intersystem crossing (ISC) [41, 42], and the $m_s = \pm 1$ state of the excited triplet tends to transition to the singlet. And from the singlet, only the ground state triplet $m_s = 0$ transitions.

2.2.4 Electron spin initialization and readout of NV centers

The initialization of the electron spin of the NV center is to set $m_s = 0$ in the ground state triplet. If the electron spins of the NV center are in the ground state $m_s = 0$ before initialization, they are excited by green laser irradiation and emit red fluorescence, corresponding to a direct transition. This process is a spin-conserving process and returns to the ground state $m_s = 0$. On the other hand, when in the ground state $m_s = \pm 1$, it is excited by green laser irradiation and emits red light while conserving spin, and after relaxing to singlet, it emits infrared light and relaxes to the ground triplet $m_s = 0$. This transition is also called radiation-free and corresponds to an indirect transition. Thus, with continued green laser irradiation, spins in the ground state $m_s = \pm 1$ gradually transition to the $m_s = 0$ state and are eventually initialized to $m_s = 0$ [43].

The readout of electron spins can be detected by irradiating light. This is based on the fact that the transition process differs depending on which ground state the electron spins are in, as mentioned earlier. In the case of the ground state $m_s = \pm 1$, the emission intensity is weaker than in the ground state $m_s = 0$ due to the occurrence of direct and indirect transitions. Furthermore, the transition rate of the indirect transition is lower than that of the direct transition. The lower transition rate of the indirect transition results in a contrast in luminescence intensity of about 30%. In other words, when irradiated with light, the NV center spin state can be read based on the luminescence intensity: $m_s = 0$ state if the luminescence intensity is high, $m_s = -1$ state if the luminescence intensity is low, and so on. The spin state of the NV center can be readout based on the luminescence intensity. If the initialized state is left without any action, the NV center relaxes to a thermal equilibrium state in which each spin state of the ground state ($m_s = 0, -1, +1$) is equally distributed due to the interaction with phonons. This relaxation time is called spin relaxation time T_1 and is a few ms at room temperature.

2.3 Magnetic Field Measurement Methods Using NV Centers

In ground field measurement using NV centers, the appropriate measurement method differs depending on the type of magnetic field to be measured. Here, we explain the sensing method for relatively slow magnetic fields (DC 100kH) such as those of living organisms. The Hahn echo method and other methods for detecting AC magnetic fields that fluctuate at high speeds are known, but are not described here.

Measurement methods suitable for biomagnetic measurement Magnetic fields generated by a living body or other objects change slowly in time and fluctuate with a frequency bandwidth. There are several methods for detecting such magnetic fields, including continuous wave (CW)-ODMR, pulsed ODMR, and the Ramsey method.

2.3.1 Theoretical Sensitivity

Quantum sensors such as NV centers are classified into the following three levels depending on the method of measuring physical quantities [27].

1. Using energy level differences
2. Using quantum coherence
3. Using entanglement

These measurement methods determine the theoretical magnetic sensitivity of the NV center. The theoretical sensitivities calculated for different measurement methods using the same NV center are shown in Figure 2.3. The theoretical sensitivity limit corresponding to level 1 in Figure 2.3 is the shot noise limit. The measurement method corresponding to this level is called the continuous wave optically detected magnetic resonance (CW-ODMR)

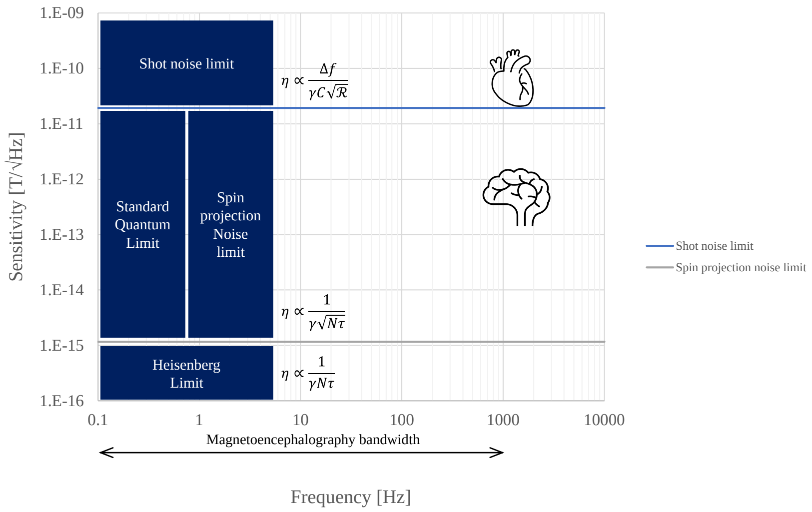

Figure 2.3: Theoretical Limit Sensitivity of Magnetic Sensor Measurement Methods Using NV Center. The limiting sensitivity was calculated under the following conditions: $\gamma = 2.8 \times 10^{10}\,\mathrm{T/Hz}$, $\Delta f = 2.8 \times 10^{6}\,\mathrm{Hz}$, $C = 1.2 \times 10^{-2}$, $R = 1.9 \times 10^{18}\,\mathrm{s}^{-1}$, $N = 1.5 \times 10^{13}$, $\tau = 4.0 \times 10^{-7}\,\mathrm{s}$.

method. The theoretical sensitivity limit corresponding to level 2 is the spin projection limit. This is called the Standard Quantum Limit (SQL). The theoretical limit sensitivity corresponding to level 3 is the Heisenberg limit. η in the figure is the theoretical equation for each limit sensitivity [44]. It can be seen that a magnetic sensor using NV centers can theoretically achieve the sensitivity to measure magnetoencephalography using the level 2 measurement method. However, this value is only a theoretical limit of sensitivity, and when it operates as a magnetic sensor, the sensitivity is the superimposed effect of noise on this value.

2.3.2 CW ODMR

CW-ODMR has a simple experimental setup and is widely used in magnetic field measurements. In CW-ODMR, optical initialization, readout, and microwave fields occur simultaneously.

Laser excitation keeps polarizing the NV center to the $m_s = 0$ ground state. As the MW frequency approaches the resonance frequency of the NV center, a transition to $m_s = \pm 1$ occurs and the light generated decreases. A change in the magnetic field changes the resonance frequency of the NV centres, which leads to a change in the detected fluorescence. The magnetic

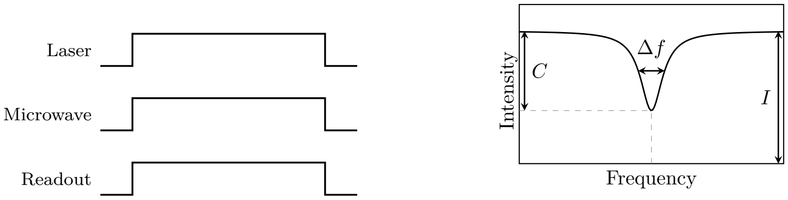

(a) CW-ODMR protocol **(b)** CW-ODMR waveform

Figure 2.4: CW-ODMR protocol and waveform

field is sensed by monitoring this change in detected fluorescence. Figure2.4 shows the laser, microwave, and readout protocols and waveforms for CW-ODMR.

Although the CW-ODMR method is easier to implement than pulse measurements such as the Ramsey method, it is not the optimal method in terms of high sensitivity for several reasons. First of all, CW-ODMR is affected by optical and microwave power broadening, which reduce contrast and increase line width, thereby reducing sensitivity. Second, it is not possible to apply pulse techniques that improve sensitivity, such as double quantum magnetometry, P1 decoupling, and many other techniques that improve readout fidelity. The optimal CW-ODMR sensitivity is where optical excitation, microwave drive, and T_2^* dephasing contribute roughly equally to the ODMR linewidth.

2.3.3 Rabi

Two level system of spin $m_s = 0, -1$ can be used for sensing. The state of the two-level system can be expressed using the Bloch sphere. Figure2.5 shows the laser, microwave, and readout protocols and waveforms for Rabi.

$$|\psi\rangle = \cos\left(\frac{\theta}{2}\right)|0\rangle + \exp^{i\phi}\sin\left(\frac{\theta}{2}\right)|-1\rangle \tag{2.8}$$

where θ, ϕ are angular coordinates on the Bloch sphere. The Hamiltonian can be expressed in terms of Zeeman terms.

$$H_{gs} = \omega_0 S_z \tag{2.9}$$

where $\omega_0 = D - \gamma B_z$ is the resonance frequency. The time evolution of the two level system is as follows,

$$|\psi(t)\rangle = \cos\left(\frac{\theta}{2}\right)|0\rangle + \exp^{i(\phi_0-\omega_0 t)}\sin\left(\frac{\theta}{2}\right)|-1\rangle \tag{2.10}$$

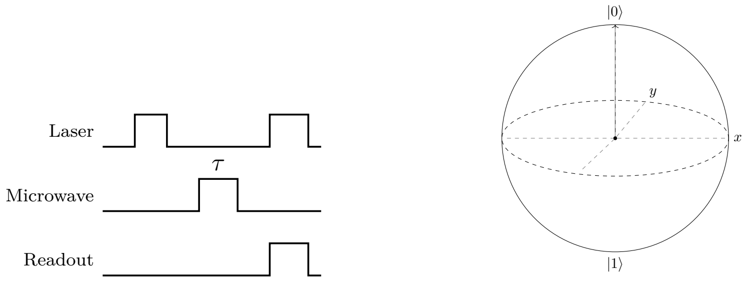

(a) Sequence **(b)** Initialization

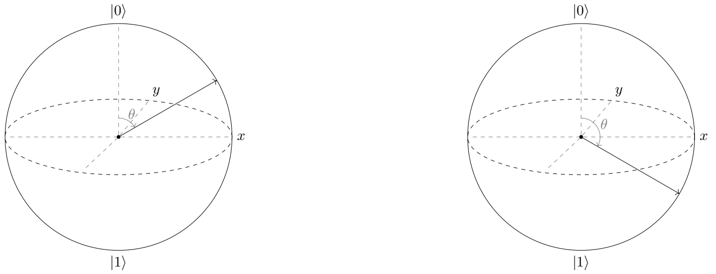

(c) Short microwave irradiation time τ **(d)** Long microwave irradiation time τ

Figure 2.5: Rabi Sequence and Bloch sphere imaging. (a)Temporal behaviour of laser, microwave and readout in Rabi sequences. (b)Spin initialisation by laser. (c)Short microwave irradiation times. (d)Long microwave irradiation times.

The magnetic field of a typical microwave can be regarded as the sum of clockwise and counterclockwise magnetic fields. In the rotating wave approximation, only one of them is considered and the other can be neglected. The rotating wave approximation is valid as long as the Larmor frequency is much larger than the Rabi frequency. In the rotational approximation, the magnitude of the microwave field is constant and the spin rotates around the x-axis of the Bloch sphere. This phenomenon is called Rabi oscillation. The time evolution of the Rabi oscillation is as follows.

$$|\psi(t)\rangle = \frac{1+\exp^{(-i\omega_1 t)}}{2}|0\rangle + \frac{1-\exp^{(-i\omega_1 t)}}{2}|1\rangle \tag{2.11}$$

The spin state can be read from the fluorescence of the diamond, and the amount of fluorescence is proportional to the transition probability.

$$S(t) = |\langle 0 \,|\, \psi(t)\rangle|^2 = Aexp\left(-\frac{t}{T_{\mathrm{R}}}\right)\cos(2\pi f_{\mathrm{rabi}} t) + B \tag{2.12}$$

where f_{rabi} is the Rabi frequency and T_{R} is the Rabi decay time constant. The length of 1/4 of the period of the Rabi oscillation relative to the length of the microwave pulse corresponds to a superposition of $|0\rangle$ and $|1\rangle$ and is called a $\pi/2$ pulse. The length of 1/2 of the period causes a transition from $|0\rangle$ to $|1\rangle$ and is called a π pulse.

2.3.4 Pulsed ODMR

The Pulsed ODMR technique partially removes the broadening effect of the CW-OMDR technique by temporally separating the laser and microwave irradiation. In the Pulsed ODMR protocol, a pulse of laser initializes the spin state to $m_s = 0$. Next, a microwave pulse transitions the spin state to $m_s = \pm 1$. Finally, the transition state is read out by irradiating an laser pulse. When the magnetic field changes, the resonance frequency of the NV center shifts and the microwave π pulse becomes incomplete, changing the number of spins that transition to $m_s = \pm 1$. The trend detected during readout with laser pulses changes. The Pulsed ODMR technique under optimal conditions can measure close to the T_2^* limit.

2.3.5 Ramsey

The Ramsey technique measures electron spins in a superposition state by accumulating a magnetic field as a phase. In the Ramsey protocol, the spin state is first initialized to $m_s = 0$ by irradiating a green laser pulse. Next, microwaves at the NV center resonance frequency are irradiated at $\pi/2$ to prepare a superposition of $m_s = 0$ and $m_s = -1$ spin states. ($m_s = +1$ depending on the frequency used). If the effect of the transverse magnetic field is sufficiently smaller than the zero-field splitting, the Hamiltonian of the two-level system is as follows [44, 45],

$$\begin{aligned} H &= (2\pi D + \gamma_e B)S_z \\ &= \frac{\hbar}{2}\begin{pmatrix} 2\pi D + \gamma_e & 0 \\ 0 & -2\pi D - \gamma_e B \end{pmatrix} \end{aligned} \tag{2.13}$$

where S_z is the spin operator for the projection in the z direction; $B = B_0 + B_{\text{sense}}$ is the total magnetic field projected along the NV axis. The resonance frequency due to the bias magnetic field is $\omega_0 = 2\pi D + \gamma_e B_0$. The spin operator S_z is expressed in terms of a Pauli matrix as follows.

$$H = \frac{\hbar\omega_0}{2}\sigma_z + \frac{\hbar}{2}\gamma_e B_{\text{sense}}\sigma_z \tag{2.14}$$

The superposition state by $\pi/2$ pulses is achieved by a microwave magnetic field perpendicular to the NV axis. This microwave field $B_1 \cos(\omega t)$ is polarized along the y-axis, and the angular frequency is $\omega \approx \omega_0$. Since $B \gg B_{\text{sense}}$ in general, the second term in the above equation can be ignored. Therefore, the Hamiltonian of the Rabi oscillation in this microwave is shown below.

$$\begin{aligned} H_{\text{rabi}} &= \frac{\hbar\omega_0}{2}\sigma_z + \frac{\hbar}{2}\gamma_e B_1 \cos(\omega t)\sigma_y \\ &= H_0 + H_1 \end{aligned} \tag{2.15}$$

where $H_0 = \frac{\hbar\omega_0}{2}\sigma_z$ and $H_1 = \frac{\hbar}{2}\gamma_e B_1 \cos(\omega t)\sigma_y$. When converted to the rotational frame at angular frequency ω_0, the time evolution is expressed using H_1 as follows.

$$\begin{aligned} \tilde{H} &= U_0^\dagger(t) H_1 U_0(t) \\ &= \frac{\hbar}{4}\gamma_e B_1 \begin{pmatrix} 0 & -i(e^{-i(\omega_0+\omega)t} + e^{-i(\omega_0-\omega)t}) \\ i(e^{i(\omega_0-\omega)t} + e^{i(\omega_0+\omega)t}) & 0 \end{pmatrix} \end{aligned} \tag{2.16}$$

If $\omega = \omega_0$ and the rotational wave approximation is performed, the term $2\omega_0$ can be neglected and the following is obtained.

$$H_1 = \frac{\hbar}{4}\gamma_e B_1 \sigma_y \tag{2.17}$$

The state vector ψ after irradiation of microwaves of $\pi/2$ pulse length is expressed as follows.

$$\begin{aligned}
\left|\tilde{\psi}(\tau_{\frac{\pi}{2}})\right\rangle &= \exp\left(-i\frac{\gamma_e B_1 \sigma_y \tau_{\frac{\pi}{2}}}{4}\right)\left|\tilde{\psi}(0)\right\rangle \\
&= \exp\left(-i\frac{\pi}{4}\sigma_y\right)|0\rangle \\
&= \frac{1}{\sqrt{2}}\begin{pmatrix}1 & -1\\ 1 & 1\end{pmatrix}\begin{pmatrix}0\\ 1\end{pmatrix} \\
&= \frac{1}{\sqrt{2}}(-|-1\rangle + |0\rangle)
\end{aligned} \tag{2.18}$$

There is no microwave magnetic field during the free precession time τ after the $\pi/2$ pulse. Therefore, the new Hamiltonian determined by B_{sense} becomes

$$H_1' = \frac{\hbar}{2}\gamma_e B_{\text{sense}} \sigma_z \tag{2.19}$$

The state vector after free precession time τ is expressed as follows,

$$\begin{aligned}
\left|\tilde{\psi}(\tau_{\frac{\pi}{2}} + \tau)\right\rangle &= e^{-iH_1'\tau/\hbar}\left|\tilde{\psi}(\tau_{\frac{\pi}{2}})\right\rangle \\
&= \frac{1}{\sqrt{2}}(-e^{-i\frac{\phi}{2}}|-1\rangle + e^{i\frac{\phi}{2}}|0\rangle)
\end{aligned} \tag{2.20}$$

where $\phi = \gamma_e B_{\text{sense}}\tau$ is the phase accumulation caused by B_{sense}.

Considering the last $\pi/2$ pulse of the Ramsey sequence in the same way as the first $\pi/2$ pulse, the Hamiltonian becomes,

$$\tilde{H}_1'' = \frac{\hbar}{4}\gamma_e B_2(\cos(\theta)\sigma_y - \sin(\theta)\sigma_x) \tag{2.21}$$

where the microwave field is B_2 and the polarization of the microwave field is θ out of phase with the x-y plane relative to the first microwave field. The state vector is,

$$\begin{aligned}
\left|\tilde{\psi}(\tau_{\frac{\pi}{2}} + \tau + \tau_{\frac{\pi}{2}})\right\rangle &= e^{-i\tilde{H}_1''\tau_{\frac{\pi}{2}}/h}\left|\tilde{\psi}(\tau_{\frac{\pi}{2}} + \tau)\right\rangle \\
&= \frac{1}{\sqrt{2}}\begin{pmatrix}1 & -e^{-i\theta}\\ e^{i\theta} & 1\end{pmatrix}\cdot\frac{1}{\sqrt{2}}\begin{pmatrix}-e^{-\frac{i\phi}{2}}\\ e^{\frac{i\phi}{2}}\end{pmatrix}
\end{aligned} \tag{2.22}$$

To rearrange the equation,

$$\left|\tilde{\psi}\right\rangle = \cos\left(\frac{\phi-\theta}{2}\right)\left|-1\right\rangle - ie^{i\theta}\sin\left(\frac{\phi-\theta}{2}\right)\left|0\right\rangle \tag{2.23}$$

The accumulated phase is transferred to the occupancy difference between the $|0\rangle$ and $|-1\rangle$ states. This accumulated phase can be obtained by measuring the observable $\tilde{S}_z$.

$$\begin{aligned}\left\langle \tilde{S}_z \right\rangle &= \frac{\hbar}{2}\left\langle \tilde{\psi} \middle| \sigma_z \middle| \tilde{\psi} \right\rangle \\ &= \frac{\hbar}{2}\left(\cos^2(\frac{\phi-\theta}{2}) - \sin^2(\frac{\phi-\theta}{2})\right) \\ &= \frac{\hbar}{2}\cos(\phi-\theta) \\ &= \frac{\hbar}{2}\cos(\gamma_e B_{\mathrm{sense}}\tau - \theta)\end{aligned} \tag{2.24}$$

The spin state is measured by the spin-dependent fluorescence of the NV center in the second laser pulse. Sweeping the free precession time, we obtain Ramsey oscillations that decay determined by T_2^* while oscillating at a frequency determined by tuning between the resonant frequency of the NV center and the microwave frequency pulse given. This decay time T_2^* corresponds to the natural linewidth Γ, if a Lorentzian waveform is assumed, $T_2^* = (\pi\Gamma)^{-1}$. The sequence and Bloch sphere imaging for Ramsey measurements are shown in Figure 2.6a - 2.6e. When the magnetic field is changed with T_2^* fixed, the detected NV fluorescence oscillates, and this oscillation is called the DC magnetic field curve. The steepest slope of this curve is the most sensitive point of the Ramsey method.

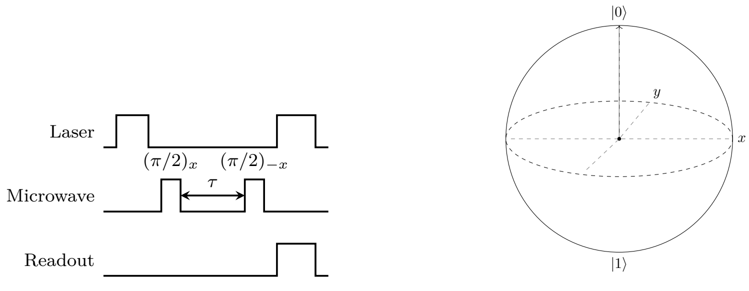

(a) Sequence **(b)** Initialization

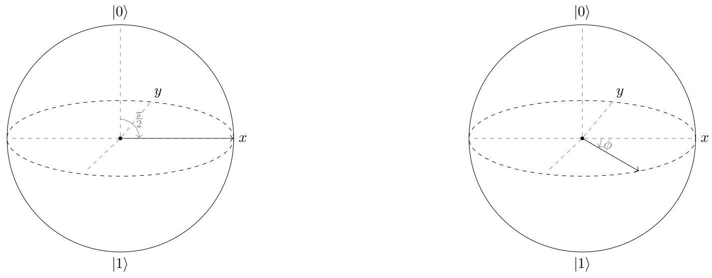

(c) $\pi/2$ pulse **(d)** Free precession time τ

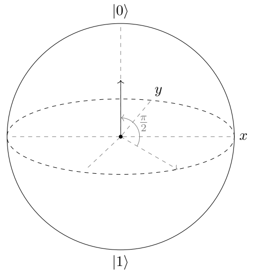

(e) Readout

Figure 2.6: Ramsey Sequence and Bloch sphere imaging. (a)Temporal behaviour of laser, microwave and readout in Ramsey sequences. (b)Spin initialisation by laser. (c)Superposition by $\pi/2$ pulses. (d)Phase accumulation by the free precession time. (e)Spin readout by $\pi/2$ pulse and laser.

2.3.6 Double Quantum Rabi

The Rabi in section 2.3.3 are $|0\rangle \leftrightarrow |1\rangle$ or $|0\rangle \leftrightarrow |-1\rangle$ transitions and are called Single Quantum (SQ) Rabi. Double Quantum (DQ) uses both $|1\rangle$ and $|-1\rangle$ states, but microwave field irradiation cannot directly cause $|1\rangle$ and $|-1\rangle$ transitions. Therefore, the DQ Rabi can be performed by applying the respective SQ Rabi, $|0\rangle \leftrightarrow |1\rangle$ and $|0\rangle \leftrightarrow |1\rangle$, simultaneously. Consider DQ Rabi in a three-level system with $|0\rangle$, $|+1\rangle$, and $|-1\rangle$ states. The Hamiltonians for the each SQ Rabi frequency as Ω_{+1} and Ω_{-1} and the each detuning as δ_{+1} and δ_{-1} are as follows [46].

$$\begin{aligned} H_{\mathrm{DQRabi}}/h = -\delta_{+1}\left|+1\right\rangle\left\langle+1\right| - \delta_{-1}\left|-1\right\rangle\left\langle-1\right| - \frac{\Omega_{+1}}{\sqrt{2}}(\left|+1\right\rangle\left\langle 0\right| + \left|0\right\rangle\left\langle+1\right|) \\ - \frac{\Omega_{-1}}{\sqrt{2}}(\left|-1\right\rangle\left\langle 0\right| + \left|0\right\rangle\left\langle-1\right|) \quad (2.25) \end{aligned}$$

Introducing the following states $D = \frac{1}{\sqrt{2}}(|+1\rangle + |-1\rangle)$ and $B = \frac{1}{\sqrt{2}}(|+1\rangle - |-1\rangle)$ to simplify the Hamiltonian, Equation 2.25 follows.

$$\begin{aligned} H_{\mathrm{DQRabi}}/h = -\frac{\delta_{+1}+\delta_{-1}}{2}(\left|B\right\rangle\left\langle B\right| + \left|D\right\rangle\left\langle D\right|) - \frac{\delta_{+1}-\delta_{-1}}{2}(\left|B\right\rangle\left\langle D\right| + \left|D\right\rangle\left\langle B\right|) \\ - \frac{\Omega_{+1}+\Omega_{-1}}{2}(\left|B\right\rangle\left\langle 0\right| + \left|0\right\rangle\left\langle B\right|) - \frac{\Omega_{+1}-\Omega_{-1}}{2}(\left|D\right\rangle\left\langle 0\right| + \left|0\right\rangle\left\langle D\right|) \quad (2.26) \end{aligned}$$

A good notation should be $\delta_{\mathrm{com}} = \frac{\delta_{+1}+\delta_{-1}}{2}$ and $\delta_{\mathrm{diff}} = \frac{\delta_{+1}-\delta_{-1}}{2}$ a reasonable (implicit) assumption should have been $\Omega_{+1} \approx \Omega_{-1}$ so $\Omega_{+1} - \Omega_{-1}$ was ignored. As a result,

$$\begin{aligned} H_{\mathrm{DQRabi}}/h \sim -\delta_{\mathrm{com}}(\left|B\right\rangle\left\langle B\right| + \left|D\right\rangle\left\langle D\right|) - \delta_{\mathrm{diff}}(\left|B\right\rangle\left\langle D\right| + \left|D\right\rangle\left\langle B\right|) \\ - \Omega_{\pm 1}(\left|B\right\rangle\left\langle 0\right| + \left|0\right\rangle\left\langle B\right|) \quad (2.27) \end{aligned}$$

Thus, the Rabi frequency for the oscillation within the two-level system composed of $\langle 0|$ and $|B\rangle$ states should be $\Omega_{\mathrm{DQ}} = 2\Omega_{\pm 1}$. This relates to $\Omega_{\mathrm{SQ}} = \sqrt{2}\Omega_{\pm 1}$ given above as $\Omega_{\mathrm{DQ}} = \sqrt{2}\Omega_{\mathrm{SQ}}$.

If the detuning were not zero($\delta_{+1} = \delta_{-1} \neq 0$) here, the oscillations of the $|0\rangle$ and $|D\rangle$ states would remain. The Rabi frequency in this case is $\Omega_{\mathrm{DQ}}/2$. The Fourier transform of the Rabi oscillation shows a peak at half the DQ Rabi frequency.

2.3.7 Double Quantum Ramsey

As shown in Section 2.3.5, SQ creates the superposition state $\frac{1}{\sqrt{2}}(|0\rangle + |1\rangle)$ or $\frac{1}{\sqrt{2}}(|0\rangle + |-1\rangle)$ by adding a $\pi/2$ pulse [46]. Similarly, the DQ creates the superposition state $\frac{1}{\sqrt{2}}(|+1\rangle + |-1\rangle)$. This means a transition from state $|0\rangle$ to state $|B\rangle$ in DQ Rabi. Therefore, unlike SQ Ramsey, the sequence in DQ Ramsey uses a π pulse, which is $\sqrt{2}$ times the $\pi/2$ pulse in SQ Rabi, since $\Omega_{DQ} = \sqrt{2}\Omega_{SQ}$ for equal SQ Rabi frequencies.

2.4 Magnetic Field Sensitivity

The detection limit field is the smallest change in magnetic field intensity that can be detected in the measurement. When considering sensor performance, the total measurement time of the measurement must be taken into account. The magnetic field sensitivity is proportional to the square root of the number of photons detected. The number of photons detected is proportional to time. Taking into account the measurement time, the sensitivity is expressed as $\eta = \delta B/\sqrt{t_{\text{measure}}}$. where the units are $T/\text{Hz}^{-1/2}$ and t_{measure} is the total measurement time.

2.4.1 CW-ODMR sensitivity

The shot noise limit sensitivity of CW-ODMR is [47]

$$\eta_{CW} = \frac{4}{3\sqrt{3}} \frac{h}{g_e \mu_B} \frac{\Delta\nu}{C_{CW}\sqrt{R}} \tag{2.28}$$

where R is the photon detection rate, $\Delta\nu$ is the line width, and C_{CW} is the CW-ODMR contrast. The value $4/(3\sqrt{3})$ is obtained from the value of the steepest slope of the ODMR waveform when the resonance waveform is assumed to be Lorentzian.

2.4.2 Pulsed ODMR Sensitivity

It is necessary to consider that the Pulsed ODMR method has separate initialization, readout, and sensing times. If the initialization and readout times are t_I and t_R and the sensing time is τ_π. The photon detection rate R multiplied by the duty ratio of readout $t_R/(t_I + \tau_\pi + t_R)$. If the overhead time in the measurement is $t_O = t_I + t_R$ and the contrast of Pulsed ODMR is C_{Pulsed}, the sensitivity is [44]:

$$\eta_{CW} = \frac{4}{3\sqrt{3}} \frac{h}{g_e \mu_B} \frac{1}{C_{Pulsed}\sqrt{Rt_R}} \frac{\sqrt{\tau_\pi + t_O}}{\tau_\pi} \tag{2.29}$$

Under optimized conditions the value of C_{Pulsed} is higher than C_{CW}.

2.4.3 Ramsey Sensitivity

The shot noise limit sensitivity of the Ramsey method is [44]

$$\eta_{Ramsey} = \frac{\hbar}{g_e \mu_B} (\frac{1}{\Delta m_s \sqrt{N\tau}})(\frac{1}{e^{-(\tau/T_2^* p)}}) \sqrt{1 + \frac{1}{C^2 \eta_{avg}}} \sqrt{\frac{\tau + t_O}{\tau}} \tag{2.30}$$

where N is the number of non-interacting NV centers contributing to the measurement, Δm_s is the difference of m_s states used for sensing, T_2^* is the ensemble dephasing time, p is the decay shape parameter, and C is the measurement contrast, η_{avg} is the flat number of detected photons per readout, and T_O is the measurement overhead including optical initialization, readout, and microwave pulse.

2.4.4 Noise

Noise that affects NV centers when they operate as magnetic sensors can be divided into environmental noise and system noise. Environmental noise is noise that comes from the external world outside the sensor. System noise is the noise generated in the elements necessary for the NV center to operate as a magnetic sensor. Environmental noise includes temperature noise and magnetic field noise. Temperature noise is noise that is generated when the temperature of the NV center changes due to air conditioning or other factors, causing the resonance frequency to change and giving the appearance of a change in the magnetic field. The resonance frequency change caused by temperature change corresponds to 2.6 μT per 1 ℃ in terms of magnetic field. Magnetic field noise is noise caused by geomagnetism and magnetic fields generated by power sources such as 50 Hz/60 Hz. The magnitude of this noise varies depending on the ambient environment, but can be as high as 50 μT. System noise includes temperature noise, electrical noise, and laser noise. The temperature noise is caused by fluctuations in the resonance frequency of the NV center due to fluctuations in the output of the laser that excites the NV center, which causes the magnetic field to appear to change. The laser output fluctuation is fast, but a low-noise laser is used to excite

Table 2.1: Typical values for environmental and system noise. These values vary depending on the experimental environment and equipment used.

	System noise	Environmental noise
Temperature	$1 \sim 3\,\mathrm{nT}$	$2.6\,\mu\mathrm{K}$ [29]
Magnetic field	–	$\sim 50\,\mu\mathrm{T}$
Electric field	$\sim 1.5\,\mathrm{nT}$	–
Laser	$\sim 3\,\mathrm{nT}$	–

the NV center. Therefore, the magnitude of the noise due to fluctuations in laser output is about $1 \sim 3\,\mathrm{nT}$. Electrical noise is the noise caused by the appearance of changes in the magnetic field due to $1/f$ noise superimposed after the fluorescent signal of the NV center is converted into an electrical signal. The biomagnetic field such as magnetoencephalography has a frequency of less than 1 kHz. Therefore, they are greatly affected by $1/f$ noise. The value is about 1.5 nT. Table 2.1 summarizes these noises. These values are many orders of magnitude larger than the magnitude of the magnetoencephalography, making it impossible to measure magnetoencephalography without noise reduction.

2.4.5 Noise reduction method

In the previous section, we described noise that affects sensitivity when NV centers are used as magnetic sensors. This section describes noise reduction methods for these noises.

System noise reduction method

The temperature noise, one of the system noises, fluctuates quickly in time because of the power fluctuation of the laser that excites the NV centers. The resonance frequencies of the NV centers, depending on the spin state (in this case, two with $m_s = \pm 1$), change in the direction away from each other when the magnetic field increases. On the other hand, when the temperature increases, the frequencies decrease in the same direction as each other. Therefore, the temperature noise can be cancelled by taking the difference of the resonance frequency change of each other [48]. Electrical noise is dominated by 1/f noise; the signal from the NV center can be modulated to a frequency band where $1/f$ noise is negligible by FM modulation of the microwave to operate as a magnetic sensor. This modulated signal can be demodulated by a lock-in amplifier to significantly reduce electrical noise [49]. Laser noise is caused by fluctuations in the fluorescence signal of the NV center due to fluctuations in the output of the laser that excites the NV center; it is not possible to distinguish between changes in the fluorescence signal due to changes in the laser output and changes in the fluorescence signal due to changes in the magnetic field alone. Laser noise can be reduced by monitoring the laser separately and subtracting the amount of laser output variation from the fluorescence signal [20].

Environmental noise reduction method

Temperature noise, one of the environmental noises, fluctuates slowly due to changes in ambient temperature caused by air conditioning and other factors. As described in the temperature noise reduction method of the system noise reduction method, the resonance frequency fluctuation of the NV center due to temperature change can be distinguished from the fluctuation due to the magnetic field. The temperature noise can be reduced by changing the microwave frequency that makes the NV center operate as a sensor by the amount of resonance frequency variation due to temperature. Magnetic field noise is the magnetic field generated by the geomagnetic field or an external 50/60 Hz power supply. Magnetic field noise can be reduced by using a magnetic shield, which is a method of canceling magnetic field noise using a gradiometer [50]. In this case, a three-layer magnetic shield box was used to reduce the magnetic field noise.

2.5 Conclusion

This chapter summarises the principles of NV and the noise superimposed when operate as a magnetic sensor. It is summarised that the shot noise-limited sensitivity of magnetic sensors using NV centres depends on the method used. This allows us to understand the key parameters for each method. Noise superimposed on the sensor is summarised and their suppression methods are explained. This will be useful for analysing noise sources when there is a gap between the actual sensor sensitivity and the shot noise sensitivity.

Chapter 3

Demonstration of magnetocardiographic imaging of living rats

Previous biomagnetic measurements using NV centers have detected the biomagnetic field generated when external stimuli are applied to tissue extracted from a living body. As a feasibility study of biomagnetic measurement, we constructed a measurement system that can detect cardiac magnetism in rats. The results of this rat cardiac magnetic imaging are summarised in the following paper. Millimetre-scale magnetocardiography of living rats using a solid-state quantum sensor. Communications physics volume 5, Article number: 200 (2022).

3.1 Experimental setup

3.1.1 NV diamond sample

The NV diamond crystal used in this study was prepared by the following procedure. A single-crystal of diamond was synthesised by a temperature-gradient method under high-pressure and high-temperature (HPHT) using a modified belt-type high-pressure apparatus [51,52]. The crystal was grown on the (100) plane of a seed crystal in a Co-Ti-Cu solvent at $\sim 5.5\,\mathrm{GPa}$ at 1300-1350 ℃ for 44 h using high-purity graphite with a natural abundance of isotopes (1.1% ^{13}C) as a carbon source. After HPHT diamond synthesis, the grown crystals were cut parallel to the {111} crystal planes, and both the top and bottom surfaces were mirror-polished. The obtained HPHT {111} crystal was a truncated hexagonal pyramid with approximate dimensions of $5.2\,\mathrm{mm}^2 \times 0.35\,\mathrm{mm}$. Then, electron beam irradiation was conducted at room temperature with a 2.0 MeV with a total fluence of 5×10^{17}electrons cm^{-2}, followed by post-annealing at 1000 ℃ for 2 h under a vacuum. The concentrations of the P1 centres and NV− centres in this NV diamond sample were measured by continuous-wave (CW) electron spin resonance to be 15 ppm ($2.6 \times 10^{18}\mathrm{cm}^{-3}$) and 1.8 ppm ($3.2 \times 10^{17}\mathrm{cm}^{-3}$), respectively. The relative uncertainties in these concentrations were both roughly ±30%.

3.1.2 Solid-state quantum sensor structure

Our sensor design is based on that of Schloss et al [53]. However, as shown in Figure. 3.1, 3.2a, we sterically constructed the optical system on two stories to put the system in a custom-made magnetically shielded room with four layers of permalloy (Ishida Ironwork's Co., Ltd.).

A 532-nm laser diode (Coherent Verdi-G5) was installed on the first floor of the setup. The laser polarisation was adjusted to p-polarisation with a half-wave plate (Thorlabs WPH05M-532). The laser beam was directed upward, guided through an M6 screw hole on a breadboard. On the second floor, the beam was then passed through a lens with a focal length f = 400 mm (Thorlabs LA1172-A) and directed diagonally downward by a silver mirror (Thorlabs PF10-03-P01). A laser beam with a 1/e2 Gaussian width of 400 m and a typical incident power P0 = 2.0 W was introduced to the diamond's top major (111) surface at an incidence angle of 70°. The estimated transmittance at the top air-diamond interface was >99%. An achromat 1.25 NA Abbe condenser lens (Olympus U-AC) collected red fluorescence from the NV centres through the top surface. Fluorescence was then passed through a long-pass filter (Thorlabs FELH0600) and directed onto a silicon photodiode (Thorlabs SM1PD1A). The condenser lens, the optical filter, and the photodiode were mounted downward on an XY manual translation stage (Thorlabs XYT1/M). Their heights were adjusted using a long-travel vertical translation stage (Thorlabs VAP10/M). The typical power of the collected fluorescence was PF = 33 mW, corresponding to a photocurrent of 14 mA, given the photodiode's 0.45 A/W responsivity at a 680 nm wavelength. A beam sampler (Thorlabs BSF-10A) was used to pick off 1.5% of the laser light, which was directed onto another silicon photodiode (Thorlabs SM1PD1A). This photocurrent signal became a reference for cancelling the laser fluctuation noise. A ring-shaped rare-earth magnet (Magfine Corporation NR0101) aligned along the [111] orientation applied a uniform static bias field of B0 = 1.4 mT at the diamond to split the mS = ±1

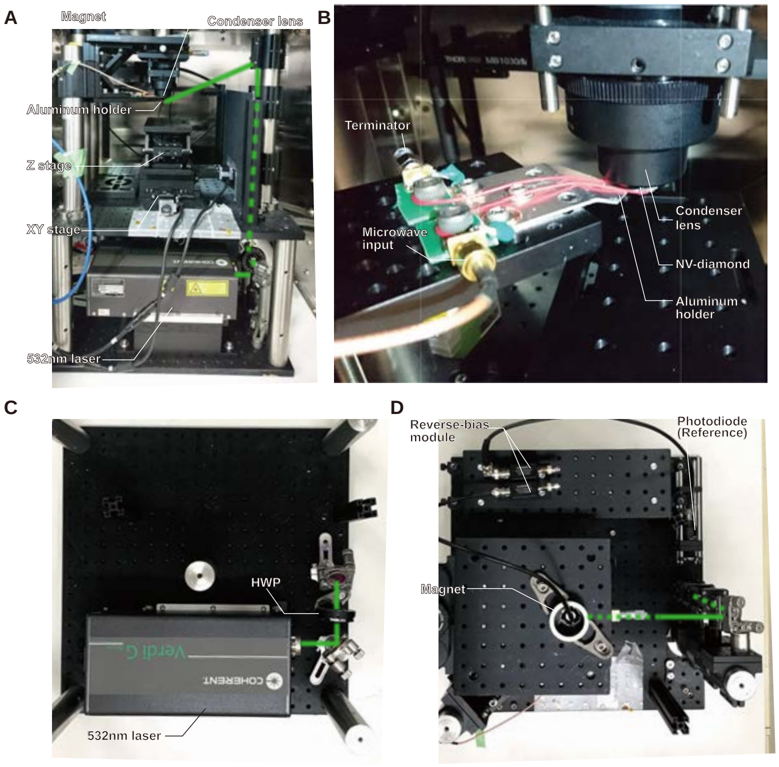

Figure 3.1: Solid-state quantum sensor structure. a, Front view of solid-state quantum sensor built on a two-story breadboard system and installed in a magnetically shielded box. A 38 mm post in the front left supports the nitrogen-vacancy (NV)-diamond-mounted aluminum holder. b, Zoomed view of a millimeter-thick aluminum holder. The two SMA connectors attached to the holder lead to the microwave amplifier and the 50 W terminator. A copper tape attached under the polycrystalline diamond and connected to two thin insulated copper wires serves as a conducting plane, whereas the aluminum holder serves as a ground plane for the microwave delivery. c, Top view of the first floor. The laser light passes through a half-wave plate (HWP), changes direction upwards, and passes through an M6 screw hole on the second-floor breadboard. d, Top view of the second floor. The light goes into the diamond located near the centre of the breadboard. The reference photodiode is located at the top right corner.

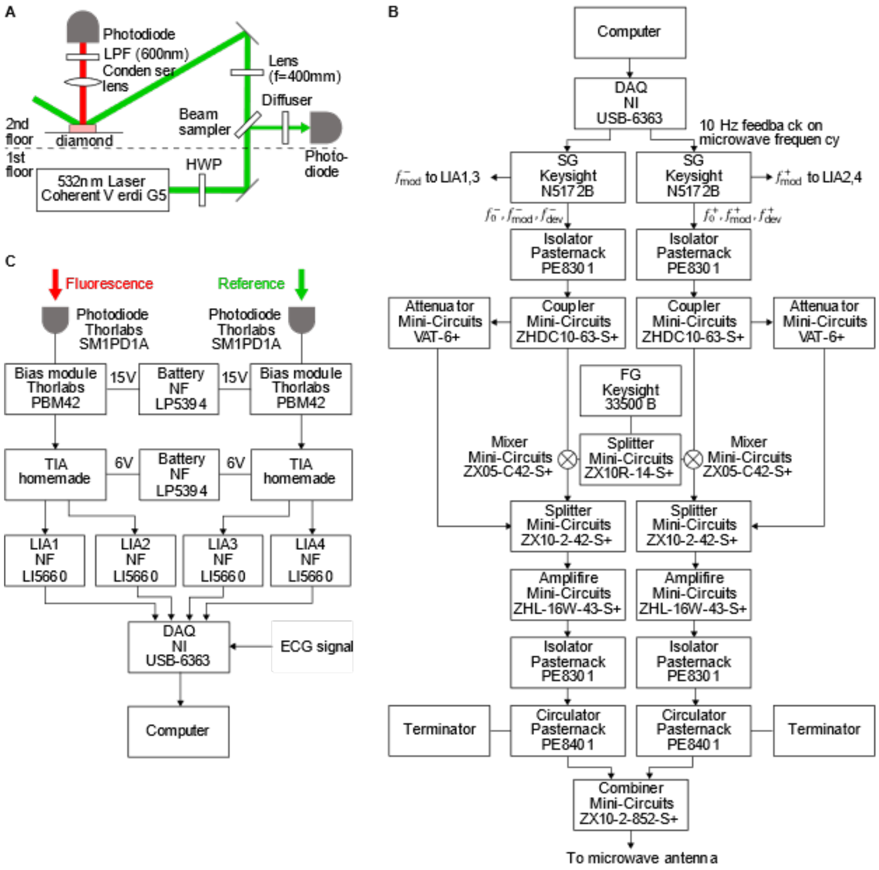

Figure 3.2: Optical, microwave, and detection setup. a, Schematic diagram of the optical setup. A half-wave plate (HWP) adjusts the laser polarization, and a diffuser diffuses the beam for the reference photodiode. A 600 nm long-pass filter (LPF) cuts the short-wavelength light before the fluorescence photodiode. b, Microwave circuit. Two signal generators (SG) generate modulated microwave signals. A function generator (FG) generates a 2.16-MHz frequency signal for three-tone driving. A 10-Hz microwave carrier frequency feedback signal is provided from a computer through a data acquisition module (DAQ). c, Light collection circuit. Trans-impedance amplifiers (TIA) convert the photocurrent to voltage. The amplified signal voltages are demodulated by lock-in amplifiers (LIA). The DAQ converts the demodulated analog signal to a digital signal, which is transmitted to the computer.

ground states. The microwave was irradiated on the diamond via a home-made microwave antenna. Each rat was placed on a 33 cm × 23 cm × 2.1 cm custom-made acrylic board with hot water circulating heater. The acrylic board was placed on a manual translation stage (Thorlabs L490/M) for height adjustment (Zaxis) and an automatic XY translation stage (SIGMA KOKI HPS120-60XY-SET) for horizontal mapping (X-Y plane). In this work, the rat was translated rather than the diamond sensor to avoid sensitivity degradation due to, for example, the change in the incidence angle of the laser.

3.1.3 Microwave and optical readout circuit

The microwave-driving schematic is shown in Figure. 3.2b. Two signal generators (Keysight N5172B) output microwave signals at carrier frequencies $f^{\pm}$ resonated with the $m_S = 0 \leftrightarrow \pm 1$ transitions (Channels 1 and 2). These microwave signals were squarely frequency modulated at modulation frequencies $f_{mod}^{\pm}$, and deviation frequencies $f_{dev}^{\pm}$, respectively. The modulation signals were also introduced to two lock-in amplifiers (NF Corporation LI5660). One of the two signal generators produced a 10 MHz reference signal to synchronise all lock-in amplifiers and the other signal generator. The modulated signal then passed through the isolators (Pasternack PE8301). To drive all the three ^{14}N hyperfine peaks of the NV centre, we generated microwave sidebands at ±2.16 MHz, corresponding to the hyperfine shift of the resonance frequency, in the following manner. In each of the two channels corresponding to $m_S = 0 \leftrightarrow \pm 1$ transitions, the carrier signal was split into two branches using a −10 dB coupler (Mini-Circuits ZHDC-10-63-S+). One branch was up and down frequency-converted by mixing (Mini-Circuits ZX05-C42-S+) with a 2.16 MHz sinusoidal signal, which was produced from a frequency generator (Keysight 33500B) and divided half by a splitter (Mini-Circuits ZX10R-14-S+). The other branch was attenuated (Mini-Circuits VAT-6+) to balance the power between the two branches. The two branches were then combined using a splitter (Mini-Circuits ZX10-2-42-S+) in a reverse manner. The two channels carrying triplefrequency microwave signals in each were separately amplified (Mini-Circuits ZHL-16W-43-S+) before being combined (Mini-Circuits ZX10-2-852-S+) and finally delivered to a microwave antenna. In more detail, an isolator (Pasternack PE8301) and a circulator (Pasternack PE8401), with the third port being 50 Ω terminated, were inserted in each channel to protect the amplifier against microwaves reflected from the antenna. In the DC magnetic field measurement, we parked the microwave carrier frequency where the lock-in ODMR signal's slope was largest to maximise the change in lock-in amplifier signal for a given magnetic field shift. However, in longterm measurements, the resonance frequency gradually shifts due to the temperature drift and residual magnetisation in the surroundings. Consequently, at the parked frequency, the signal slope decreases, and the magnetic field sensitivity deteriorates. To solve this degradation, we implemented carrier frequency feedback by measuring the resonance frequency every 100 ms. The deviation of the optimal frequency, calculated by dividing the error signal by the slope, was fed back from the lock-in amplifier to the signal generator to perform a follow-up correction. The proportional-integral control algorithm performed in a PC determined the correction amount. The optical readout schematic is shown in Figure 3.2 c. The detected photodiode signals were passed through each of two reverse-bias modules (Thorlabs PBM42) with a low-noise DC power supply (NF Corporation LP5394) and amplified through a homemade trans-impedance amplifier with the same power supply before being directed into the lock-in amplifiers. The four demodulated signals, V_F^+,V_F^-, V_L^+,V_L^- were then sampled by a data acquisition module (National Instruments USB-6363) at $fs = 5 \times 10^4$ sample/s. A lock-in time constant of $\tau_{LIA} = 50$ µs was used, providing an equivalent noise bandwidth of $f_{ENBW} = 3.125$kHz

3.1.4 Diamond sample holder

A diamond sample holder schematic is shown in Figure 3.3a, b. The NV diamond was glued with a thermal conductive adhesive (Widework JT-MZ-03M) on a polycrystalline diamond plate (10mm × 10mm × 0.3mm) to spread the heat produced by the laser beam. The polycrystalline diamond was then attached to a custom-made aluminium holder (10mm × 10mm × 1mm), which served as a heat sink and a ground plane for microwave delivery. Attached to the rear surface of the polycrystalline diamond was a copper tape (4mm × 10mm × 0.06mm), which served as a conducting plane for microwave delivery as well as a reflector of the laser and fluorescence light. This copper tape also ensured that the laser intensity transmitted to the rat was a few orders of magnitude below the damage threshold

3.1.5 Laser absorption and fluorescence emission

In this experiment, we chose the laser incident angle to maximise the optical excitation of the NV centres by the laser at a given power for optimum sensitivity. The laser light absorption depends on the amount of laser

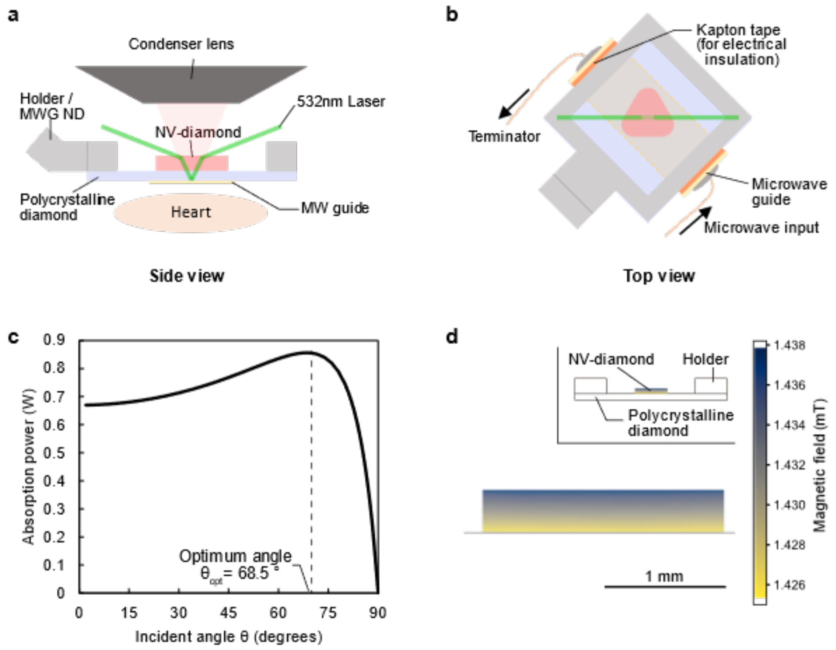

Figure 3.3: Diamond sample holder design. a, Side view of the diamond area (not to scale). The nitrogen-vacancy (NV)-diamond is affixed to the top of a polycrystalline diamond using a thermal paste for stabilization and heat sinking. Copper tape at the bottom of the polycrystalline diamond provides a modulated microwave (MW) drive to the NV centres and serves as a laser light reflector. b, Top view of the diamond sample holder. polished. The NV-diamond has a truncated hexagonal pyramid shape. c, Dependence of absorption power on the incidence angle. The absorption is maximal when the incidence angle is $\theta_{opt} = 68.5°$. d, Magnetic field profile around the diamond sample, simulated using the COMSOL software package. The field variation from the top to the bottom of the diamond is 12 µT, corresponding to an optically detected magnetic resonance (ODMR) peak broadening of 340 kHz.

power entering the NV diamond as well as the distance the laser travels in the diamond at a given incident angle. According to Fresnel's and Snell's law, the transmittance at the air-diamond interface is given by $T_p(\theta) = 1 - [\tan(\theta - \theta_d)/\tan(\theta + \theta_d)]^2$ and $n_d \sin\theta_d = n_0 \sin\theta$, where and d are the angles of incidence and refraction, respectively, $n_0 = 1$ and $n_d = 2.42$ are the refractive indices of air and diamond. The transmittance becomes unity when the incident angle is equal to Brewster's angle $\theta = \arctan(n_d/n_0) = 67.5^\circ$. The one-way path length of the laser L_e depends on the laser incident angle through $L_e(\theta) = L_d/\cos\theta_d$, where $L_d = 0.35$ mm is the diamond thickness. With the deduced transmittance $T_p(\theta)$ and path length $L_e(\theta)$, we calculated the amount of laser absorption under the assumption that the dominant absorbers were NV^- and NV^0. Let $\sigma^{NV^-} = 3.1 \times 10^{17}\mathrm{cm}^2$ and $\sigma^{NV^0} = 1.8 \times 10^{17}\mathrm{cm}^2$ be the absorption cross-section [54, 55] and $[\mathrm{NV}^-] = 3.2 \times 10^{17}\mathrm{cm}^3$ (measured) and $[\mathrm{NV}^0] = 1.0 \times 10^{17}\mathrm{cm}^3$ (estimated) be the absorber density for NV^- and NV^0, respectively. From the top to the bottom surface, the laser power absorbed by NV^- and NV^0 was $P_{L_1}^{\mathrm{NV}} = P_0 T_p(\theta)[1 - \exp(-\alpha^{\mathrm{NV}} L_e)]$, where $P_0 = 2.0$ W is the laser incident power, and $\alpha^{\mathrm{NV}} = \sigma^{\mathrm{NV}^-}[\mathrm{NV}^-] + \sigma^{\mathrm{NV}^0}[\mathrm{NV}^0] = 12\mathrm{cm}^1$ is the total absorption coefficient. On the way back from the bottom to the top surface after being reflected by the copper with reflectivity $R_{Cu} \sim 0.67$ at 532 nm, the light absorbed becomes $P_{L_2}^{\mathrm{NV}}(\theta) = P_0 T_p(\theta) \exp(-\alpha^{NV} L_e) R_{Cu}[1 - \exp(-\alpha^{NV} L_e)]$. To obtain the absorption by NV^-, we must multiply by a fraction $\xi^{\mathrm{NV}^-} = \sigma^{\mathrm{NV}^-}[\mathrm{NV}^{-1}]/\alpha^{\mathrm{NV}} \sim 85\%$. Thus, the total laser power absorbed by the NV^- centres is given by $P_L^{\mathrm{NV}^-}(\theta) = \xi^{\mathrm{NV}^-}(P_{L_1}^{\mathrm{NV}}(\theta) + P_{L_2}^{\mathrm{NV}}(\theta))$. As shown in Figure. 3.3c, the absorption light becomes maximum at an incident angle of $\theta_{opt} = 68.5^\circ$ to be $P_L^{\mathrm{NV}^-}(\theta_{opt}) = 0.85$ W. The photon absorption rate per NV^- centre is then $R_L = P_L(\theta_{opt})/N_F(\theta_{opt})/h\nu_L = 38\,\mathrm{kHz}$ per NV, where $N_F(\theta_{opt}) = 6.0 \times 10^{13}$ is the total number of NV^- centres emitting photons, and $\nu_L = 564$ THz is the absorbed green laser frequency. The photon emission rate per NV^- centre is $R_F = Q_Y R_L = 32$ kHz per NV, where $Q_Y = 0.83$ is the quantum yield from an absorbed green to an emitted red photon determined from the NV^-photodynamics [56]. Thus, the total red fluorescence power from the diamond decreases to $P_F = R_F N_F h\nu_F = 0.55$ W, where $\nu_F = 441$ THz is the typical emitted red fluorescence frequency. Because the collection efficiency estimated from the condenser lens's optical properties and detection geometry was $\beta \approx 6\%$, the red fluorescence collected by the detector was estimated to be 33 mW, which is in agreement with experimental observations.

3.1.6 Bias field uniformity and thermal stability

The static bias field may introduce an ODMR linewidth broadening and resonance peak shift due to the field inhomogeneity and thermally induced field fluctuations, respectively. However, as discussed below, these effects did not affect our magnetocardiography measurements. First, we performed a magnetic field simulation using the COMSOL software package (Figure. 3.3d) to evaluate the static field inhomogeneity across the diamond. The simulated field variation across the diamond induced an ODMR linewidth broadening of 0.34 MHz. This broadening was six times smaller than the ODMR linewidth, and thus, we ignored this effect in this experiment. Second, we estimated the temperature effect on the bias magnetic field. Because of the small thermal diffusivity of the magnet, even if the lab temperature suddenly changed by 0.1 K, the estimated speed of magnet temperature change was less than $\sim 0.1\mathrm{mKs}^{-1}$. Such a magnet temperature change would introduce a magnetic field shift of $< 200\mathrm{pTs}^{-1}$ at the diamond, calculated from the bias field B_0 and the reversible temperature coefficient of the magnet -0.12% per Kelvin. This amount of resonance peak shift could be suppressed by the microwave feedback system.

3.1.7 Rat surgical protocol

The animal experiment was approved by the University of Tokyo Ethical Review Board (reference number KA18-15), and every procedure followed the institutional guidelines, ensuring the humane treatment of animals. The animals studied were five male SLC/Wistar rats (Japan SLC, Inc., Tokyo, Japan). Only male rats were studied because no significant sex bias in normal R-waves had been known. Each rat was held on a hot-water bed (water temperature: 45.0°C), where hot water was circulated through a silicon tube via a water circulation system (Thermo Haake DC10/K10, Thermo Fisher Scientific GmbH, Germany) for maintaining its body temperature. The anaesthesia, tracheotomy, artificial ventilation, and thoracotomy processes were as follows (Figure.3.4a–c). First, rats were anaesthetised using 2-3% isoflurane in 300 mL per min air via an automatic delivery system (Isoflurane Vaporiser; SN-487; Shinano Manufacturing, Tokyo, Japan). Next, under moderate anaesthesia, the body hair of each rat was shaved, and a tracheotomy was performed for artificial ventilation. For the artificial respirator (Small Animal Ventilator, SN-480-7, Natsume Seisakusho Co., Ltd., Japan), 2-3% isoflurane in 2.5 mL air per respiration at 80 times per min was delivered to each rat during the imaging of cardiac magnetic fields and

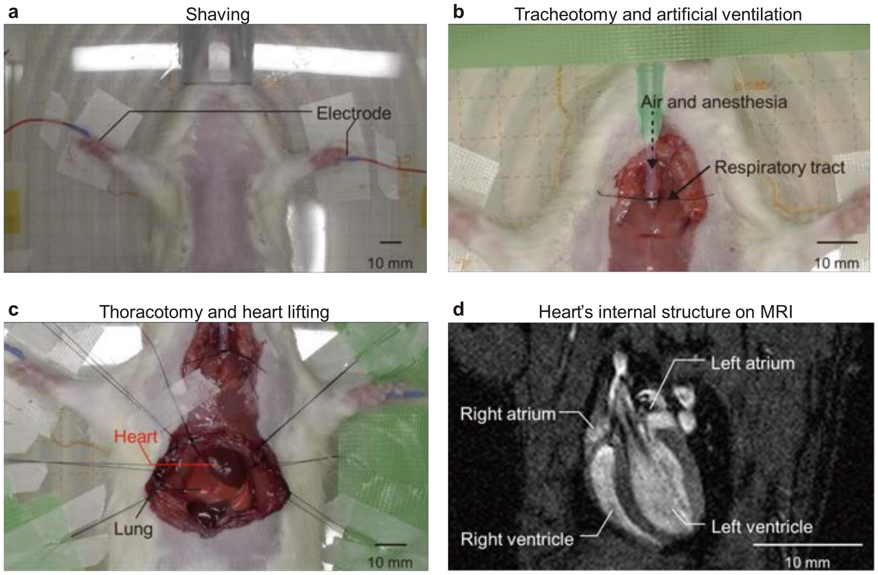

Figure 3.4: Rat preparation process. a, Shaving. The rats are shaved under moderate depth anaesthesia for subsequent surgical procedures. b, Tracheotomy and artificial ventilation. The skin and muscle are incised around the trachea, and tracheotomy is conducted. Artificial ventilation supports respiration. c, Thoracotomy and heart lifting. The breastbone is cut along the centre line, and the pectoral muscle is pulled toward both sides. The heart is lifted by surgical sutures. d, Internal structure of the rat heart revealed by magnetic resonance imaging.

the surgical process. Subsequently, a thoracotomy was performed to expose the heart. Nylon threads were used to lift the heart for further exposure outside the body surface. This vivisection and heart-lifting were necessary to place the sensor a millimetre away from the heart surface. After completion of all experimental procedures, the animals were sacrificed under deep anaesthesia due to the ethical reason that rats should not suffer from the pain any longer.

3.1.8 Magnetic resonance imaging

Before magnetic field measurements on rat samples, MRI was conducted with a 7-Tesla MRI system (BioSpec 70/20USR, BRUKER, Germany) to confirm each heart's internal structure (Figure. 3.4 d). Each rat was mounted in a cylindrical sample holder. Images of the rat hearts were obtained without a contrast agent and using a FLASH-cine sequence at 1-mm thickness and with a 60 mm × 60 mm field of view. The details of the MRI sequences are as follows: repetition time $T_R = 2.5\,\mathrm{ms}$, echo time $T_E = 8.0$ ms, 192 × 192 pixels, excitation pulse angle = 15°, the exposure time for movie recording = 160 ms, and the number of movie cycles = 20.

3.1.9 Electrocardiography

Each sample's electrode voltage was recorded with an ECG recording instrument (Neuropack X1, Nihon Kohden Corporation, Japan) through a recording electrode (Natus Ultra Subdermal Needle Electrode 0.38 mm, Natus Neurology Inc., USA) before being sent to the data acquisition module simultaneously with the MCG signal. The ECG signal was used as a reference for the MCG measurement and to monitor heart activities [57]. The typical heart rate was 4.5-8.0 Hz, which did not change more than 30% before and after the surgical operations and during the measurement (Figure.3.5).

3.1.10 Three-tone ODMR spectroscopy

The superposition of three Lorentzian functions efficiently approximates the line shape of the CW ODMR spectrum in the presence of optical and microwave power broadening [47]:

$$P_F^{single}(f) = P_{F0}\left[1 - C\sum_{k=-1,0,1}\left(-\frac{(\frac{\Gamma}{2})^2}{(\frac{\Gamma}{2})^2 + (f-(f_0+kf_n))^2}\right)\right] \tag{3.1}$$

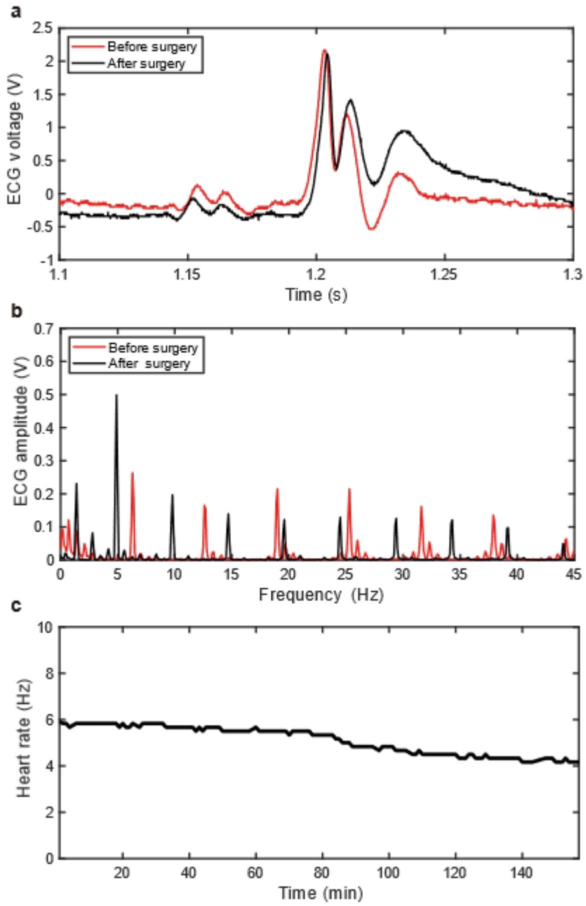

Figure 3.5: Electrocardiogram (ECG) measurement. a, Example of ECG signal before (red) and after (black) surgical operations. The electrical voltage of ECG is detected with three electrodes attached to the left and right front-foot and the left rear-foot. b, Amplitude of the Fourier transform of the measured ECG signal before (red) and after (black) surgical operations. In this example case, the heart rate dropped from 6 Hz to 5 Hz. For most cases, the change in heart rate was no more than 30%. c, Example of change in the heart rate during the measurement. The heart rate gradually decreased from 6 to 4 Hz. For most cases, the heart rate changed by no more than 30% over three hours.

where f is the single-tone microwave carrier frequency, P_{F0} is the baseline red fluorescence observed without applying microwaves, C is the fluorescence contrast of the resonance peaks, Γ is the linewidth (full width at half maximum, FWHM), f_0 is the resonance frequency of the central peak, and $f_n = 2.16$ MHz is the ^{14}N hyperfine coupling strength. In this experiment, we applied triple-tone microwave signals with carrier frequencies of $f - f_n$, f, and $f + f_n$ to increase signal contrast. The CW ODMR spectrum then becomes

$$P_F^{triple}(f) = P_{F0}\left[1 - C\sum_{j=-1,0,1}\sum_{k=-1,0,1}\left(-\frac{(\frac{\Gamma}{2})^2}{(\frac{\Gamma}{2})^2 + ((f + jf_n - (f_0 + kf_n)))^2}\right)\right] \tag{3.2}$$

In numerous high-sensitivity magnetic sensing measurements, technical noise such as $1/f$ noise presents a large electronic noise floor, making it difficult to extract a small magnetic field signal from the sample of interest. To mitigate such $1/f$ noise at low frequencies and obtain a larger SNR, the sensing bandwidth may shift away from DC to higher frequency via up-modulation. A standard method in NV diamond magnetometry experiments, e.g., the one described in detail in the study of ref. [20], applies square-wave frequency modulation to the microwaves. The output spectrum after demodulation using the lock-in amplifiers becomes a differential function:

$$\begin{aligned} V(f) &\propto \frac{P_F^{triple}(f - f_{dev}) - P_F^{triple}(f + f_{dev})}{2} \\ &= \frac{V_0 C}{2}\sum_{j=-1,0,1}\sum_{k=-1,0,1}\left[-\frac{(\frac{\Gamma}{2})^2}{(\frac{\Gamma}{2})^2 - ((f + jf_n - f_{dev}) + (f_0 + kf_n)^2)}\right. \\ &\quad \left. + \frac{(\frac{\Gamma}{2})^2}{(\frac{\Gamma}{2})^2 - ((f + jf_n + f_{dev}) - (f_0 + kf_n)^2)}\right] \end{aligned} \tag{3.3}$$

where V_0 is the lock-in voltage dependent on P_{F0} and the output settings of the lock-in amplifier, and f_{dev} is the deviation frequency. Taking the derivative of the lock-in ODMR spectrum, one finds that, in theory, $f_{dev} = \Gamma/2\sqrt{3}$ yields the optimum slope.

3.1.11 Microwave parameter determination

We chose the microwave parameters in the following manner. First, the NV resonance frequencies $f_0^{\pm}$ corresponding to the $m_s = 0 \leftrightarrow \pm 1$ transitions were determined by the CW ODMR spectrum under the triple-tone microwave excitation. Second, the microwave excitation amplitude was varied to find where the contrast over the FWHM linewidth, $C/\Delta f$, in the CW ODMR spectrum reached nearly the maximum value around 10 dBm (Figure. 3.6a), above which we observed an increase in the noise floor due to the microwave higher harmonics. As the microwave amplitude increased, the linewidth increased faster than the signal contrast; thus, there was an optimum point that yields the maximum contrast/linewidth. The optimised CW ODMR spectrum is shown in Figure. 3.6b. Third, the deviation frequency $f^{\pm}_{dev}$ was varied to find the maximum slope (Figure. 3.6c). Finally, the microwave modulation frequency $f^{\pm}_{mod}$ was varied to determine the minimum sensitivity (Figure. 3.6d-f). As the modulation frequency increases, the $1/f$ featured noise floor improves, whereas the slope decreases due to the reduction in NV spinstate contrast [49, 58]. The lock-in ODMR spectrum of the $m_s = 0 \leftrightarrow \pm 1$ transitions recorded with the optimised microwave parameters is shown in Figure. 3.6g.

3.1.12 Lock-in DC magnetometry scheme

In lock-in DC magnetometry [20, 53, 59], the microwave carrier frequency is set to a value at which the lock-in ODMR slope becomes maximal while the NV states are continuously excited via optical and microwave illumination. A time-varying external DC magnetic field $B(t)$ is then sensed as the shift in the resonance frequency $f_0(t) = f_0 + \delta f(t)$, where $\delta B(t) = g_e \mu_B h^{-1} \delta B(t)$. When the resonance frequency changes, the fluorescence intensity and the lock-in signal change accordingly. The field is then extracted by dividing the change in the lock-in voltage δV by the lock-in ODMR slope dV/df as $\delta B(t) = g_e^{-1} \mu_B^{-1} h \delta V(t)(dV/df)^{-1}$. We applied this frequency up-modulation to both $m_s = 0 \leftrightarrow \pm 1$ transitions simultaneously but with different modulation frequencies $f^{\pm}_{mod}$ and deviation frequencies $f^{\pm}_{dev}$; thus, information about each transition was encoded in different modulation frequency bands. The signal associated with each transition was obtained by lock-in demodulation at the corresponding modulation frequencies. This method allowed us to cancel out the temperature fluctuations that appeared as common-mode noise in both transitions. Calibration of the sensor was performed by applying a known test sinusoidal field and measuring the field with the sensor. The measured field was consistent with the applied field to better than 2.5%. This systematic error was a few times smaller than the statistical errors in the MCG measurements.

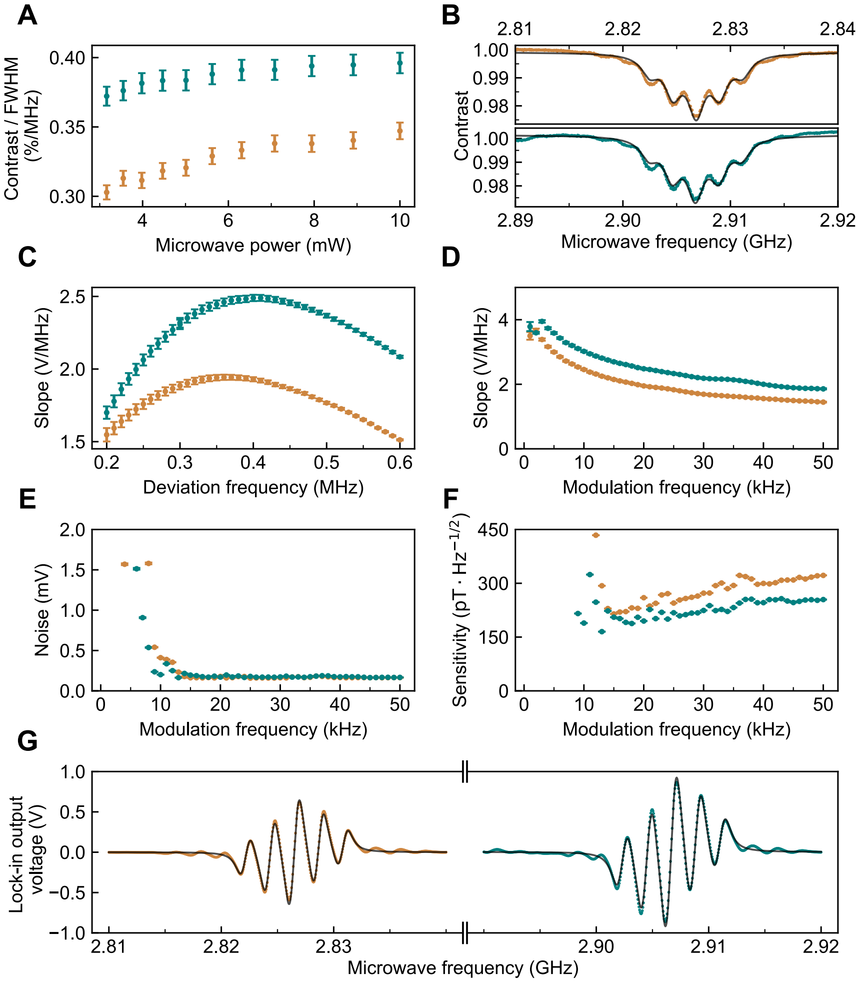

Figure 3.6: Microwave parameter determination process. a, Change in contrast divided by full width half maximum (FWHM) of the continuous-wave optically detected magnetic resonance (CW ODMR) resonance spectrum as a function of microwave power at the signal generator output. The contrast is the focused fluorescence normalized by the fluorescence at the time of non-resonance. b, CW ODMR spectrum measured with the nearly optimum microwave power. The black curves are fit to the model. c, Change in slope as a function of deviation frequency $f^{\pm}_{dev}$. d-f, Changes in slope (d), noise (e), and magnetic field sensitivity (f) as a function of microwave modulation frequency $f^{\pm}_{mod}$. The deviation frequency is set to the optimum value obtained in (c). g, Lock-in ODMR spectrum with the microwave parameters determined in (a)-(f). The black curves are fit to the model. For (a)-(g), the green and amber data indicate the $m_s = 0 \leftrightarrow +1$ and $m_s = 0 \leftrightarrow -1$ transition, respectively. Error bars are calculate using the uncertainties (one standard deviation) of the fitted parameters.

3.1.13 Signal processing

In this experiment, we obtained four lock-in amplifier outputs: $V_F^+, V_F^-, V_L^+, V_L^-$, where $F_F^\pm$ is the fluorescence signal demodulated at $f_{mod}^\pm$ and $V_L^\pm$ is the laser reference demodulated at $f_{mod}^\pm$. The data analysis process comprised five steps (Figure.3.7). First, laser noise cancellation was performed. Laser fluctuations appeared in all four outputs as common-mode noise. This noise can be suppressed by subtraction: $V_s^+ = V_F^+ - \xi^+ V_L^+$ and $V_s^- = V_F^- - \xi^- V_L^-$. The scaling factors $\xi^\pm$ were fixed to the ratio between the fluorescence photodiode's average signal level and the laser reference photodiode's average signal level, measured at the beginning of the measurement run. Second, the temperature drift that interferes with cardiac magnetic field detection was cancelled as commonmode noise by subtracting the $m_s = 0 \leftrightarrow +1$ signal from the $m_s = 0 \leftrightarrow 1$ signal: $V_s = (V_s^- - \zeta V_s^+)/2$. The scaling factor ζ was fixed to the ratio between the $m_s = 0 \leftrightarrow 1$ signal slopes, determined from the lock-in ODMR spectrum. Third, notch filtering was performed. The electronic background noise within the measurement bandwidth was removed with a notch filter at multiples of 11 and 50 Hz. The filtered signal was defined as $V_s^{'}$. Fourth, the obtained MCG data were timecompensated and averaged. Because the raw MCG data had poor SNR, the magnetic pulse timing was determined from the R-wave peak location in the ECG temporal data. The MCG temporal traces were cut from −300 to +300 ms around the peaks, and these 600 ms temporal traces were overlapped and averaged. Fifth, band-pass filtering was performed. Because most of the magneto-cardiac signals were between 3 and 200 Hz, a 3–200 Hz band-pass filter was applied. For magnetic imaging in Figs. 3 and 4, the acquisition duration was 40 s per pixel. Such a 40-s data contained approximately 220 peaks with 6 Hz repetition. By averaging these peaks, the SNR reached 8.

3.1.14 OPM magnetocardiography

To verify the experimental data measured by the solid-state quantum sensor, we performed two-dimensional MCG imaging with an OPM (QZFM-Gen2, QuSpin Inc.) inside the magnetically shielded room. The OPM sensor's vapour cell was located 8.5 mm above each rat's heart surface. A two-dimensional image of the MCG signals was recorded on the X-Y plane ([-15, +15] mm with a 3 mm step size, $11 \times 11 = 121$ measurement points, and a 1 kHz sampling rate). The data acquisition time per pixel was 10 s.

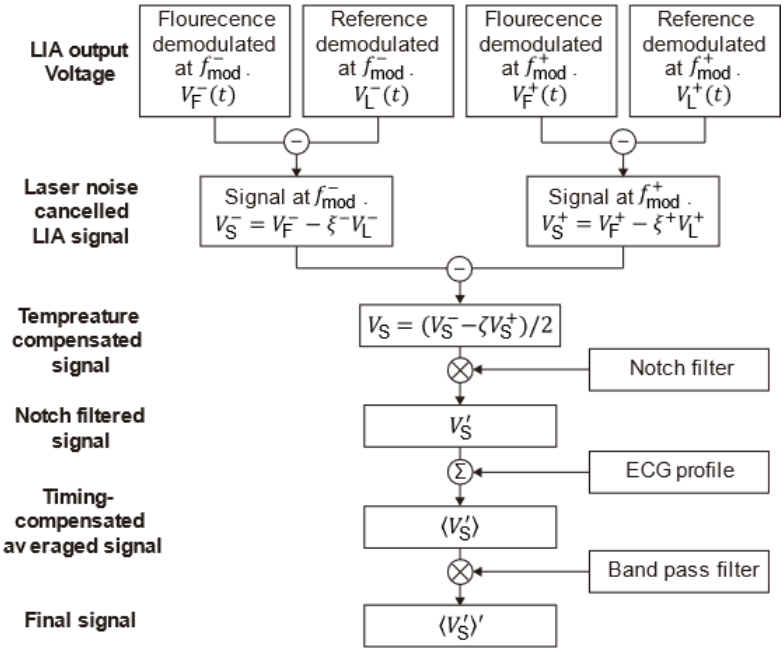

Figure 3.7: Magnetocardiography signal processing protocol. Lock-in amplifiers demodulate fluorescence and laser reference photodiode signals: $V_F^{\pm}, V_L^{\pm}$. Laser fluctuations are cancelled by subtracting the laser reference signal from the fluorescence signal: $V_s^{\pm} = V_F^{\pm} - \xi^{\pm} V_L^{\pm}$. Temperature fluctuations are compensated by subtracting $m_s = 0 \leftrightarrow +1$ transition signal from $m_s = 0 \leftrightarrow 1$ signal: $V_s = V_s^{-} - \zeta V_s^{+}$. Electronic noise at multiples of 11, 50 Hz is removed by applying notch filters. The obtained signal is averaged after adjusting the timing of the cardiac signal using the timing of pulses extracted from the Electrocardiogram (ECG) profile. Furthermore, the signal is smoothed, and slow variations are removed by applying a bandpass filter.

3.2 Analysis method

3.2.1 Current dipole model

The multiple-current-dipole model used in this work consisted of $N_{\mathrm{Q}} = 7$ central current dipoles with the same magnitude and orientation and a pair of return current dipoles with opposite orientations. The central dipoles were distributed evenly across the vertical cross-section of the heart: $\boldsymbol{Q}_C = \sum_{i=1}^{N_{\mathrm{Q}}} \boldsymbol{Q}(\boldsymbol{r_0} + \boldsymbol{z_i})/N_{\mathrm{Q}}$, where $\boldsymbol{Q}$ is the total current dipole moment, $\boldsymbol{r_0}$ is the position vector of the geometric centre of the dipoles, and $\boldsymbol{z_i} = (0, 0, z_i)$ is the vector of the location of each dipole from the centre. The number of central current dipoles were chosen by testing the goodness of numerical fitting with different numbers. The measured magnetic images were not reconstructed well for $N_{\mathrm{Q}} < 7$, while the result did not change much for $N_{\mathrm{Q}} \geq 7$. The return current dipoles were placed $\pm\boldsymbol{\rho_R} = \pm(x_R, y_R, 0)$ from the centre: $\boldsymbol{Q_{\mathrm{R}}} = -k_{\mathrm{R}}[\boldsymbol{Q}(\boldsymbol{r_0} + \boldsymbol{\rho_{\mathrm{R}}}) + \boldsymbol{Q}(\boldsymbol{r_0} + \boldsymbol{\rho_{\mathrm{R}}})]$, where k_R is the ratio of the return current amplitude and the vectors Q and ρ_{R} are set orthogonal to each other. The fitted curve for Fig. 2e was calculated by nonlinear least squares regression with a fitting parameter of $Q = |\boldsymbol{Q}|$, and a predictor variable of the standoff distance d. The dipoles in Figure. 3.12 were calculated by matching simulated magnetic field images with those measured using an L^2-norm minimisation routine. The fitting parameters were the magnetic moment vector $\boldsymbol{Q} = (Q_x, Q_y, 0)$, the magnetic moment centre location $\boldsymbol{r_0} = (x_0, y_0, d_{\mathrm{Q}})$, and the return current dipole location $\boldsymbol{\rho_{\mathrm{R}}}$. Here d_{Q} is the standoff distance between the centre of the central dipoles and the sensor. MRI measurements of the relative sizes and positions of each rat's heart were used to provide an initial guess and impose constraints on these fitting parameters. The uncertainty of the fitted parameters $\delta Q_x, \delta Q_y, \delta x_0, \delta y_0, \delta d_{\mathrm{Q}}$ was estimated from the 68% confidence interval of the fitting. The obtained standoff distance $d_{\mathrm{Q}} \pm \delta d_{\mathrm{Q}}$ was then used in the current density estimation presented in Figure. 3.13.

3.2.2 Electric current density model

The process of electric current density estimation from the obtained magnetic field images in Figure. 3.13 employed bfieldtools [60, 61], an open-source Python software suite. In this software, the surface-current density $\boldsymbol{j}(\boldsymbol{r})$ originates from a piecewise linear stream function $\psi(\boldsymbol{r})$. This stream function is determined such that the L^2-norm of the difference between the simulated field B_{sim}, which is derived from the stream function using the

Biot-Savart's law, and the measured field B_{meas} under a penalty term with a strength of λ becomes minimal: $\psi \in \text{argmin}||B_{\text{meas}} - B_{\text{sim}}||^2 + \lambda||\psi||^2$. Vectors along the contour lines of the stream function represent the surface-current density $\boldsymbol{j}(\boldsymbol{r}) = \nabla_{\|}\psi(\boldsymbol{r}) \times \boldsymbol{n}(\boldsymbol{r})$; where $\boldsymbol{n}$ is the unit vector perpendicular to the surface and $\nabla_{\|} = \nabla - \boldsymbol{n}(\boldsymbol{n} \cdot \nabla)$ is an operator that projects the gradient vector of a scalar function onto the tangent plane of the surface.

3.2.3 Spatial resolution

In this work, we evaluated the resolution, localisation precision, and accuracy of the current dipole moment and magnetic field. For the current dipole moment $\boldsymbol{Q}$, the resolution Δr_{Q} (5.1 mm for the NV and 15 mm for the OPM) was defined in the dipole space as the minimum separation between two dipoles of equal magnitude that are distinguishable through magnetic imaging measurements. Here the two dipoles are claimed to be indistinguishable when the joint magnetic field at the midpoint between these dipoles has zero derivatives, analogous to the Sparrow criterion in optics. The localisation precision δr_{Q} (1.2 mm for the NV and 2.9 mm for the OPM) was defined as the uncertainty (one standard deviation) of the fitted current dipole moment position. The accuracy was estimated from the systematic error in placing the sensor with respect to the heart centre (approximately 0.5 mm for NV and 2 mm for OPM). OPM had greater inaccuracy because it was more technically challenging to align the sensor at a larger standoff distance. For the magnetic field image $B_z(x, y)$, the resolution Δr_{B} (1.5 mm for the NV and 3.0 mm for the OPM) was limited by the imaging pixel size. The localisation precision δr_{B} (0.4 mm for the NV and 0.4 mm for the OPM) was determined from the uncertainty (one standard deviation) of the fitted magnetic pole position. The accuracy was the same as that of the dipole.

3.2.4 Magnetometer performance

Magnetic field sensitivity limits

For nitrogen-vacancy (NV)-based magnetic field sensing, the noise intrinsic to spin projection yields the fundamental sensitivity limit, which is given by [19]

$$\eta_\sigma = \frac{\hbar}{g_e \mu_B} \frac{1}{\sqrt{N T_2^*}} \tag{3.4}$$

where $\hbar = h/2\pi$ is the reduced Planck constant, $N = N_F/4 = 1.5 \times 10^{13}$ is the number of sensing NV centres and $T_2^* \sim 400$ ns is the NV spin coherence time. These values yielded an estimate of the spin projection-noise-limited sensitivity of $\eta_\sigma \sim 2\mathrm{fT} \cdot \mathrm{Hz}^{-1/2}$.

The photon shot-noise-limited sensitivity for continuous-wave optically detected magnetic resonance (CW ODMR) magnetometry is [47]

$$\eta_\gamma = \sqrt{2}\alpha_L \frac{h}{g_e \mu_B} \frac{\Delta f}{C\sqrt{\beta N_F R_F}} \tag{3.5}$$

where the factor $\sqrt{2}$ is an additional shot-noise from the reference photocurrent, $\alpha_L = 4/3\sqrt{3}$derives from a Lorentzian function's steepest slope, $\Delta f = 2.1$ MHz is the full width half maximum (FWHM) linewidth, including microwave and optical power broadening, $C = 1.2\%$ is the signal contrast, and $\beta \approx 6\%$ is the photon collection efficiency. From these values, the photon shot-noise-limited sensitivity became$\eta_\gamma = 19\mathrm{pT} \cdot \mathrm{Hz}^{-1/2}$. The total photon detection rate at the photodiode was estimated as $R_{\mathrm{det}} = \beta N_F R_F = 1.1 \times 10^{17}$ Hz. This value was consistent with what was derived from the measured photoelectron current $I_\gamma = 14$ mA: With $\rho = 0.45\mathrm{A} \cdot \mathrm{W}^{-1}$ the photodiode responsivity at fluorescence wavelength ~ 680 nm, $R_{\mathrm{det}} = I_\gamma(\rho h \nu_F)^{-1} \sim 1.1 \times 10^{17}$Hz.

Magnetic field sensitivity analysis

We measured the sensor's sensitivity in the absence of test field by

$$\eta_m = \frac{h}{g_e \mu_B} \frac{\sigma_V}{\frac{dV}{df}} \tag{3.6}$$

where σ_V, measured in $\mu V \cdot Hz^{-1/2}$, is the noise spectral density obtained from the level of the lock-in amplifier output power spectral density in the flat region, and dV/df is the measured lock-in ODMR slope. The noise was recorded for $T_{trial} = 10$ s under (i) magnetically sensitive configuration, (ii) magnetically insensitive configuration, and (iii) electronic noise configuration, while the slope was determined by fitting the lock-in ODMR spectrum near the zero-crossing frequency for all the above cases. Figure. 3.6a shows a single trace of raw time domain data obtained under a magnetically sensitive configuration, where the microwave carrier frequency was set at resonance. The Fouriertransformed amplitude spectra obtained for such 180 traces of measurements were averaged to improve visibility, revealing the noise floor level in the flat region (1 - 200 Hz) to be $8.4\mu\mathrm{V} \cdot \mathrm{Hz}^{-1/2}$, equivalent to a measured sensitivity of $140\mathrm{pT} \cdot \mathrm{Hz}^{-1/2}$ (Figure. 3.6b). Under the magnetically insensitive configuration, the microwave carrier frequency was set far from the resonance; thus, it was sensitive only to the noise sources introducing fluorescence fluctuations. The magnetically insensitive noise floor was $6.0\mu\mathrm{V} \cdot \mathrm{Hz}^{-1/2}$, corresponding to $100\mathrm{pT} \cdot \mathrm{Hz}^{-1/2}$. In the electronic noise configuration, realized in the absence of the green laser and microwaves, the measured noise floor was $1.8\mu\mathrm{V} \cdot \mathrm{Hz}^{-1/2}(30\mathrm{pT} \cdot \mathrm{Hz}^{-1/2})$. The ×7.4 discrepancy between the shot-noise-limited sensitivity and the measured sensitivity under magnetically sensitive configuration was explained qualitatively by the reduced available slope and enhanced noise. The available slope became smaller than its maximum value by a factor of ~ 1.8 mainly due to the NV ground states' finite cycling time limited by the microwave Rabi frequency and the signal loss into higher harmonics during demodulation. The noise floor was higher than the shot-noise by a factor of ~ 4.1 due to several factors, which likely included electronic noise, residual laser noise, and microwave noise.

Sensor stability analysis

To assess the stability of the solid-state quantum sensor, we calculated the Allan deviation $\sigma_A(\tau)$ as a figure-of-merit. If white noise is dominant, the Allan deviation decreases as $\tau^{-1/2}$, where τ is the averaging time. However, magnetic drift can cause deviation from this scaling, which hinders measurement stability. We repeated N measurements periodically with a time interval Δt, that is, at a constant sampling rate. The total measurement time was T = NΔt. With the obtained data set $y(t) \in \{y(\Delta t), y(2\Delta t), \ldots, y(N\Delta t)\}$, the Allan deviation at time τ is defined by

$$\sigma_A^2(\tau) \equiv \frac{1}{2}\langle(\overline{y}_{k+1}(\tau) - \overline{y}_k(\tau))^2\rangle = \frac{1}{2(K-1)} \sum_{k=1}^{K-1} (\overline{y}_{k+1}(\tau) - \overline{y}_k(\tau))^2 \quad (3.7)$$

where $\overline{y}$ denotes averaging over a time duration of τ. If the Allan deviation is evaluated at $\tau = m\Delta t$, where m takes a power of two, then $K = T/\tau = N/m$, where K is the number of binned groups of duration τ non-overlapped within the total measurement time . The Allan variance $\sigma_A^2(\tau = m\Delta t)$ was, thus, calculated by dividing N pieces of data into K groups of m pieces. In each group $k \in 1, 2, \ldots, K$, there were m data, $y_k \in \{y([(k-1)m + 1]\Delta t), y([(k-1)m+2]\Delta t), \ldots, y([(k-1)m+m]\Delta t)\}$, and as a representative value of each group, their average value was given by $\overline{y}_k = m^{-1}[y([(k-1)m+1]\Delta t) + y([(k-1)m+2]\Delta t) \ldots + y([(k-1)m+m]\Delta t)]$. The Allan variance is the variance of the set of differences between the representative values $\overline{y}_k$.

In the presence of temperature drifts and residual magnetization in the surroundings, the locked frequency can gradually shift, and the Allan deviation deviates from the white noise scaling. Because we applied the carrier frequency feedback by measuring the resonance frequency, random walk type noise was mitigated. An example feedback voltage is shown in Figure. 3.6c. Consequently, the Allan deviation overall scaled as $\sigma_A(\tau) \propto \tau^{-1/2}$ except between 0.1 s and 10 s, where the frequency drift could not be cancelled effectively with the feedback whose time constant was a few seconds (Figure. 3.6d).

3.2.5 Rat magnetocardiography

Rat cardiac conduction system

Cardiac activity in a rat [62] is triggered by electrical impulses. An increase in voltage depolarizes a fraction of the cardiac tissue into a positively charged state, while the remainder of the tissue stays polarized in a negatively charged state. A subsequent decrease in voltage repolarizes this fraction into the negatively charged state. This potential difference yields electric currents flowing from the depolarized (positive) area to the polarized (negative) area. Thus, a two-dimensional current wavefront appears at the boundary of these two areas. Both current wavefronts associated with depolarization and repolarization spread from the base to the apex [57]. Current dipoles are distributed at the current wavefront with negativity on the depolarized side and positivity on the polarized side. By integrating all current dipoles, one finds that the overall current flows from the negativity toward the heart base to the positivity toward the apex during almost the entire contraction cycle. However, the local currents present a more complicated pattern due to the complex nature of the path of electrical impulses explained below. The sinus node near the base of the heart triggers an electrical impulse. The impulse first excites the right and left atria. Following this impulse, an electric current gradually spreads from the top right to the bottom left atrium. Via sinus-atrioventricular internodal pathways, the impulse simultaneously reaches the atrioventricular node. Delayed a few milliseconds at the atrioventricular node, the impulse then passes through the bundle of His and down the right and left bundle branches. Because the upper part of the rat's ventricular myocardium is in contact with the His bundle, depolarization of the ventricle occurs from the upper part of the ventricle. At this time, the direction of the current points from the base of the heart to the apex. These bundle branches are fibres specialized for rapid impulse transmission and terminate in Purkinje fibres. In the His-Purkinje system, the papillary muscle is excited earlier than the ventricles, thereby preventing blood flow through the atrioventricular valves. In the Purkinje fibre, the left and right impulses depolarize each ventricle. Immediately before depolarization is completed near the right ventricle base, the current direction reverses, directed upward towards the right ventricle. Finally, repolarization begins in the other parts of the ventricle. This current travels from the base of the right ventricle to the apex. Consequently, the current vectors associated with depolarization and repolarization cancel each other. When depolarization is complete, only the vector of repolarization remains, and the current reorients from the base of the right ventricle to the apex. Finally, repolarization is completed earlier in the right ventricle than in the left ventricle. Furthermore, a considerable amount of electric current flows through the tissue in the lungs and fluids surrounding the ventricles, as they also efficiently conduct electricity.

Effect of laser heating of diamond on rats

In this experiment, the primary source of NV-diamond heating was laser excitation. During the magnetometry operation, the average optical intensity of the laser light traveling through the diamond was $0.55\text{kW}\cdot\text{cm}^{-2}$, and the diamond temperature increased to 70°C, which was determined from CW ODMR measurements. The laser-induced heating of the diamond shifted the resonance frequency by $\sim$ 2 MHz/W around 0.5-3.0 W. The polycrystalline diamond coverslip absorbed the heat and transferred it to the aluminum holder, resulting in a measured back-surface temperature of $<$ 50°C. The temperature profile of the setup was consistent with the Autodesk CFD software package's numerical simulation results. From these results, the temperature at the heart location was estimated to be 35-40°C, depending on the phase of the cardiac motion. The temperature rise at the location of the rat was acceptable, as its body temperature was $\sim$ 36-38°C.

Influence of vibration of rat's heart

The distance between the microwave antenna and rat heart variates due to heart beats on the measurements of Magnetocardiography (MCG) in the animal experiments. The vibration of dielectric media also could couple to microwave antenna and change its transmission at a particular frequency. To evaluate the influence of this variation, a change in the efficiency of the near field coupling between antenna and diamond arising from the motion of the sample/specimen, we have performed the electromagnetic field simulation (Keysight EMPro) based on a finite element method. Our calculation reveals that the energy of microwaves emitted from our broad-resonance antenna changes by ~ 2 dB when the standoff distance varies from its maximum to minimum values due to a reduction of the antenna's transmittance and absorption of magnetic field lines by the animal. This 2 dB change corresponds to a $\sim 4\%$ reduction in the slope of the lock-in ODMR spectrum according to our calibration measurement (Figure. 3.6a).

Mechanism of ventricular tachycardia and fibrillation

The solid-state quantum sensor would be a suitable platform for studying ventricular tachycardia and fibrillation (VT/VF). VT/VF are the major cause of sudden cardiac death, which accounts for about half of cardiac mortality [63]. Approximately 100 years has passed since the proposal of the concept that VT/VF are initiated and sustained by electrical rotational activity, also known as rotor, formed by the failure of the cardiac excitatory wave [64], but especially for VF, no essential treatment method has been established. Recent clinical studies have reported that the abnormal excitation from the Purkinje fibres and papillary muscles play an important role in initiation and maintenance of VF [65]. With a millimeter-scale resolution offered by the solid-state quantum sensor, the mechanism of such abnormal excitation may be investigated in more detail.

3.2.6 Further sensitivity improvement

Sensitivity improvement - optical engineering

Our solid-state quantum sensor continuously excites NV centres via a high-power laser. Although this scheme is common in bulk ensemble magnetometers, especially for biological application [20, 59, 66], its photon shot-noise-limited sensitivity is several thousand times larger than the ideal spin projection-noiselimited sensitivity [44] primarily because of the low total photon detection rate $R_{\mathrm{det}=\beta N_F R_F}$. The collection efficiency $\beta = 6\%$ is currently limited by the low numerical aperture detection scheme, while it can, in principle, reach nearly unity. The number of NV centres emitting fluorescence N_F is mainly limited by the laser illumination volume, which is still one-tenth of the whole diamond volume. The emission rate per NV centre is currently $R_F = 32$ kHz, while it is fundamentally limited by the NV centre's optical saturation [56] to be $R_F^{\mathrm{sat}} \sim 10$ MHz. It is, however, challenging to fill this gap by simply increasing the illumination laser power. Indeed, the laser power required to reach this fundamental limit under the same laser beam width amounts $P_0^{\mathrm{sat}} \sim 600$ W. Furthermore, the laser power required to maintain a certain emission rate increases significantly as the illumination volume increases. Below, we discuss alternative optical engineering approaches to improve the total photon detection rate.

Existing approaches to higher β include using a trapezoidal-cut diamond chip and a parabolic concentrator to enhance collection efficiency [67] ($\beta \approx$ 60-65% in theory), positioning detectors close to the diamond surfaces [68, 69]($\beta \approx$ 40-50% in measurement) and fabricating light-guiding nano-structures on the diamond surface [70–73]. In particular, Kim et al [74]. recently employed an on-chip photodiode to enable a CMOS-integrated solid-state quantum sensor. A primary approach to a higher $N_F R_F$ without increasing laser power is to extend the laser path length via internal reflection [48], where the laser beam is circulated multiple times using surface-coated metals. In practice, it may be problematic for certain applications to incorporate such experimental complexity associated with the approaches mentioned above [75]. Nevertheless, we expect that the techniques reviewed here can be introduced to next-generation solidstate quantum sensors to achieve $\beta \sim 50\%$ and a nearly twofold enhancement in $N_F R_F$. Furthermore, one can gain another factor of two by suppressing the residual laser noise, which occupies almost half of the remaining noise. With these improvements, the sensitivity must reach $\eta \sim 20\mathrm{pT} \cdot \mathrm{Hz}^{-1/2}$. When divided by the illumination volume $V_L = 0.19\mathrm{mm}^3$, the volume-normalized sensitivity is $\eta^V = \eta\sqrt{V_L} \sim 9\mathrm{pT} \cdot \mathrm{Hz}^{-1/2} \cdot \mathrm{mm}^{3/2}$.

Sensitivity improvement - Ramsey and quantum-assisted protocols

The Ramsey protocol can further improve the magnetic field sensitivity, because the pulsed readout scheme generally provides higher contrast and avoids the effect from the laser and microwave power broadening of the linewidth. Below, we discuss to what extent the sensitivity is improved by pulsed techniques for our solid-state quantum sensor. A typical Ramsey scheme for an ensemble of NV centres with initialization time t_I, free precession time t, and readout time t_R has a shot-noise-limited sensitivity of

$$\eta = \frac{\hbar}{g_e \mu_B} \frac{1}{n_\sigma \sqrt{Nt}} \frac{1}{e^{-(t/T_2^*)}} \sqrt{1 + \frac{1}{C_R^2 \beta \eta_\gamma}} \sqrt{\frac{t_I + t + t_R}{t}} \tag{3.8}$$

where n_σ is the difference in spin quantum number between the two interferometry states, C_R is the Ramsey signal contrast, defined as the difference divided by the sum of the collected fluorescence at the maximum and minimum of the Ramsey fringe, and n_γ is the number of photons emitted per Ramsey sequence. The free precession time yields an optimum sensitivity for $T_2^*/2 \leq t \leq T_2^*$, depending on the value of overhead time $t_I + t_R$. If we assume a double-quantum measurement ($n_\sigma = 2$), $N = N_F/4 = 2.2 \times 10^{13}$, a reduced coherence time of $T_2 \sim 200$ ns due to a twice larger sensitivity of the double-quantum scheme to the environmental noise, $C_F \sim 5\%$, $\beta = 50\%$, $n_\gamma = 0.01$ photon, and typical values of $t_I = 1\mu$s and $t_R = 300$ ns , the expected sensitivity reaches $1.9\text{pT} \cdot \text{Hz}^{-1/2}$, yielding a volumenormalized sensitivity of $\sim 0.8\text{pT} \cdot \text{Hz}^{-1/2} \cdot \text{mm}^{3/2}$. Indeed, Hart et al [76]. recently demonstrated $1.1\text{p} \cdot \text{Hz}^{-1/2} \cdot \text{mm}^{3/2}$ sensitivity by employing a modified double-quantum technique called double-quantum 4-Ramsey, which cancels microwave pulse errors as common-mode noise and enhances the homogeneity of the sensitivity over a large volume. As an alternative solution, Zhang et al [77]. demonstrated $0.9 - 2.1\text{pT} \cdot \text{Hz}^{-1/2} \cdot \text{mm}^{3/2}$ sensitivity by combining pulsed microwaves and a weak continuous laser. An additional advantage of the pulsed scheme will be facilitated in combination with other quantum techniques for improving T_2^*, C_R, and n_γ. Employing the NV-diamond sample used in this study, we expect a 15-fold improvement in T_2^* by decoupling the surrounding spin impurities (primarily P1 spins). Techniques such as preferential NV orientation, nuclear-spin-assisted readout, and charge-stateconversion can enhance C_R and n_γ, leading to a 6-fold improvement in the readout fidelity. These schemes combined with the above-mentioned techniques will lead to a magnetic field sensitivity of $50\text{fT} \cdot \text{Hz}^{-1/2}$, yielding a volume-normalized sensitivity of $22\text{fT} \cdot \text{Hz}^{-1/2} \cdot \text{mm}^{3/2}$.

3.2.7 Standoff distance and sensor scale

Diagram for scale of standoff distance using diamond/ optically pumped magnetometers (OPM) sensors

The standoff distance between the sensor and heart and the sensor volume is crucial for spatial resolution. To show the standoff distance and sensing volume of diamond and OPM sensors, a side view of experimental setups is shown in Figure. 3.20. For diamond NV centres, the standoff distance and sensor area are ~ 6-8 mm and $\sim 3 \times 0.35\text{mm}^2$, respectively. For OPM sensors, the standoff distance and sensor area are ~ 14 mm and $\sim 3 \times 3\text{mm}^2$, respectively. The size of the rat heart is typically ~ 11-12mm.

3.3 Results

3.3.1 Custom-built NV-MCG system and its magnetic sensing performance

Our experimental setup is a custom-built magnetic field sensing system (Figure. 3.8a and Figures. 3.1-3.3). The rat specimens used in this study were 10-11-week-old males, anaesthetised, thoracotomized, and maintained for 5 h using an artificial respirator (Figures. 3.4 and 3.5). The heart was lifted using nylon thread for further exposure outside the body. This vivisection and heart-lifting allowed the sensor to be placed a millimetre away from the heart surface. However, it is noted that these invasive procedures could alter the path of return currents as the heart was not in contact with surrounding tissues. The core of our sensor consisted of a single-crystal diamond chip containing high-density ($\sim 8 \times 10^{16}\text{cm}^{-3}$) electronic spins associated with negatively charged NV centres oriented in the z-direction of the laboratory frame. The ground-state energies of the NV centre $m_s = \pm 1$, which depend on an external magnetic field, were interrogated with a green laser and microwaves at room temperature (Figure. 3.8b). An ensemble of $\sim 1.5 \times 10^{13}$ of these NV centres in a laser illumination volume of 0.19mm^3 was used to detect the z-component of the magnetic fields generated by electric currents flowing through each rat's heart (with a thickness of 11 mm) placed directly under the sensor with 0.6-2.0 mm proximity relative to the heart surface (Figure. 3.8c). As explained in Figure.3.8d, the time-varying cardiac magnetic field Bz (t) was converted to a change in fluorescence from the NV centres using the frequency-modulated optically detected magnetic resonance (ODMR) scheme [20, 53, 59] (see also Figure. 3.6). As a benchmark, we first evaluated the magnetic field sensitivity, stability, temporal resolution, and field dynamic range of our sensor in the absence of a rat. Figure 3.8e presents a measured magnetic field sensitivity $\eta_m = 140\text{pTHz}^{-1/2}$ across the rat's cardiac signal bandwidth of 200 Hz, determined from the sensor's noise floor obtained by the Fourier transform of the raw timedomain data. This magnetic field sensitivity, seven times above the shot noise $\eta_\gamma = 19\text{pTHz}^{-1/2}$, was achieved using three well-established noise suppression techniques: low-frequency electronic noise avoidance by lock-in upconverting [20, 53, 59] at a typical modulation frequency of $f_{mod} =$ 17-25 kHz, laser fluctuation cancellation by subtracting a pick-off laser beam signal from the red fluorescence signal [20,53,59], and temperature drift compensation by monitoring double resonance peaks corresponding to the $ms = 0 \leftrightarrow \pm 1$ transitions simultaneously [48, 78]. This level of sensitivity was maintained stably over 3 h using

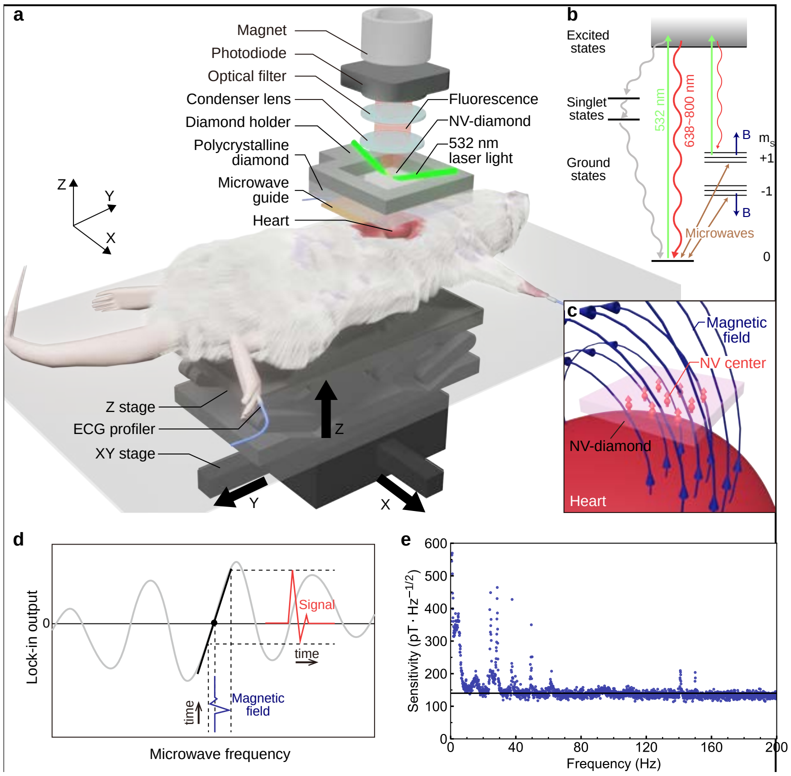

Figure 3.8: Magnetocardiography based on a solid-state quantum sensor. a Schematic of the rat magnetocardiography (MCG) setup. A living rat's heart remains approximately one millimetre below a diamond chip containing an ensemble of nitrogen-vacancy (NV) centres. The rat is scanned automatically along the XYaxes for magnetic field mapping and manually along the Z-axis for height adjustment. An electrocardiography (ECG) signal is monitored through ECG profilers concurrently with the MCG. The NV centres are excited by a 2.0 W green laser light. This excitation entails spin-state-dependent fluorescence collected by an aspheric condenser lens. b NV centre energy level diagram. The mS = ±1 ground states are split by a bias magnetic field and mixed by microwaves resonant with the NV transition frequencies. Each of the ground states are further split by hyperfine interactions with the host 14N nuclear spin. c Enlarged view of the heart and diamond. Electric currents flowing through the heart generate a circulating field (blue arrows). The NV centres (red arrows) along the [111] orientation are sensitive to the Z-component of the magnetic field. d Magnetometry principle. The time-varying cardiac magnetic field (blue), which shifts the NV transition frequency, is converted to a change in the lock-in-demodulated fluorescence signal (red). Five peaks are observed in the lock-in optically detected magnetic resonance (ODMR) spectrum because three hyperfine transition frequencies are excited with three-tone microwaves. e Magnetic field sensitivity across the rat's heart signal frequency band of DC∼ 200Hz. The black dashed line indicates 140pTHz$^{-1/2}$.

a microwave feedback system, which compensated for the long-term resonance frequency drift caused by environmental magnetic and thermal noise. Within this total measurement time, Allan deviation consistently dropped up to 500 s, which was long enough to cover any single point measurement conducted in this work. The temporal resolution, estimated to be $\Delta t = 0.34$ ms from the 10-90% rise time with a roll-off of 24 dB/octave and a lock-in time constant of $\tau_{LIA} = 50\mu$s, was fast enough to capture the signal profile. With a full-width-half-maximum ODMR linewidth of 2.1 MHz and a lock-in deviation frequency of f_{dev} = 360-400 kHz, the approximate magnetic field dynamic range, with a less than 3% loss in sensitivity, was estimated to be $\pm 2.5\mu$T, comfortably above the typical magneto-cardiac signal of nanoteslas. Therefore, our NV sensor offered sufficiently high performance for detecting the rat's cardiac magnetic fields at a short standoff distance ($\sim$ 6-7mm) (see 3.2.4 and Figures. 3.9 and 3.7).

For a longer distance, however, an OPM was used complementarily because the NV sensor could not detect the signal (~picoteslas) with a good signal-to-noise ratio (SNR).

3.3.2 Demonstration of cardiac magnetic field sensing

Next, we performed MCG measurements concurrently with ECG signal detection. The obtained MCG signal was assessed from the following five viewpoints. First, as presented in Figure. 3.10a, the MCG signal and corresponding ECG data of rat A exhibited the same periods of the cardiac pulse cycle, manifesting that the magnetic signals originated from the rat's cardiac activities. Second, the MCG signals of two additional rats (labelled B&C) were acquired, supporting the result's reproducibility among rats A-C (Figure. 3.10a-c). Third, our MCG signal presented a similar profile to what was obtained from rat D with an OPM (Figure. 3.10d), fulfilling inferential reproducibility between the two different methodologies. The Fourier transform of the signals (Figure. 3.11) also show a similar frequency spectrum. Fourth, both the NV and OPM data were explained by the same current dipole model (see Methods) with the standoff distance from the centre of the heart to the sensor as a predictor variable (Figure. 3.10e). This agreement encourages that these two types of sensors can also be used complementarily for extending the measurement space coverage. Fifth, the SNR, defined as the mean signal peak amplitude ratio to the root mean square noise, is scaled as the square root of the number of averages, indicating that the obtained MCG signal was a consequence of averaging over consistent repetitive peaks of similar temporal profile (Figure. 3.10f). We also excluded

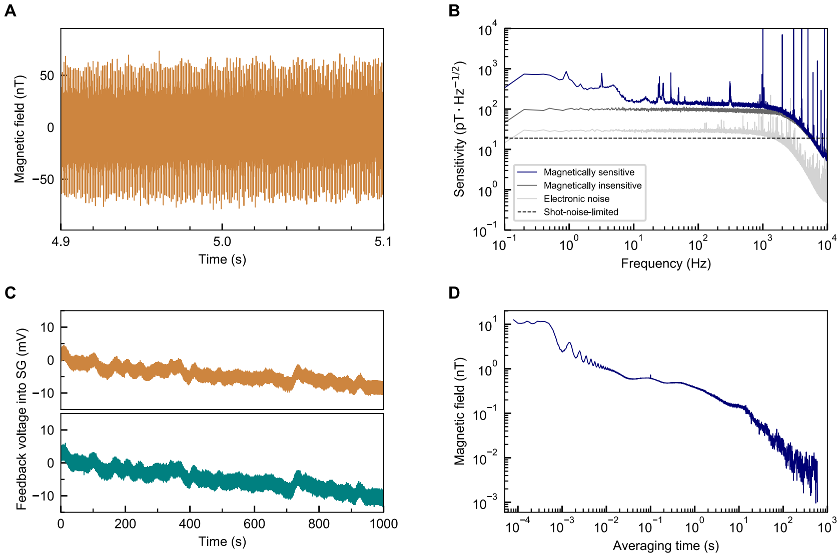

Figure 3.9: Sensitivity and stability analysis. a, Typical raw unfiltered timedomain magnetic signal ($m_s = 0 \leftrightarrow 1$ transition). Low frequency and power line hum noise (50 Hz and its higher harmonics) ranging between -50 and +50 nT are dominant. b, Noise spectrum of magnetically sensitive configuration (blue), magnetically insensitive configuration (grey), electronics noise measured without the presence of laser and microwaves (light grey), and shot-noise (black dashed line). The spectrum decreases above 1 kHz due to the filtering of the lock-in amplifier. c, Typical microwave feedback voltage sent into signal generators for $m_s = 0 \leftrightarrow -1$ (amber; upper panel) and $Wx = 0 \leftrightarrow +1$ (green; lower panel) transitions. d, Allan deviation of the measured magnetic field as a function of averaging time

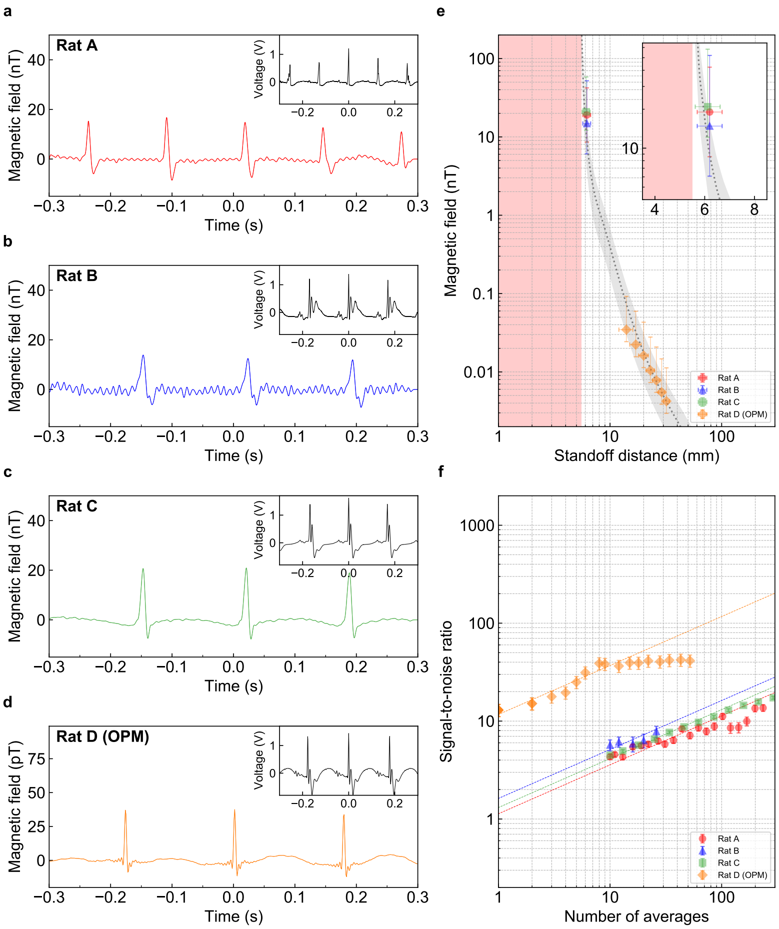

Figure 3.10: Time-domain cardiac magnetic field signal. a-d Typical time-domain magneto-cardiac signal from rats A, B, C, and D, detected with the solid-state quantum sensor (rats A-C) and an optically pumped magnetometer (OPM) (rat D). The insets show electrocardiography (ECG) signals recorded simultaneously. The peaks correspond to the R-wave, the repetition rate of which matches that of ECG. e Dependence of the cardiac magnetic field strength at the R-wave peak on the standoff distance d from the heart centre to the sensor. The vertical error bars reflect an indeterminacy of the sensor position in the XY direction relative to the point of the maximal magnetic field. The horizontal error bars represent the systematic error due to an inaccuracy in measuring the standoff distance. The grey dashed line is the magnetic field calculated from a multiple-current-dipole model with a total dipole $Q = (1.4 \pm 0.2) \times 10^3 \mu$Amm (fitted). The grey shaded area also reflects an indeterminacy of the sensor position. The pink shaded area represents the heart domain. f Dependence of the measurement signal-to-noise ratio (SNR) on the number of averages of the cardiac pulse N_{ave}. Dashed lines show the fitted model $SNR \propto N_{ave}^{1/2}$. For the solid-state quantum sensor (rats A-C), square-root dependence is observed. By contrast, for the OPM, the SNR saturates at ~ 40, possibly due to the residual environmental magnetic field that cannot be removed by the magnetic shield. Error bars are calculated from the signal, measurement noise, and the number of averages.

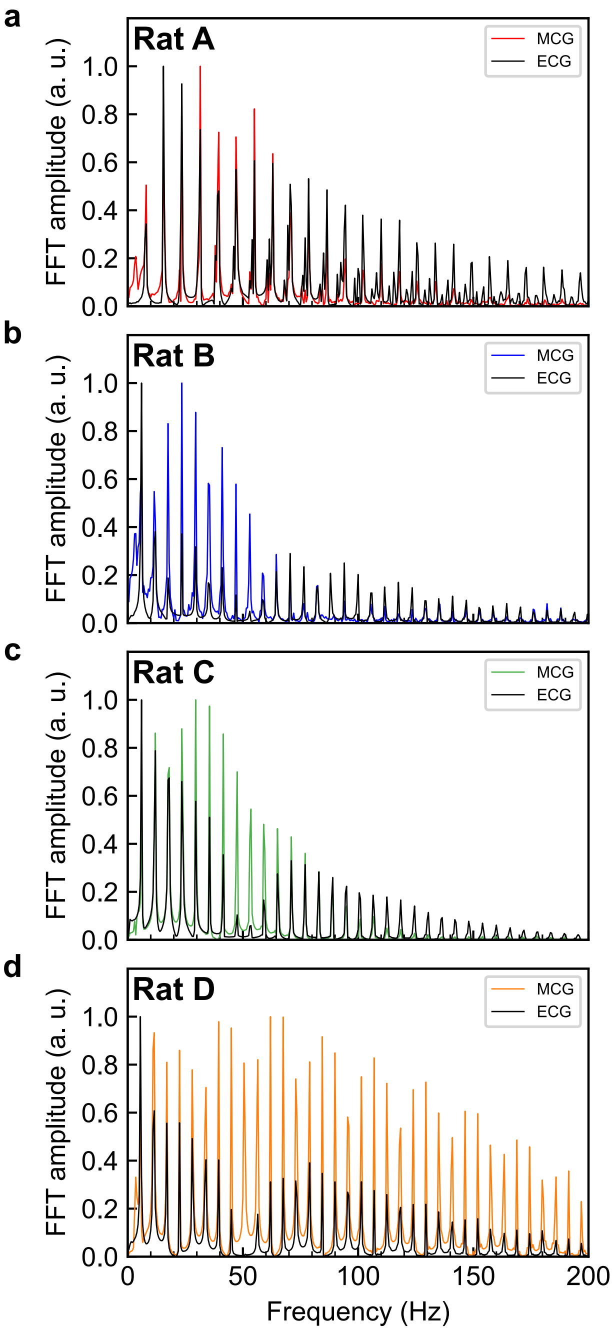

Figure 3.11: Comparison of Magnetocardiography (MCG) and Electrocardiogram (ECG) signals in the frequency domain. a-d, Absolute value of the Fourier transform of the 2-s time domain MCG and ECG data for rat A-D. The observed fundamental frequency is rat A: 7.8 Hz, rat B: 5.9 Hz, rat C: 6.0 Hz, and rat D: 5.5 Hz.

the possibility that some spurious noise sources synchronised with the rat's cardiac activity contaminated the magnetometry signal via additional laser light, pressure, temperature, microwaves, or magnetic field on the diamond. One such possible source was the rat heart's physical vibration. We frequently verified that the rat's body did not contact the diamond sample holder using a camera and our eyes during the experiments. The vibration might have also travelled through the rat's translation stage, breadboard, diamond holder, and air. According to our estimation, however, the amplitude of such vibrations was negligibly small. Besides, its natural frequency could change due to a mismatch of Young's modulus of various materials through such a channel. The vibration of dielectric media could also couple to the microwave antenna and change its transmission at a particular frequency. This effect could introduce 4% contamination according to our numerical simulation of microwave emission based on a finite element method (See 3.2.5). Another source was the reflected light from the rat's heart returning to the diamond, generating additional fluorescence. Because a copper tape attached to the backside of the polycrystalline diamond coverslip blocked the laser light, almost no power reached the rat's heart. Even if all reflected light had returned to the diamond, it would have added a spurious signal of a few orders of magnitude below the sensitivity limit. The other source was the transmission of the heat of the heart to the diamond through air convection. Our numerical simulation using Autodesk CFD showed that the 40 °C heart moving back and forth at 6 Hz changed the diamond temperature by no more than 500 K. Furthermore, this effect was removed by the double resonance detection scheme. From these considerations, we concluded that the acquired signal was the rat's cardiac magnetic field.

3.3.3 Two-dimensional imaging of cardiac magnetic field at the millimetre-scale

As shown in Figuress. 3.12 and 3.13, the solid-state quantum sensor has the ability to perform cardiac magnetic field mapping, revealing intra-cardiac current dynamics. In the following measurements, the diamond was fixed to the laboratory frame, while rat E was scanned horizontally in two dimensions with respect to the diamond across 11 × 11 pixels with a step size of 1.5 mm, covering most of the heart within a field of view of 15mm × 15mm. An optical image of the heart in this field of view is shown in Fig. 3a. The measured standoff distance between the sensor and heart centre was $d^{\mathrm{NV}} = 7.5 \pm 0.5$mm. Under appropriate imaging conditions, the magnetic field patterns produced by the rat could be measured within 40 s per pixel

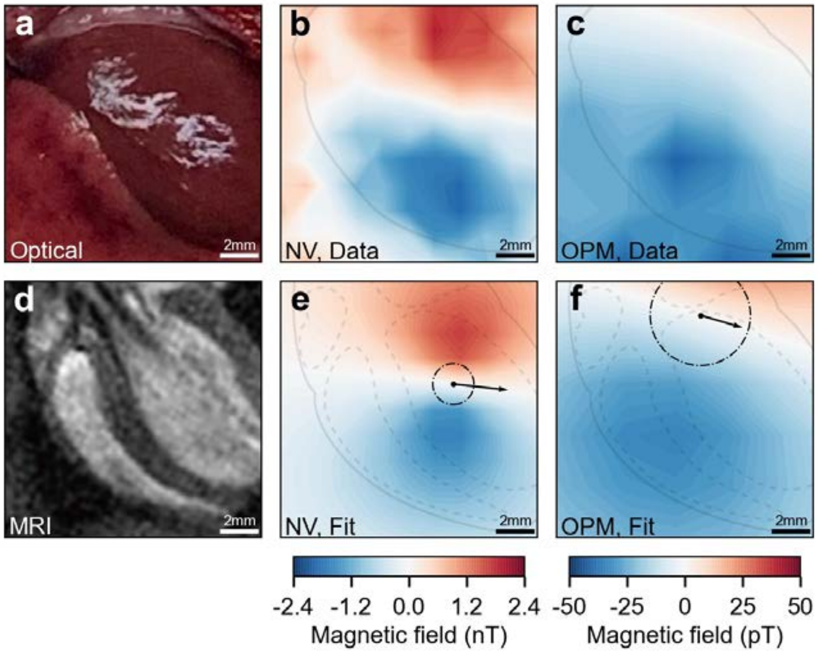

Figure 3.12: Millimetre-scale cardiac magnetic field mapping. a Optical image of the rat's heart. b, c Measured magnetic field map at the timing of the R-wave peak obtained with the nitrogen-vacancy (NV) centres for $d^{\mathrm{NV}} = 7.5 \pm 0.5$mm and with the optically pumped magnetometer (OPM) for $d^{\mathrm{OPM}} = 14 \pm 2$mm, respectively. The field of view is the same as that of the optical image, with an accuracy of better than 2 mm. The superimposed grey solid line shows the contour of the rat's heart traced from the magnetic resonance imaging (MRI) (d). d Magnetic resonance image of the rat's heart, the orientation of which is adjusted to the optical image. The Purkinje fibre bundle is located in the inner ventricular walls between the left and right ventricular. e, f Fitted magnetic field map using the multiplecurrent-dipole model, superimposed on the contour of the internal structure of the rat's heart (grey dashed line) revealed by MRI (d). The black arrows represent the location, direction, and relative magnitude of the central dipole. The black dash-dotted circle depicts the localisation precision of the central dipole. The current dipoles are estimated such that the mean squared error between the measured and simulated magnetic fields is minimal.

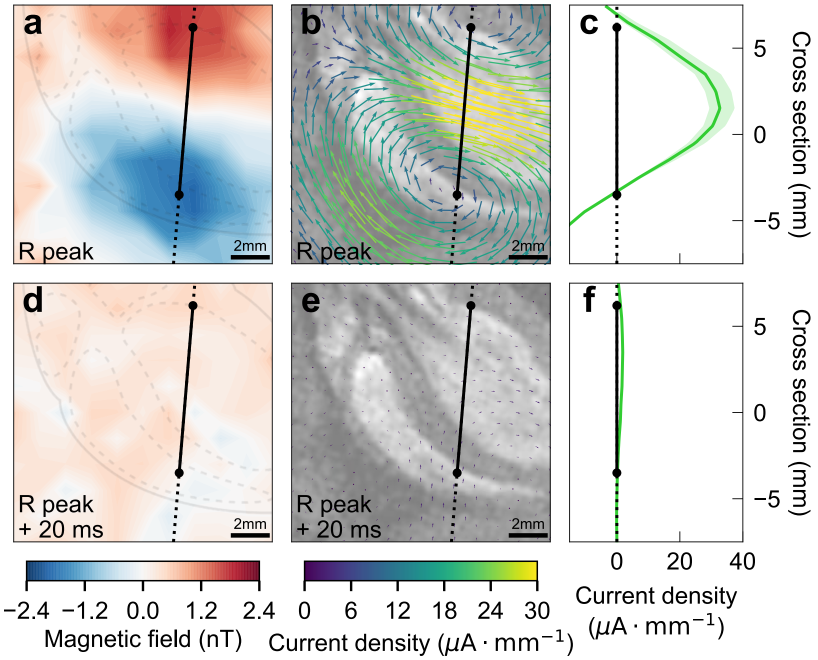

Figure 3.13: Estimation of the spatiotemporal dynamics of the cardiac current. a Measured field map at the R-wave peak, superimposed on the contour of the structure of the rat's heart revealed by optical imaging and magnetic resonance imaging (MRI). The black solid line is a linecut connecting the centres of the observed positive and negative magnetic field peaks. b Vector plots of the electric current density calculated using bfieldtools with a standoff distance of $d_{\mathrm{Q}}^{\mathrm{NV}} = 8.1 \pm 0.7 mathrmmm$. As a guide for an eye, the MRI image is superimposed in greyscale. c Normal component of the electric current density vector with respect to the linecut. The green shaded region shows the uncertainty of the current density estimated from the uncertainty of the standoff distance (one standard deviation) obtained in the dipole fitting. d-f Measured field map (d), estimated electric current density (e), and electric current density across the linecut (f) evaluated at 20 ms after the R-wave peak.

plus 40-min preparation time with minimal tissue optical and microwave radiation exposure, such that no visible damage was observed after magnetic imaging and ECG recording for ~2 h. The 40-s raw data included ~220 peaks with an expected SNR of ~8 (2.4 nT signals) after averaging. The obtained averaged data at each pixel were sliced at various timings, and corresponding magnetic images were constructed. In particular, the magnetic image at the R-wave peak presented a dipolar pattern with a pole-to-pole spacing of $\Delta^{\mathrm{NV}} = 9.7 \pm 0.6$mm (Figure. 3.12b). This spreading was smaller than that obtained from rat D with an OPM at a measured standoff distance of $d^{\mathrm{OPM}} = 14 \pm 2$mm (Figure. 3.12c).

3.3.4 Estimation of internal current dipoles as the magnetic field source

To further characterise the properties of the source electric current, we fitted each of the two measured magnetic field patterns to a magnetic field pattern simulated with a multiplecurrent-dipole model. The obtained total dipole moment for the NV data, $Q^{\mathrm{NV}} = (1.3 \pm 0.5) \times 10^3 \mu$Amm, overall agreed with that obtained with the OPM, $Q^{\mathrm{OPM}} = (1.0 \pm 0.4) \times 10^3 \mu$Amm. By correlating with magnetic resonance imaging (MRI) (Figure. 3.12d), we also found that the central current dipole, which is the geometric centre of the current flow in the heart, was located within the left ventricle near the Purkinje fibre bundle (Figure. 3.12e, f). In this measurement configuration, the resolution of the dipole moment Δr_{Q}, defined in the dipole space as the minimum separation between two current dipoles that are distinguishable through magnetic imaging measurements, was 5.1 mm for the NV and 15 mm for the OPM, manifesting the intra-cardiac scale resolving power of the solid-state quantum sensor.

3.3.5 Spatiotemporal dynamics of the cardiac current

We highlight that our magnetic field imaging results can be used to determine the time-varying source electric current density distribution $\boldsymbol{J(r)}$ on a two-dimensional plane, which can reveal spatiotemporal information about cardiac electrodynamics. The current density was calculated using bfield-tools [60, 61], a software package that employs a stream-function method to rapidly reconstruct the magnetic potential parameters via nonlinear optimisation. For simplicity, the current was approximated to flow within a flat two-dimensional plane with a standoff distance $d_{\mathrm{Q}}^{\mathrm{NV}} = 8.1 \pm 0.7$mm, as determined by the current dipole fitting. For spatial information, Figure. 3.13a, b presents the measured magnetic field pattern and estimated current density distribution sliced at the R-wave peak, revealing a current stretched in the left ventricle near the Purkinje fibre. The total current flowing through the heart, calculated by integrating the density across a linecut between the magnetic poles, was $I_{\mathrm{J}}^{\mathrm{NV}} = (2.0 \pm 0.3) \times 10^{2} \mu\mathrm{A}$ (Figure. 3.13c). For temporal information, Figure. 3.13d–f presents the measured magnetic field pattern, calculated current density distribution, and current density across the linecut, evaluated at 20 ms after the R-wave peak. As expected, almost no signal was present, resulting in a total current of $I_{\mathrm{J}}^{\mathrm{NV}} = 13 \pm 3 \mu\mathrm{A}$. This result suggests that this current density estimation method can determine the distribution of current at various timings of the electric signal propagation.

3.4 Discussion

Our demonstration using NV centres does not deny the possibility of other laboratory sensors, including OPMs and TMRs, because their standoff distance can also be as small as millimetres while maintaining high enough sensitivity and temporal resolution. In contrast, SQUIDs typically operate with sample-to-sensor separations greater than ten millimetres due to cryogenic operating temperature requirements and extended sensor dimensions. As an alternative invasive approach, electric probe arrays provide higher SNR. However, they require additional information, such as personalised rat body models and the uncertainty of the tissue conductivity [79–81], for estimating the internal current dipoles. The millimetre-scale MCG technique reported here is an essential step toward developing a tool for studying various cardiac diseases. As an initial step towards this goal, our sensor combined with the two current models will allow more precise observation of the origin and progression of cardiac imperfections, such as spiral re-entry and abnormal automaticity involved in the pathogenesis of tachyarrhythmias [82, 83], by using small mammalian model animals. A limitation of our approach is that the thoracotomy procedure can alter the current dissipation channel from the heart surface to the other body tissues. However, the influence of the limitation is relatively less because the electric conductivities of the bone and lung are very low compared with that of the heart tissues [84]. For further clinical research where the alternation of the current dissipation channel is important, the influence originating from the current dissipation can be compensated by using a numerical calculation based on the finite element method [85]. The invasive MCG technique we propose has a significant value of contactless measurement for atrial fibrillation, as explained for the following reasons. Although the wearable/flexible ECG using contact electrode arrays can detect the cardiac electric signal with a millimetre-scale resolution [86], the signal is possibly influenced by the tissue's nonuniformity in the heart, and contact failure might occur due to the heartbeat. In contrast, the MCG, based on the contactless observation of the cardiac magnetic signal, does not suffer from such effects. A contactless optical mapping technique can also demonstrate cardiac electrophysiology with a millimetre-scale resolution [87, 88]. However, this technique employs the fluorescence dye that generates toxicity to cells and tissues [89]. Our MCG technique provides a contactless method without toxicity to investigate the mechanism of atrial fibrillation for the heart on millimetre-scale spatial resolution. Overall, the invasive MCG with millimetre-scale mapping we propose has the potential ability to reveal the mechanism of atrial fibrillation [90, 91], which is the benefit of our approach because the surgical treatment is performed under the thoracotomy procedure to treat atrial fibrillation. The applicability of our sensor can be extended further from MCG to various other biological current-driven phenomena via the following step-by-step technical improvements in magnetic field sensitivity (see 3.2.6). First, the sensitivity of our sensor approaches $\sim 20\mathrm{pTHz}^{-1/2}$ through optical engineering, which provides a severalfold improvement in the laser absorption rate and fluorescence collection efficiency. Successful approaches include multiple total internal reflections of the excitation laser beam [48] and fluorescence collection through a trapezoidal-cut diamond chip combined with a parabolic concentrator lens [67] or with directly attached photodiodes [68, 74]. Second, $\sim 1\mathrm{pTHz}^{-1/2}$ can be achieved via the incorporation of the pulsed NV control scheme. Promising approaches recently demonstrated include the double quantum 4-Ramsey protocol [76] and continuously excited Ramsey protocol [77]. Third, introducing additional quantum manipulation techniques such as magnetic impurity decoupling techniques [92] for extending the NV coherence time and quantum-assisted readout schemes [93, 94] for enhancing the NV spin-state readout fidelity would yield a subpicotesla sensitivity. This sensitivity might enable the detection of action potential propagation in muscle fibres, cerebral tissues, and the spinal cord. Finally, we also envision that our solid-state quantum sensor will add tremendous value to medicine and healthcare once the three-dimensional reconstruction of source currents at the millimetre-scale becomes available by fully exploiting the following other unique advantages of NV magnetometry. Parallelisation with CCD/CMOS camera-based detection [24,95] in place of photodetector-based detection will reduce the time of scanning the sensor. Full vectorisation of magnetic sensing by encoding all four crystallographic classes of NV centres into separate lock-in modulation bands [53] will improve the SNR and facilitate the consistency check on the current reconstruction results [96]. In addition, miniaturisation and integration via on-chip fabrication [74] may allow the NV sensor to be installed on a catheter and an endoscope. This next-generation diamond sensor with these unique features and broad modalities, combined with sub-picotesla sensitivity and ambient operating conditions, would enable rapid localisation of the cause of acute cardiac fibrillation.

3.4.1 Limitation of CW-ODMR method

To improve the sensitivity of the CW-ODMR method from the shot noise sensitivity Equation 3.5, the linewidth Δf should be narrower, the contrast C should be higher, the number of NV center N_F should be increased, and the emission rate R_F should be higher (stronger excitation light). The contrast and linewidth in the shot noise sensitivity equation of the CW-ODMR method are affected by the excitation optical intensity and Rabi frequency (microwave intensity). According to Dréau [47], the contrast C and linewidth Δf are as follows

$$C = \Theta \frac{\Omega_R^2}{\Omega_R^2 + \Gamma_p^\infty \Gamma_c^\infty \left(\frac{s}{1+s}\right)^2} \tag{3.9}$$

$$\Delta\nu = \frac{\Gamma_c^\infty}{2\pi} \sqrt{\left(\frac{s}{1+s}\right)^2 + \frac{\Omega_R^2}{\Gamma_p^\infty \Gamma_c^\infty}} \tag{3.10}$$

where $s = P_{opt}/P_{sat}$ is the saturation parameter, P_{opt} is the excitation power and P_{sat} is the saturation excitation power, and Γ_p^∞ is the polarization rate at saturation excitation power. Γ_c^∞ is the optical cycle rate at saturation excitation power. Θ is the ESR contrast of the time-resolved PL response integrated over time. Ω_R is the Rabi frequency. From Equations 3.9 and 3.10, we can increase the contrast C by increasing the Rabi frequency Ω_R and decreasing the saturation parameter s (excitation optical intensity). On the other hand, to make the linewidth Δf narrower, the saturation parameter s (excitation optical intensity) should be lower and the Rabi frequency Ω_R should be lower. Thus, it is impossible to achieve both high contrast C and narrow linewidth Δf, and there is a parameter for which shot noise sensitivity is optimal. Linewidth also becomes thicker with higher NV density, so to gain sensitivity in CW-ODMR, the volume should be increased at the optimal saturation parameter and Rabi frequency. However, increasing the volume makes it difficult to make the Rabi frequency uniform, and other problems arise. Therefore, the sensitivity of magnetic sensors using NV centers has not been updated since 2016, when $15\mathrm{pT}/\sqrt{\mathrm{Hz}}$ was achieved [20]. To overcome this situation, the Ramsey method, in which optical excitation and microwave irradiation are separated in time, is beginning to attempt to solve the above problem.

3.5 CW ODMR method antenna

This section reports the development of a printed circuit board-based loop-gap microwave resonator, used to excite $\sim$ mm^3 of diamond, allowing for high sensitivity. This design has potential to biomagnetic field measurement, despite being constructed using a commonly accessible printed circuit board fabrication process. The results of this CW ODMR antenna are summarised from the following article. Loop-gap microwave resonator for millimetre-scale diamond quantum sensors. Materials Today Communications 31(455):103488

3.5.1 Introduction

To achieve high sensitivity of the diamond quantum sensors, it is necessary to excite a volume of 1 mm3 using light and microwaves and to collect fluorescence efficiently from NV centers [77, 97]. It has been proposed to increase the optical path length by several hundred times by injecting the excitation light into the side of the diamond so that total reflection occurs in the diamond in order to use a large number of NV centers [48]. The fluorescence collection efficiency is also less than 10% because of the high refractive index of diamond (2.42), which traps the fluorescence of the NV center inside the diamond. It has been reported that a fluorescence collection efficiency of 65% was achieved by contacting the diamond surface with a compound parabolic concentrator (CPC) [67]. The commonly used microwave resonators for driving NV centers are shorted coaxial loops [53], microstrip waveguides [98] and coplanar waveguides [99]. These can drive NV centers at arbitrary frequencies, but the volume of the NV center to be driven and the strength of the microwave field are not compatible. On the other hand, planar lumped element resonators, such as split ring resonators [97], omega loop resonators [100], and patch antennas [98], can drive NV centers in a large area. For example, the double split-ring resonator of Bayat et al. has a MW field strength of 5.6 G at 27 dBm input microwave power and a root-mean-square inhomogeneity of 4.4% over a 1 mm2 region [97]. Stürner et al. have achieved a sensitivity of $344\mathrm{pT}/\sqrt{\mathrm{Hz}}$ using this double-split ring resonator [101]. However, the magnetic field uniformity of these planar structures deteriorates away from the plane. To overcome these shortcomings, metal cavity resonators [102], dielectric resonators [103, 104], and three-dimensional lumped element resonators [105, 106] have been proposed. These resonators have enabled the uniformity of the microwave field over a large volume. Zhang et al. have achieved a sensitivity of $17\mathrm{pT}/\sqrt{\mathrm{Hz}}$ using an open dielectric resonator [77]. We utilized a loop-gap resonator that is used in electron spin resonance systems [107]. However, a conventional loop-gap resonator is made by processing metal into a loop shape and cutting a narrow slit in its longitudinal direction, therefore it is difficult to process and adjust the resonance frequency. A stacked loop gap resonator with electrodes on dielectric in a metal cavity has also been proposed [108]. In this study, we propose a printed circuit board open loop-gap microwave resonator to improve the spatial uniformity of the microwave field to the millimeter volume of diamond. Moreover, our resonator can incorporate efficient optical excitation and collection, and heat dissipation.

3.5.2 Sensor system and design of the microwave resonator

Figure 3.14 shows the fabricated diamond quantum sensor. The resonator and exciter are fixed to the aluminum base, and the CPC is bonded to the diamond surface to efficiently collect the fluorescence of NV centers as shown in Figure. 3.14(a). The diamond is mounted to the aluminum base via a heat-dissipating material in the hole of the resonator and excite. The aluminum base also serves as the ground for the exciter. Excitation light is passed through the hole in the side of the resonator to optically excite the side of the diamond. A photograph of the resonator and exciter is shown in Figure 3.14(b). Details of the resonator and exciter are shown in Figures 3.14(c) and 3.14(d). The loop-gap microwave resonator surrounding the diamond was composed of four layers of loops connected by vias, except for the part where the laser passes through. The exciter consisted of a loop of similar material and size as the resonator. The characteristic impedance of the feed line of the loop coil was designed to be 50Ω. One end of the exciter was terminated at 50Ω to eliminate reflected waves. The structure of the exciter is a two-layer board. The front layer is the feed line and the back layer is the ground plane. The ground of the terminating resistor on the front layer is connected to the ground plane on the back layer and the aluminum base via a screw. Since the thickness of the spacer is 0.2 mm,

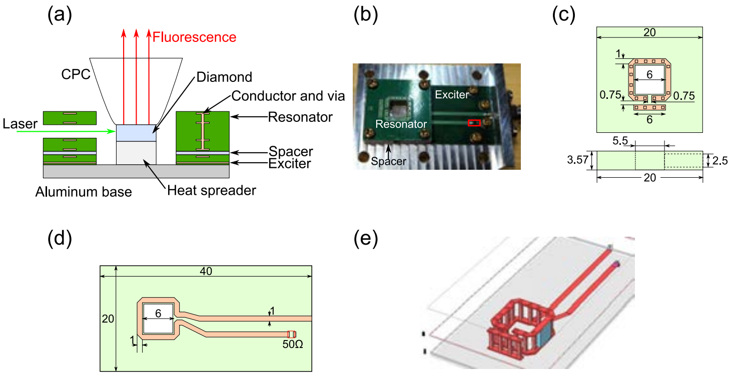

Figure 3.14: The loop-gap microwave resonator and optical system of the diamond quantum sensor (a) Schematic of the quantum sensor including the microwave resonator, exciter, CPC, diamond, heat spreader, and aluminum base. (b) The loop-gap microwave resonator, spacer, and exciter are fixed to the aluminum base. A 50Ω terminator is placed inside the red solid line. (c) Diagram of the loop-gap microwave resonator. The squares in the wiring indicate the locations of the vias. (d) Diagram of the exciter. The bottom of the feed line is terminated with a 50 Ω resistor. (e) 3D view of the wiring of the resonator and exciter conductors. The blue area is where the laser passes through.

the distance between the wires of exciter and resonator is only 0.2 mm, thus they are electrically and inductively coupled. The 3D view of the resonator and exciter is shown in Figure 3.14(e). Multi-layered loop conductors in the printed circuit board are connected by vias to enclose the entire diamond so that it functions as a loop-gap microwave resonator. The vias in the resonator loop conductors are placed at equal intervals, except where there are holes used for diamond optical excitation. The heat generated by the diamond due to the optical excitation is dissipated to the aluminum base through a heat spreader. Spacers between the resonator and exciter are used to adjust the inductive coupling between them. The direction of the microwave magnetic field is perpendicular to the surface of the loop-gap microwave resonator. The magnetic field sensitivity of the sensor at this time is determined by the shot noise limited sensitivity and is expressed by the following equation [47]:

$$\eta = \alpha \frac{h}{g_e \mu_B} \frac{\Delta f}{C\sqrt{\beta R_F N_F}} \tag{3.11}$$

Here, $alpha$ is the shape factor ($\alpha = 4/3\sqrt{3}$ for the Lorentzian case), h is Planck's constant, g_e is the g factor, μ_B is the Bohr magneton, Δf is the line width, and C is the measurement contrast. Furthermore, β is the fluorescence collection efficiency, R_F is the NV center excitation rate, and N_F is the number of exciting NV centers. To improve the sensitivity, the line width Δf should be narrowed and increase fluorescence collection efficiency and the number of NV centers. Since there is a trade-off between NV density and linewidth, increasing the volume is effective to improve the sensitivity. The sensitivity can be improved by increasing the number of NVs that can function as sensors by generating a microwave field in a large volume. A typical loop-gap resonator can be considered as an LC resonator as long as the resonator size is small ($\sim 1/6\lambda$) compared to the microwave wavelength λ. At frequencies close to the resonant frequency, a microwave field is generated uniformly in the loop inside the resonator. In a cylindrical loop-gap resonator of thickness w, radius r_0, depth l, and gap width t, the inductance L created by the loop is

$$L = \mu_0 \frac{\pi r_0^2}{l} \tag{3.12}$$

C_{gap} is the capacitance created by the gap, expressed as follows:

$$C_{gap} = \epsilon_r \epsilon_0 \frac{wl}{t} \tag{3.13}$$

where ϵ_0 is the electric constant of the vacuum, ϵ_r is the relative permittivity, and μ_0 is the magnetic constant. The resonant frequency f_0 of the loop-gap resonator is expressed as follows [109]:

$$f_0 \approx \frac{1}{2\pi\sqrt{LC_{gap}}} \tag{3.14}$$

In this study, the loop aperture of the loop-gap microwave resonator was set to $r_0 = 6$mm for a commercially available diamond up to 5 mm square. As long as we used an ordinary FR4 printed circuit board as the substrate material, the resonator size would exceed $1/6\lambda$ of the microwave wavelength because of the shortening effect of wavelength caused by the relative permittivity of the FR4 substrate. Instead of FR4, Fluoroplastic (Nippon Pillar Packing Co., Ltd. NPC-F260A-0.2) was used as the substrate material. The resonator was manufactured by Nippon Pillar Packing Co., Ltd. The inductance and capacitance of the cylindrical loop-gap microwave resonator with $w = 1$mm and $l = 3.57$mm were calculated to be $L = 40$nH and $C_gap = 0.11$pF, respectively, and the resonant frequency was $f_0 = 2.4\,$GHz. Since the resonant frequency is increased by the aluminum base for heat dissipation, the shape of the resonator was designed to have a resonant frequency close to 2.87 GHz using 3D Planar Electromagnetic software (Sonnet) based on the value of w and l above. The thickness of the copper foil of the resonator was 35μm, the thickness of the substrate was 155μm, the area through which the laser pass was 3.12mm, the thickness of the film was 50μm, and the thickness of the solder resist was 20μm. The exciter had a copper foil thickness of 35μm, a substrate thickness of 400μm, and a solder resist thickness of 20μm. The spacer between the resonator and the exciter was made of the same material as the substrate material and had a thickness of 155μm.

3.5.3 Experimental results and discussion

A homoepitaxial diamond (100) film was grown on high-pressure/high-temperature (HPHT) grown type-Ib crystals with a top (001) surface of 3.5 mm × 3.5 mm by microwave plasma chemical vapor deposition (MPCVD). The methane and oxygen concentration to the total gas flow were 10%, 2%, respectively. Nitrogen concentration (N/C) was 1000 ppm in gas phase during growth. The substrate temperature, growth duration, and thickness of diamond film are, 1050±50 °C, 171 h and 500 μm, respectively. The nitrogen concentration was expected to be 0.057 ppm. Details of MPCVD growth conditions can be found elsewhere [110]. After the diamond growth, 2 MeV electron beam

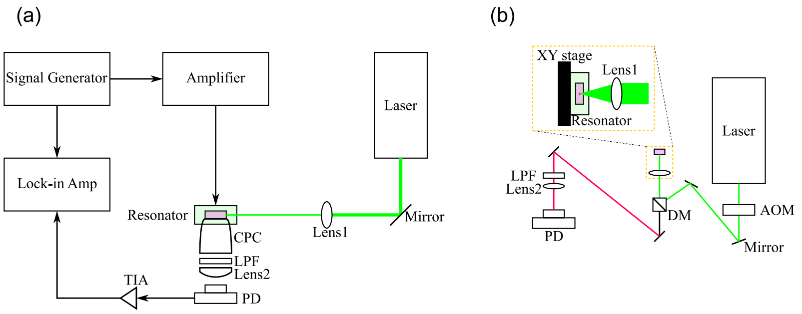

Figure 3.15: (a) Optical setup for CW-ODMR measurements. (b) Optical setup for Rabi measurement.

irradiation was applied with the total fluence of $1 \times 10^{18}\,\mathrm{e \cdot cm^{-2}}$ to create vacancies in the diamond, being followed by vacuum annealing at 1000 °C for 2 h to form NV center in the diamond crystal. After the electron beam irradiation process, CVD layer was removed the HPHT substrate to make a freestanding CVD (100) plate with a dimension of $3\,\mathrm{mm} \times 3\,\mathrm{mm} \times 0.4\,\mathrm{mm}$ by laser cutting. All 100 crystal planes of the freestanding plate were mirror polished. We used two different optical setups for DW-ODMR and Rabi measurements. Figure 3.15(a) shows an optical setup for CW-ODMR measurement. The laser is focused by a lens1 and incident on the side of the diamond in the cavity for optical excitation. The fluorescence from the diamond is collected by the CPC and focused on the PD by a lens2 after a long-pass filter(LPF). Figure 3.15(b) shows Rabi measurement optical setup. The laser is focused with a lens1 and incident on the diamond surface in the resonator for optical excitation an area of 30um diameter. Rabi measurements are performed at multiple points in the resonator by moving the XY stage. The fluorescence from the diamond is collected by a lens2 and focused on the PD by a lens after a dichroic mirror (DM) and a long-pass filter (LPF). The loop-gap microwave resonator was evaluated for resonant frequency, CW-ODMR measurement, and microwave field uniformity. The resonant frequency was measured using a network analyzer (Keysight E5080A). The S-parameter transmission coefficient, S21, was measured using an exciter with a two-port geometry. We confirmed through CW-ODMR measurements that the NV centers could be driven by microwaves using our loop-gap resonator. As shown in Figure 3.15(a) the diamond sample was placed in the center of the resonator and optically excited by laser irradiation from the side of the diamond through the hole. The diameter of the laser was $30\,\mu$m, and the NV center was optically excited over a 3 mm length in the width direction of the diamond sample. The laser incident into diamond simply punched through the diamond. The diamond surface was bonded with a CPC (Edmund Optics CPC 25DEG2.5MM EXIT UNCTD) with a laser power of 150 mW. The PD current was 106 μA. The CW-ODMR was amplified by a transimpedance amplifier and measured using a lock-in amplifier (NF LI5660). The modulation frequency, frequency deviation, time constant, and low-pass filter were 30 kHz, 300 kHz, 100 ms, and -24 dB/oct, respectively. The Rabi measurement optical setup is shown in Figure 3.15(b). The loop-gap microwave resonator and diamond were moved by an XY stage, the excitation of the NV center and collection of fluorescence were performed using a lens1 (Thorlabs AC254-030-AB-ML), and an area of 30 μm diameter was excited by a laser power of 10 mW. The obtained photodiode (Thorlabs SM1PD1A) current was amplified by a transimpedance amplifier (FEMTO DHCPA-100) at 71 nA (gain 10^6 V/A, bandwidth 1.8 MHz). The Rabi frequency becomes faster in proportion to the strength of the microwave magnetic field; therefore, the uniformity of the microwave magnetic field in the loop-gap microwave resonator was evaluated by the distribution of the Rabi frequency. The diamond sample was placed in the resonator with a crystal axis <100> parallel to the depth direction of the resonator. A static earth field B_0 was applied in the [100] direction using a permanent magnet.

Figure 3.16 shows the S-parameter transmission coefficient S_{21} of the loop-gap microwave resonator. The resonant frequency is 2.86 GHz, which is consistent with the simulation results. The Q-value of the resonator was 95 and the coupling coefficient β was 0.85. The bandwidth of the resonator was 56 MHz. This Q is lower and bandwidth is wider compared to the reported value [101]. The asymmetry in the S_{21} parameter is due to the increased reflection before entering the resonator at the high frequency region. Three resonators with different resonant frequencies were fabricated, and were performed in a manner consistent with the simulation results. This result shows that we can design a resonator with the desired resonant frequency using a simulator.

Figure. 3.17(a) shows the ODMR waveform when optical excitation light was punched through the diamond sample in the width direction, and the hyperfine structure of ^{14}N nuclear and electron spins can be clearly seen in all resonances [20, 53, 111]. The S-parameter resonant frequency and CW-ODMR spectra indicate that this system drives the NV centers near the resonant frequency. The small fluctuations between the CW-ODMR spectral peaks were mainly due to laser power fluctuations. As shown in Figure. 3.17, the intensity of the ODMR spectra was large at the resonance frequency

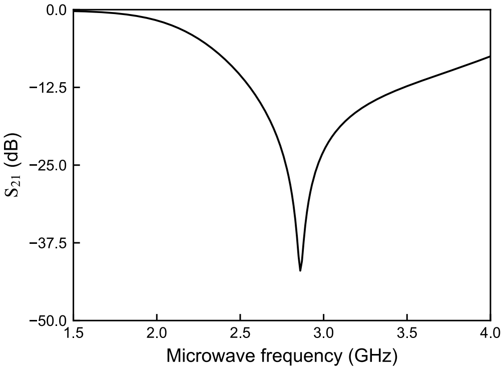

Figure 3.16: Loop-gap microwave resonator S_{21} parameter The resonant frequency was measured with two ports, and a jig for the exciter was made to allow for two-port measurements. The resonant frequency f_0 is 2.86 GHz.

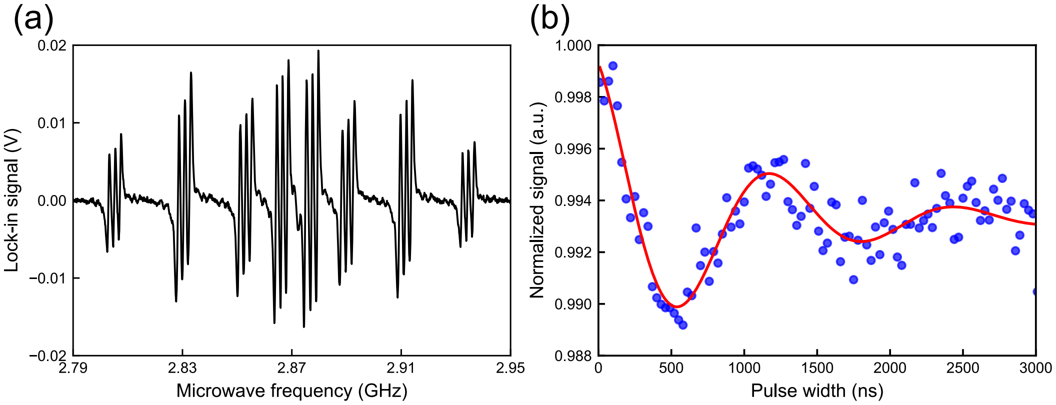

Figure 3.17: CW-ODMR and Rabi oscillation (a) A static magnetic field was applied to observe the ODMR spectra of the four NV centers. The hyperfine structure of the NV centers can be clearly seen. The NV centers are strongly driven near the resonant frequency of the resonator, making the ODMR signal strongest at the resonant frequency. (b) Rabi oscillation data near the center of the loop-gap microwave resonator. The applied MW frequency is 2.825 GHz. The data were fitted with damped cosine oscillation.

and decreased away from the resonance frequency. This confirms that this resonator is capable of driving NV centers. Fluctuations in the CW-ODMR signal strength due to the frequency characteristics of the resonator have no effect when measuring small magnetic fields because there is little frequency fluctuation. The Rabi oscillation in the NV transition is shown in Figure. 3.17(b). The low Rabi contrast is due to the presence of a relatively large number of NV0 in the sample. The laser incident power to the diamond in the Rabi measurement was 8.3 mW and the microwave incident power to the resonator was 40 W. The data were fitted with $A \exp(-t/\tau_R)\cos(2\pi f_R t)+D$ to determine the Rabi frequency. A is the amplitude, τ_R is the decay time of the Rabi oscillation, and D is the offset. The microwave magnetic field B and the Rabi oscillation frequency f_R are expressed in the following equation [112]:

$$f_R = \frac{g_e \mu_B B \sin\beta}{\sqrt{2}h} \tag{3.15}$$

where β is the angle between the NV axis and the microwave magnetic field. Because the angle between the microwave field in the <100> direction and the NV center in the [100] crystal is $\cos\beta = 1/\sqrt{3}$, the microwave field can be expressed as [113]

$$B = \sqrt{3}\frac{h f_R}{g_e \mu_B} \tag{3.16}$$

The Rabi frequency measurement area was 25 points in a 5 mm × 5 mm area, as shown in Figure. 3.18(a). The average Rabi frequency 0.87 MHz and the microwave magnetic field 0.53 G were obtained at the 46 dBm input microwave power. The Rabi frequency was slow compared to the value expected from microwave input power because the applied microwave frequency is 45 MHz away from the resonance frequency. The intensity distribution of the microwave field is shown in Figure. 3.18(b). The uniformity of the magnetic field intensity was evaluated by the standard deviation σ and peak-to-peak σ_{pp}. In the area of 25 mm^2, σ was within 0.15 G, and in the volume of 1 mm^3, σ_{pp} is within 0.27 G. The microwave field strength is weaker than those reported in Stürner et al., where the diamond is locates just above the resonator wires [101]. The microwave field strength of the loop-gap microwave resonator was simulated using commercial 3D electromagnetic field simulator software (Keysight EMPro). The simulations included resonators, exciters, and diamonds. A space of 20 mm × 40 mm × 8.8 mm was analyzed using the finite element method with a tetrahedral adaptive mesh. Absorbing boundary conditions were used as boundary conditions. The simulation results shown in Figure. 3.18(c) indicates that, σ was within

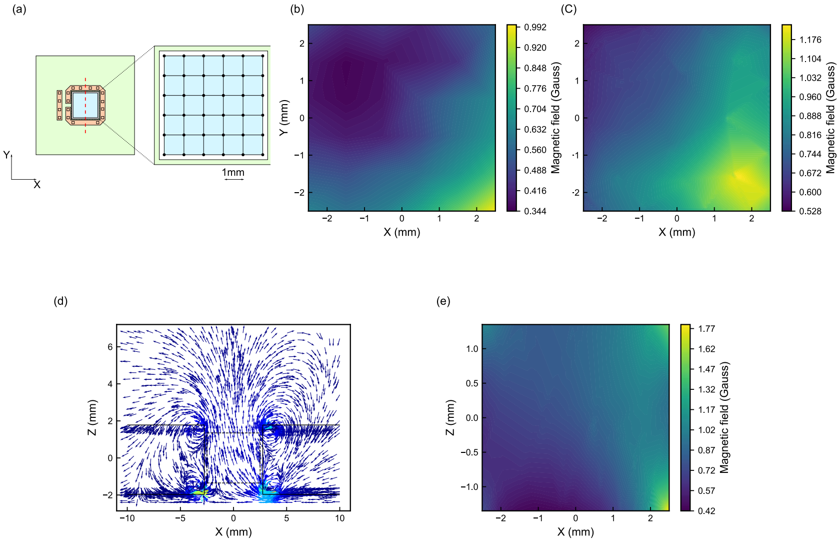

Figure 3.18: Microwave magnetic field uniformity of loop-gap microwave resonator (a) The microwave magnetic field was determined by measuring the Rabi frequency while shifting the position of the 3 mm×3 mm diamond containing NV centers (5 mm × 5 mm area at 1 mm intervals). (b) Measured microwave magnetic field at the point indicated in (a). (c) Simulation results of the microwave magnetic field. The magnetic field becomes stronger moving from the upper left to the lower right. (d) Simulation results of microwave magnetic field vectors in the XZ cross section shown in (a) with red dashed lines. The solid line shows the outline of the resonator and the dashed line shows the area where the diamond is placed. (e) Simulation results of microwave magnetic field at the XZ cross section shown in (d) by the dashed line. The area is 5 mm × 2.7 mm.

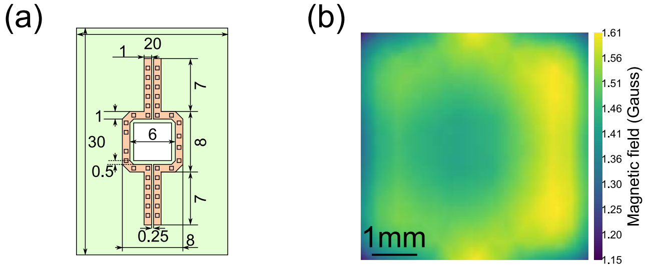

Figure 3.19: Simulation results of microwave differential input to a loop-gap resonator with two gaps. (a) Diagram of a loop-gap microwave resonator with two gaps. (b) Simulation results of the microwave magnetic field, showing a region of 5 mm × 5 mm. Compared to Figure. 3.18(c), the field distribution is improved.

0.12 G in the area of 25 mm^2 and within σ_{pp} is within 0.17 G in the 1 mm^3 volume. From the simulation results, it was found that the microwave field direction inside the resonator is generated in the Z direction as shown in Figure. 3.18(d). The microwave field strength of the magnetic field in the XZ plane (5 mm × 2.7 mm) in Figure. 3.18(e) was 0.83 G and σ was 0.23 G. The microwave magnetic field strength in the 2 mm × 2 mm area was 0.79 G and σ_{pp} was 0.43 G. The mismatch distribution between the actual measured value and the simulation result is considered to be caused by the misalignment of the measurement points and the dimensional error of the resonator. The oblique distribution of the microwave field shown in Figure. 3.18(b) is due to the unbalanced current flowing in the loop caused by the single-port microwave input. The field uniformity can be improved by using differential microwave input and multiple gaps.

The structure of the resonator is shown in Figure. 3.19(a), which has two gaps with 0.25 mm spacing on the top and bottom. Figure 3.19(b) shows the simulation results of the microwave magnetic field when microwaves are input differentially to the resonator. The microwave magnetic field distribution was improved and σ_{pp} of 0.093 G in 1 mm^3 volume. The microwave magnetic field strength is also improved due to the differential input of microwaves. The results showed that the field uniformity was also improved, and therefore we would like to perform sensitivity measurements using the improved diamond. In addition, the microwave field strength can be improved by adding a matching circuit to the exciter and impedance matching with the resonator. To achieve higher sensitivity, the use of pulsed measurements such as the Ramsey protocol is necessary. The resonator for the pulsed measurement requires further uniformity and strength of the microwave magnetic field [76]. To improve sensitivity, further improvements of diamond is necessary, such as extending T_2^* by improving ^{12}C enrichment and P1-NV conversion efficiency. The thermal resistance between the diamond and the heat sink surface is 13 K/W when the heat sink (Sankyo Thermo-Tech 33BS050-L50) is mounted on the aluminum base of our resonator and the heat spreader (AlN ceramic 4 mm × 4 mm × 1 mm) is mounted between Diamond and aluminum base in natural air cooling. To further reduce the thermal resistance, liquid cooling or forced air cooling is required. CPC bonded to the diamond surface is used for high photon collection efficiency, expected to excess 60% [67]. The excitation light was injected from the side of the diamond. The diameter of the laser was 30 µm, and the NV center was optically excited over a 3 mm length in the width direction of the diamond sample. Large-volume optical excitation can be achieved by processing the diamond and injecting the excitation light in such a way that it undergoes a total internal reflection. This loop-gap microwave resonator can be fabricated using a common multilayer printed circuit board fabrication process. The layered structure of the printed circuit board makes it easy to optically excite the diamond from the side. Since the diamond can be excited from the side, it is compatible with optical systems that improve the light collection efficiency, such as CPC. The loop-gap microwave resonator fabricated on a printed circuit board has a high degree of freedom in terms of its shape, and there is room for further improvement.

3.6 Conclusion

In this chapter, a long-time stable biomagnetic field measurement system is proposed by combining CW-ODMR with lock-in and differential measurements and temperature feedback against temperature changes, and magnetocardiographic imaging of rats was demonstrated. A microwave antenna was also proposed to enable a large sensor volume, which is effective in improving the sensitivity of the CW-OMDR method.

In magnetocardiographic imaging, we exploit a key strength of the solid-state quantum sensor the ability to bring the NV centres into proximity to the signal source under ambient operating conditions—to demonstrate the MCG of living mammalian animals and the associated electric current estimation with a spatial resolution smaller than the heart's feature size. To achieve the spatial resolution with millimetre-scale, we reduce the standoff distance under the thoracotomy procedure (see 3.2.7 and Figure. 3.20). To reconstruct the high-resolution magnetic image, we also propose an ex-

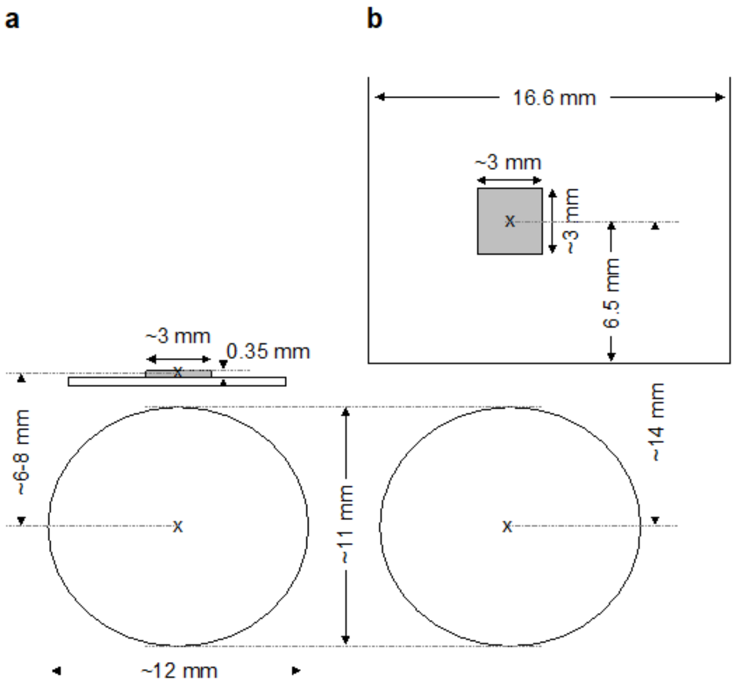

Figure 3.20: Side view of the experimental setups. a, Nitrogen-vacancy (NV) centre. b, Optically pumped magnetometers (OPM). Gray shaded parts and circles represent the sensor area and the heart, respectively. The drawings are to scale.

tended current dipole model consisting of vertically distributed dipoles. This extended dipole method and the current density estimation method determine the geometric centre of the current in three dimensions and associated current density distribution on a projected two-dimensional plane as complementary information.

Our resonator can drive NV centers within an area of 5 mm square and the uniformity of the microwave field strength was 0.53 G at the 46 dBm input microwave power. The peak-to-peak value at 1 mm^3 volume was 0.27 G. In the simulation, the peak-to-peak value in the XZ plane (2 mm × 2 mm) was 0.43 G. By using a loop-gap resonator with two gaps and differential microwave input, the peak-to-peak value at 1 mm^3 is improved to 0.093 G in the simulation. In addition, this resonator achieved compatibility both of the fluorescence collection efficiency which is considered to exceed 60% and the thermal resistance which is 13 K/W. Further improvement of the microwave magnetic field uniformity and intensity of the resonator will allow the application of pulsed measurements such as the Ramsey protocol.

Chapter 4

Development of advanced quantum protocols based on Ramsey method toward brain monitoring

In 3.4.1, we mentioned that for further improvement of magnetic sensitivity, it is necessary to increase the sensor volume in the CW-ODMR method or to apply the Ramsey method, in which the optical excitation and microwaves are irradiated separately. This chapter consists of the following two sections.

1. Development of an antenna capable of generating a strong microwave field with a wide bandwidth that can be applied to the Ramsey method with Double Quantum, and evaluation of the antenna by Rabi measurements.
2. A measurement system that enables the Ramsey method combining Double Quantum and Lock-in detection was constructed using the developed antenna, and its sensitivity was evaluated.

4.1 Ramsey method antenna

In this section, we report the development of an antenna capable of performing the Ramsey method by applying Double Quantum. The antenna uses a printed circuit board and an inverted T-shaped bandpass filter structure [114]. This inverted T-type bandpass filter can generate a strong microwave field in a wide bandwidth. Furthermore, by drilling holes in the metal wiring of the inverted T-type part, the attenuation of the microwave magnetic field intensity due to the distance from the metal line has been successfully reduced. This antenna is suitable for applying Double Quantum to Ramsey measurements using ensemble NV centers.

4.1.1 Introduction

The Ramsey method requires the sensor volume to be exposed to a strong and uniform microwave magnetic field. A resonant antenna such as a loop gap resonator [113] can generate a strong and uniform microwave magnetic field inside the resonator. On the other hand, when Double Quantum [92] is applied to the Ramsey method, two resonance frequencies of $m_s = \pm 1$, split by the magnetic field, are used. The splitting width varies depending on the strength of the applied bias magnetic field, but when a magnetic field of 1 mT is applied, the splitting width is 56 MHz. Therefore, there is little merit in using a resonator with a high Q value. In addition, when using 111 crystal diamond, which is advantageous for biomagnetic field measurement, a microwave magnetic field perpendicular to the direction of the magnetic field generated by the loop gap resonator is required. Coplanar resonators [99] and double split ring resonators [97] have been used for 111 crystal diamond. However, such antennas have a narrow bandwidth, and the further away from the metal line of the antenna, the weaker the microwave field becomes. It has been shown that the bandwidth can be increased by incorporating multiple bandpass filter structures used in telecommunications and other applications. However, it is difficult to generate a broadband microwave magnetic field at a fixed diamond position because the intensity of the microwave magnetic field becomes stronger at the design frequency of each stage of the bandpass filter. Therefore, we focused on a invferted T-type bandpass filter [114], which is a variant of the side-coupled single-stage bandpass filter. This filter operates as a parallel-coupled microstrip line. The antenna has a position where a strong microwave field strength with a wide bandwidth is generated. By fixing the 111 crystal diamond at this position, a broadband microwave field perpendicular to the NV center axis is generated. However, this antenna does not solve the problem that the microwave magnetic field becomes weaker as the distance from the metal line of the antenna increases. We have therefore focused on the fact that the presence of holes in the metal line cancels the microwave magnetic field with the magnetic field on the back side of the metal line, thereby reducing the variation in the intensity of the microwave magnetic field in the direction perpendicular to the line. We thought that by applying this idea, we could

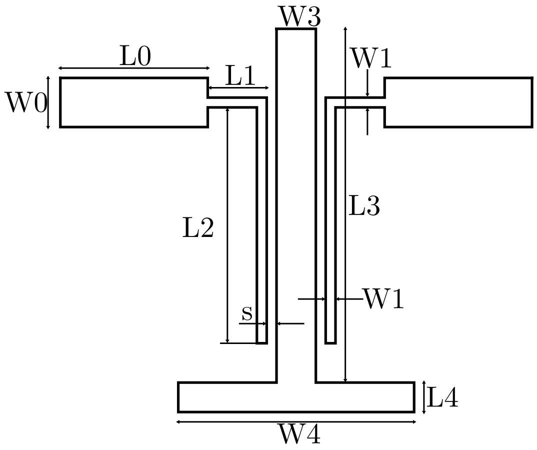

Figure 4.1: Antenna Geometries. This antenna is composed of two parallel coupled wires with an inverted T-shape.

reduce the variation of the microwave magnetic field strength by drilling holes at the positions where diamonds are fixed.

4.1.2 Anttena Design

Figure 4.1 shows the appearance and dimensional parameters of the antenna created in this study. The basic element of this antenna is a parallel-coupled microstrip line. This antenna consists of two parallel coupled lines with inverted T-shape [114]. This antenna is considered to have ideal parallel lines with an electrical length that is 1/4 wavelength of the design frequency. And the lines with inverted T-shape have different lengths and widths. The design parameters $L0, L1, L2, L4, W0, W1, W3, W4$, and s of this antenna are shown in Figure 4.1. Two electromagnetic simulators were used to determine the various parameters of the antenna. First, Sonnet was used to determine the parameters that satisfy the frequency and bandwidth of the S_{11} parameters. Next, the parameters were used to determine the magnetic field strength distribution using EMPro. CS-3376G from RISHO KOGYO CO., LTD was selected as the substrate material for the antenna because of its low dielectric constant, high strength, and good workability. A double-sided substrate with a board thickness of 1.6 mm and a copper foil thickness of 35 μm was used. The dielectric constant and loss tangent used in the simulation were set to 3.35 and 0.005, respectively. The parameter s affects the bandwidth with respect to the design frequency. In this case, s was designed so that the bandwidth where S_{11} is less than -10 dB is 200 MHz. Parameter

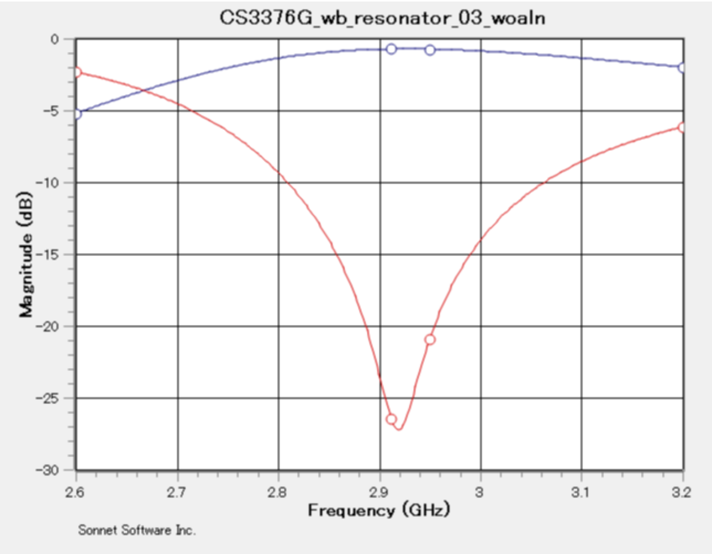

Figure 4.2: Sonnet simulation result. Results of S-parameter simulation with Sonnet to find parameters that achieve the target resonant frequency and bandwidth. red line is S_{11}, blue line is S_{21}.

$W1$ affects the characteristic impedance and was set to be well matched at the design frequency. Parameter $L2$ affects the insertion loss and the bandwidth on the high frequency side. In this case, it was set to a value that reduces insertion loss while satisfying the bandwidth. Parameter $L3$ affects both resonant frequency and bandwidth. In this case, it was set so that the resonant frequency is around 2.9 GHz while satisfying the bandwidth. The reason for setting the design frequency near 2.9 GHz was to place a 30 mm square SiC substrate on the antenna as a diamond heat sink. The resonance frequency is lowered by the SiC substrate, so the design frequency was set higher.

Figure 4.2 shows the S_{11} parameters calculated by Sonnet. The parameters shown in Figure 4.1 are $L0 = 12\,\mathrm{mm}, L1 = 2\,\mathrm{mm}, L2 = 15.5\,\mathrm{mm}, L3 = 21\,\mathrm{mm}, L4 = 3\,\mathrm{mm}, W0 = 3\,\mathrm{mm}, W1 = 0.5\,\mathrm{mm}, W3 = 2\,\mathrm{mm}, W4 = 12\,\mathrm{mm}, s = 0.5\,\mathrm{mm}$. Using these parameters, a three-dimensional electromagnetic field analysis was used to calculate the microwave magnetic field distribution. The SiC heat sink was also taken into account in this simulation. Simulations were performed with and without holes in the inverted T-shaped metal line section, and the vertical distribution of the microwave magnetic field was compared.

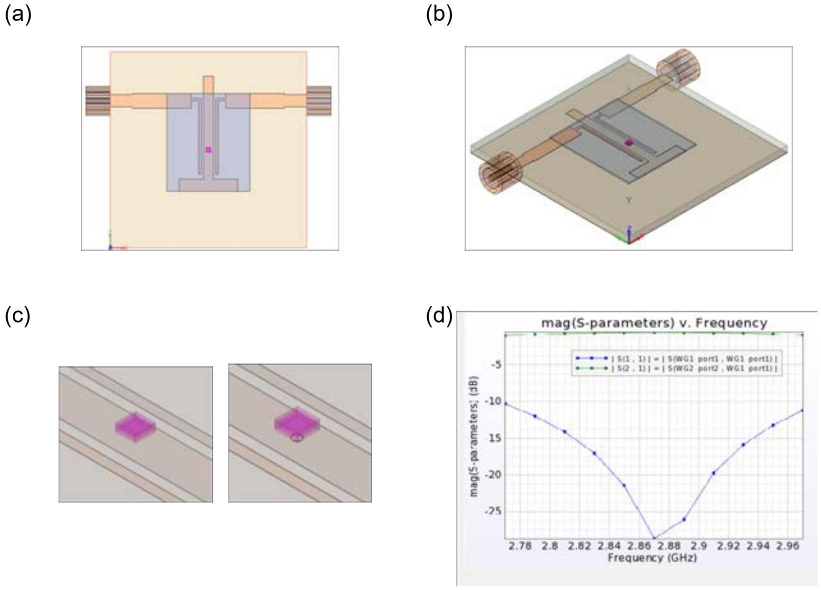

Figure 4.3: Three-dimensional electromagnetic field simulation model and S parameter result. (a) Three-dimensional view of the antenna. The blue area is the SiC heat-dissipating substrate. (b) Three-dimensional view of the antenna. The pink area is the diamond placement position. (c) Enlarged view of the diamond placement position. (d) S-parameters calculated by simulation.

Figure 4.3 shows the simulation model and S-parameter simulation results. Figure 4.3(a),(b) show the model of the antenna used in the simulation. The blue area in the figure is a 30 mm square 0.2 mm thick SiC heat-dissipating substrate. The pink region is the diamond placement position. Figure 4.3(c) is an enlarged view of the diamond placement position. The left figure shows a model without holes in the inverted T-shaped metal line. The right figure shows a model with a hole in the inverted T-shaped metal line. Figure 4.3(d) shows the S-parameters calculated by the simulation. The blue line is S_{11} and the green line is S_{21}. The simulation without the SiC heat sink had a resonance frequency of about 2.9 GHz, while the simulation with the SiC had a resonance frequency of about 2.87 GHz. This value is equal to the zero field splitting of the NV center.

Figure 4.4 shows the simulation results of microwave magnetic field strength. Figure 4.4(a) shows the microwave magnetic field intensity distribution at different frequencies for the case without and with holes in the metal line. In the upper figure without holes in the metal line, the closer to

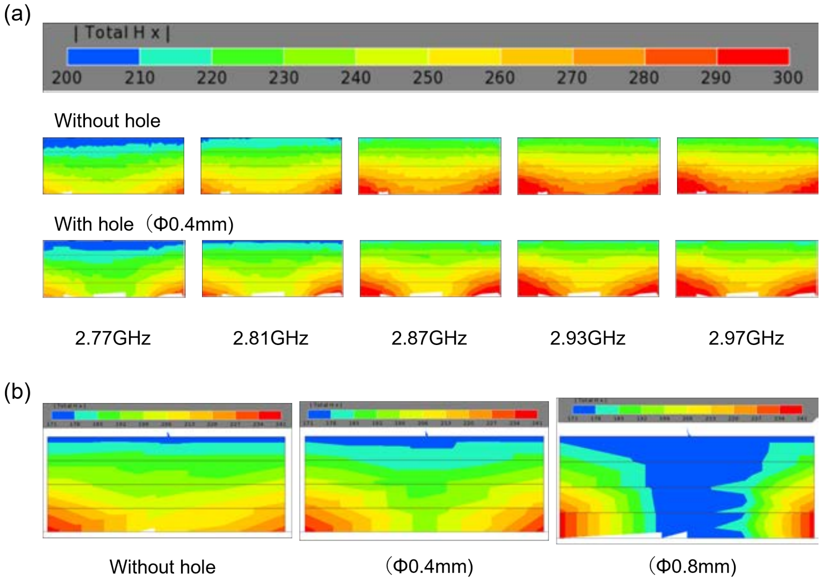

Figure 4.4: Microwave magnetic field strength (a) Microwave magnetic field intensity distribution for the metal wiring without and with holes. (b) Microwave magnetic field intensity distribution for different hole sizes.

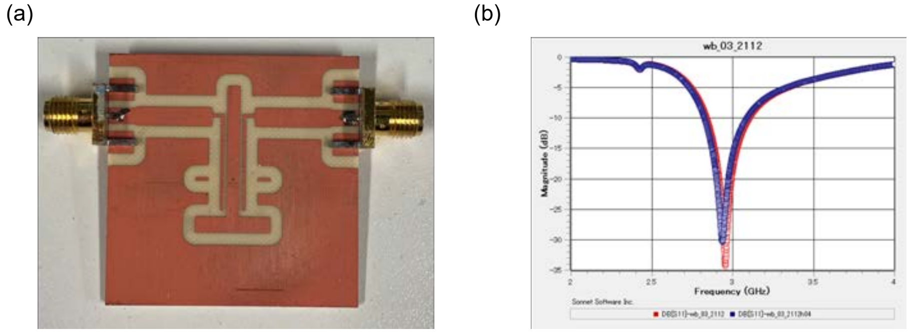

Figure 4.5: Antenna picture and S11 characteristics (a)Antenna created by a printed circuit board processor. (b)S_{11} characteristic of the antenna. Blue circle is with hole. Red circle is without hole.

the metal line, the stronger the microwave magnetic field intensity is, and the further away from the metal line, the weaker the microwave magnetic field is. In the lower figure with holes in the metal lines, the microwave magnetic field intensity distribution is suppressed in the upper part of the holes. However, because the size of the hole is small, the distribution of microwave magnetic field intensity is large. Figure 4.4(b) compares the microwave magnetic field intensity distribution when there are without holes in the metal line and when the size of the holes in the metal line is changed. In the case of without holes, the microwave magnetic field intensity changes as the distance from the metal line increases. In the case with holes, the microwave magnetic field intensity above the holes decreases, but the uniformity of the magnetic field intensity improves. In this case, a hole with a diameter of 0.8 mm was selected because it has a high degree of uniformity, although the microwave magnetic field strength is inferior.

4.1.3 Experimental results and discussion

The creation of the antennas for the parameters used in the simulation was created using a printed circuit board processor. The copper foil on the surface of the printed circuit board was cut using a drill on a printed circuit board processor to create the pattern. For comparison, an antenna without holes in the metal line and an antenna with holes in the metal line were created. Figure 4.5 shows the appearance and S_{11} characteristics of the fabricated antenna. $2.93 \sim 2.95$ GHz, which is slightly higher than the result of 2.92 GHz simulated by Sonnet, but the bandwidth where S_{11} is less than -10 dB is more than 200 MHz.

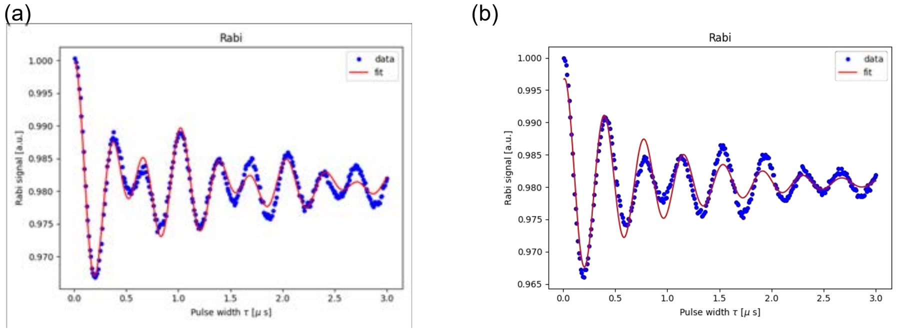

Figure 4.6: Rabi measurement results (a) Rabi oscillation at the frequency of $m_s = -1$. (b) Rabi oscillation at the frequency of $m_s = +1$.

We will check if we can make a Ramsey measurement with Double Quantum using the antenna we created. The Ramsey measurement requires a $\pi/2$ pulse of microwaves. The $\pi/2$ pulse is obtained from the period of the Rabi oscillation. Therefore, we will check if the Rabi oscillation can be observed at a microwave frequency of $m_s = \pm 1$. Figure 4.6 shows the results of the Rabi oscillation measurement. Figure 4.6(a) shows Rabi oscillation at a microwave frequency of $m_s = -1$. Figure 4.6(b) shows Rabi oscillation at a microwave frequency of $m_s = +1$. If the variation of the microwave field strength in the photoexcited region is large, the Rabi oscillations decay quickly and the waveform is not visible. On the other hand, in this antenna, the Rabi oscillations do not decay immediately. This is thought to be due to the fact that drilling holes in the metal line improves the uniformity of the microwave magnetic field strength over the holes.

The microwave amplifiers used for Ramsey measurements can accelerate the Rabi frequency up to about 4 MHz, but since the width of the ^{14}N hyperfine splitting is about 2.2 MHz, a Rabi frequency of about 5 MHz is ideal for all the hyperfine splitting to drive. To accelerate the Rabi frequency without modifying the antenna, the bias field should be reduced and the microwave frequency at $m_s = \pm 1$ should be brought closer to the resonant frequency of the antenna. The Rabi frequency may also be accelerated by changing the pattern of the antenna wiring. The reason for making the microwave field intensity uniform in the vertical direction by drilling holes in the metal line of the antenna was that the excitation laser was supposed to be incident on the diamond at Brewster's angle. In this case, the uniformity of the microwave field in the vertical direction is important. On the other hand, when the excitation laser is injected from the side of the diamond, the height of the excited area is constant. Therefore, if the spot diameter of the excitation laser is small, microwave field uniformity in the vertical direction is not so much of an issue. This method also has the advantage that fluorescence from the NV center can be focused with high collection efficiency by combining it with a CPC lens. Thus, the required characteristics of the antenna also vary depending on the method of optical excitation. Therefore, it is necessary to design the optimum antenna for the measurement system.

4.2 Lock-in Double Quantum Ramsey

In this section, we report on a measurement system that enables Ramsey measurements using Double Quantum. In this system, electrical noise is reduced by combining lock-in detection. In addition, a laser noise cancellation system is realized by combining an auto-balanced transimpedance amplifier circuit to reduce noise due to fluctuations in the output power of the laser used for optical excitation of the diamond.

4.2.1 Introduction

The highest sensitivity of magnetic field sensors using NV centers is only $15\,\mathrm{pT}/\sqrt{\mathrm{Hz}}$ [20]. Therefore, a higher sensitivity is needed to detect the magnetic field of a living body. The Ramsey method [76], one of the measurement protocols that allows NV centers to operate as magnetic field sensors, is based on the temporal separation of optical excitation and microwave manipulation, which allows the use of high optical excitation intensities while maintaining contrast. On the other hand, pulse measurement like the Ramsey method has the following problems.

1. the shot noise sensitivity is not reached due to noise caused by laser power fluctuation.
2. Pulse measurement is affected by broadband electrical noise due to high-speed sampling of the optical response of the NV center.
3. Pulsed measurement involves pulsed optical excitation, so the diamond temperature is not stable.

Laser noise cancel

Laser noise cancellation is essential to achieve high sensitivity measurements with magnetic sensors using NV centers [20, 53]. As shown in section 3.1.13, the CW-ODMR method achieves this by using part of the excitation laser as a reference light. In the CW-ODMR method, the temperature of diamond is stable because the excitation laser is always irradiating the diamond. Therefore, the fluorescence intensity does not fluctuate over time, and this method works well. However, in pulsed measurement such as the Ramsey method, the temperature of diamond fluctuates because the excitation laser is emitted in pulses. Therefore, the fluorescence fluctuates with time. Therefore, we have developed a transimpedance amplifier that automatically balances the PD current between the fluorescence and the reference light to achieve laser noise cancellation [77]. The output of this circuit is zero as long as the PD current is balanced, and only the change in fluorescence dependent on the spin state of the NV center is output, which is the AC signal.

Electrical noise reduction

Pulse measurement requires fast sampling of the temporal response of fluorescence. Therefore, broadband electrical noise is picked up. Lock-in detection synchronized with pulsed excitation laser is used to reduce electrical noise. Since the bandwidth can be changed by changing the time constant in lock-in detection, electrical noise can be suppressed by focusing on the bandwidth necessary for the measurement.

Diamond Heat Dissipation

The Ramsey method irradiates a high-power laser with a narrow beam diameter, which raises the temperature of diamond. Therefore, it is necessary to dissipate the heat from the diamond. In this case, an antenna with a SiC substrate is used to dissipate the heat of the diamond created in section 4.1. The diamond and SiC are fixed using a heat-dissipating adhesive.

In pulse measurement using a Digitizer with a fast sampling rate, the fluorescence intensity changes only a few percent in accordance with the spin state, so the majority of the fluorescence intensity is offset. This means that most of the Digitizer's resolution is consumed by the offset, reducing the resolution used to detect the spin state. Lock-in detection, on the other hand, detects only the AC signal, so the offset can be ignored. In addition, the auto-balanced transimpedance circuit outputs the spin state as an AC signal, so when combined with Lock-in detection, the resolution of the Lock-in amplifier can be used at full scale. The measurement using the Digitizer requires post-process analysis of a large amount of acquired data. On the other hand, lock-in detection has the advantage of real-time detection

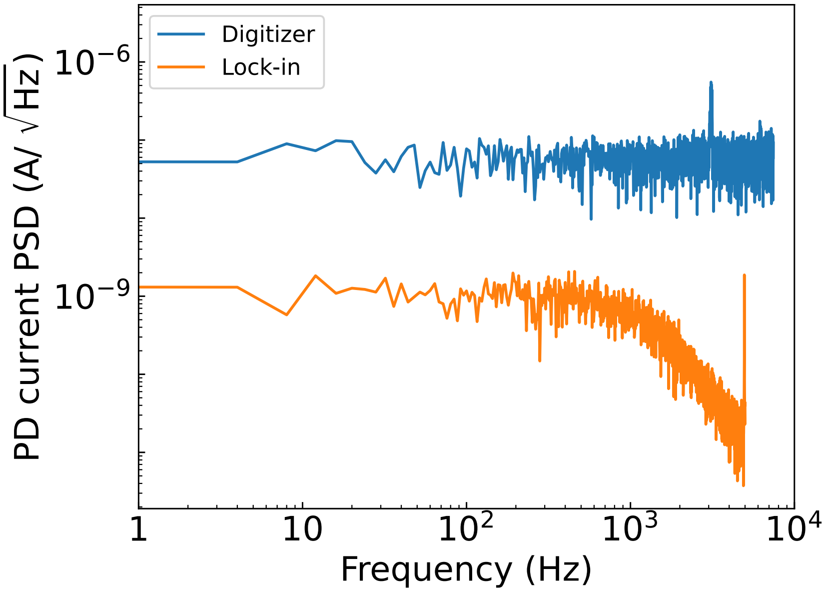

Figure 4.7: Current noise spectral density. Blue line is the measurement result using Digitizer. Orange line is the measurement result using Lock-in detection.

because the demodulated data indicates the spin state.

Figure 4.7 shows the results of comparing the current noise spectral density using Digitizer and Lock-in detection.

As will be discussed later, the Digitizer measurement maximizes the signal contrast because it extracts only the time in the readout initialization pulse when the spin state is reflected in the readout initialization pulse. On the other hand, the Lock-in detection has a lower signal contrast than the Digitizer measurement because the contrast is based on the signal intensity of the spin state in the entire readout initialization pulse. The signal contrast ratio between the Digitizer measurement and Lock-in detection is affected by the initialization time, and approaches 1:1 when the initialization time is shortened.

Figure 4.8 shows the prospect of sensitivity enhancement by the Ramsey method. The Ramsey method is expected to improve sensitivity by applying Double Quantum. Furthermore, unlike the CW-ODMR method, the intensity of the excitation power can be increased, and sensitivity below $1\,\mathrm{pT}/\sqrt{\mathrm{Hz}}$ can be achieved by combining a highly efficient focusing system such as a CPC lens.

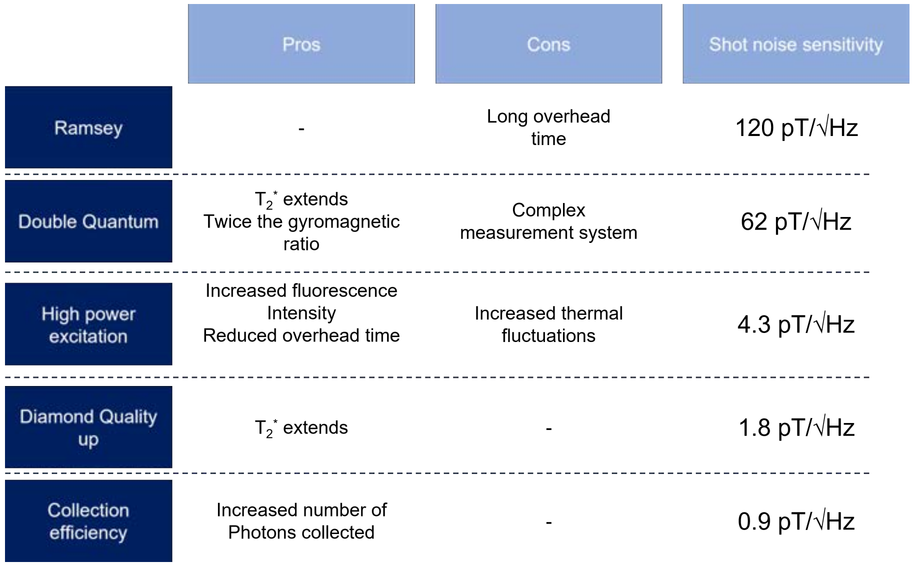

	Pros	Cons	Shot noise sensitivity
Ramsey	-	Long overhead time	120 pT/√Hz
Double Quantum	T_2^* extends Twice the gyromagnetic ratio	Complex measurement system	62 pT/√Hz
High power excitation	Increased fluorescence Intensity Reduced overhead time	Increased thermal fluctuations	4.3 pT/√Hz
Diamond Quality up	T_2^* extends	-	1.8 pT/√Hz
Collection efficiency	Increased number of Photons collected	-	0.9 pT/√Hz

Figure 4.8: Sensitivity improvement strategies for the Ramsey method and their effects.

In this study, we first constructed a Ramsey measurement system that can apply Double Quantum, which performs Digitizer and Lock-in detection. First, we confirmed that we could achieve the measurements necessary for magnetic field sensitivity measurements using Digitizer detection. After that, we applied Lock-in detection and measured the magnetic field sensitivity.

4.2.2 Experimental setup

NV diamond sample

The NV diamond crystal used in this study was prepared by the following procedure. A single-crystal of diamond was synthesised by a temperature-gradient method under high-pressure and high-temperature (HPHT) using a modified belt-type high-pressure apparatus. ^{12}C is enriched to suppress dephasing by ^{13}C nuclear spins. ^{13}C is 50 ppm. After HPHT diamond synthesis, the grown crystals were cut parallel to the $\{111\}$ crystal planes. Then, electron beam irradiation was conducted at room temperature with a 2.0 MeV with a total fluence of 1×10^{17} electrons cm^{-2}, followed by post-annealing at 1000 ℃ for 2 h under a vacuum. The concentrations of the P1 centres and NV$^-$ centres in this NV diamond sample were measured by

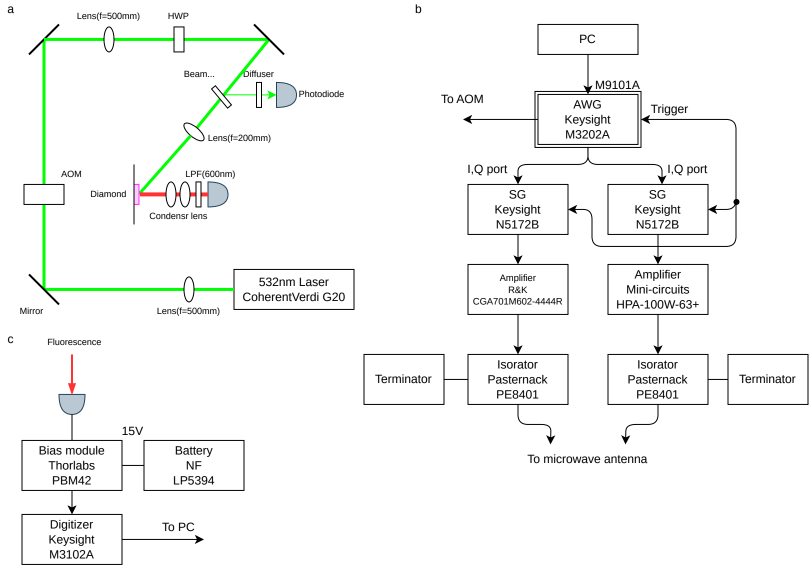

Figure 4.9: Digitizer Detection Ramsey Measurement Setup. (a) Optical system for optical excitation of diamond and detection of fluorescence (b) Microwave system for spin manipulation (c) Detection system to read out the spin state from the fluorescence

Instantaneous Diffusion to be 1.1 ppm and 0.05 ppm respectively.

Optical and electrical setup

Experimental setups of Digitizer detection and Lock-in detection are shown in Figures 4.9 and 4.10. The optical system shown in Figure 4.9(a) was installed inside a custom-made 3-layer Permalloy magnetic shield box. 532 nm laser (Coherent Verdi-G20) was installed inside this shield box. The laser is focused by a lens with a focal length of $f = 500\,\mathrm{mm}$ and passes through the AOM, after which it returns to its original spot size with a focal length of $f = 500\,\mathrm{mm}$. After passing through the AOM, the laser is focused by a lens with a focal length of $f = 200\,\mathrm{mm}$ after adjusting the polarization with a waveplate. A dielectric mirror was used as the mirror to reflect the laser. The laser spot size is $1/e^2$ Gaussian width $\sim 80\,\mu\mathrm{m}$. The laser power incident on the diamond is $\sim 70\%$ of the laser power. A portion of the laser incident on the diamond is monitored by a silicon photodiode for laser power monitoring via a beam sampler. An achromat 1.25 NA Abbe condenser lens (Olympus U-AC) collected red fluorescence from the

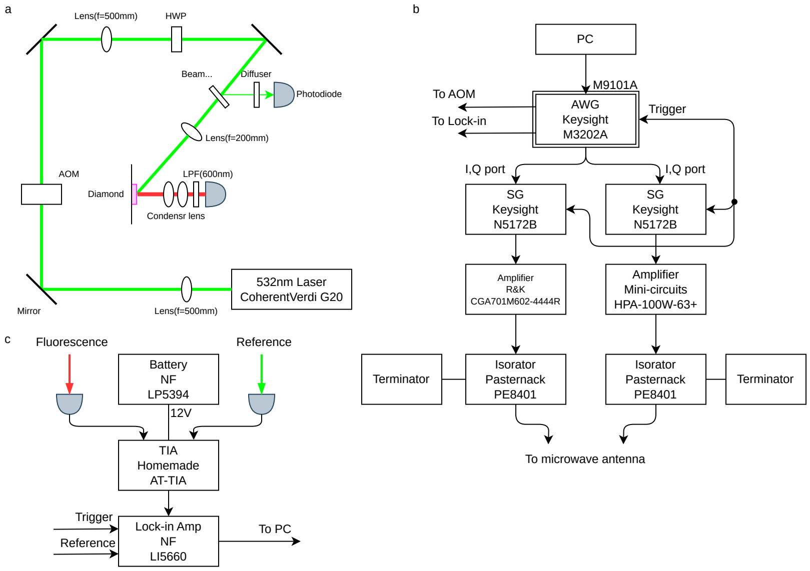

Figure 4.10: Lock-in Detection Ramsey Measurement Setup. (a) Optical system for optical excitation of diamond and detection of fluorescence (b) Microwave system for spin manipulation (c) Detection system to read out the spin state from the fluorescence

NV centres through the top surface. Fluorescence was then passed through a long-pass filter and directed onto a silicon photodiode. The condenser lens, the optical filter, and the photodiode were mounted downward on an XYZ manual translation stage. A square-shaped rare-earth magnet aligned along the [111] orientation applied a uniform static bias field of $B_0 = 2.2\,\mathrm{mT}$ at the diamond to split the $m_s = \pm 1$ ground states. The antenna used to irradiate the microwaves on the diamond was the one described in section 4.1.

The microwave system for spin manipulation is shown in Figure 4.9(b). The two microwave oscillators are IQ modulated to adjust the microwave phase. The microwaves output from the microwave oscillators are amplified by a microwave amplifier and delivered to the microwave antenna via a circulator. IQ modulation to the microwave oscillator is performed using the analog output port on the AWG board, and the on/off control of the AOM is similarly performed using the analog output port on the AWG board.

Detection system to read out the spin state from the fluorescence is shown in Figure 4.9(c). The diamond fluorescence is converted to a current by the photodiode, which is converted to a voltage by the Digitizer board terminated in 50Ω and transferred to the PC. The photodiode that detects the diamond fluorescence is applied a reverse bias voltage of $15\,\mathrm{V}$.

The difference between the Lock-in detection system in Figure 4.10 and the Digitizer detection system in Figure 4.9 is the microwave control system and the detection system. The lock-in detection system requires a reference signal. The reference signal is output from the analog port of the AWG board. The Lock-in detection system uses an auto-balanced transimpedance amplifier for laser noise cancellation. When the transimpedance amplifier is input with the diamond fluorescence signal and the laser monitor signal, it outputs a spin-state dependent signal with the laser noise removed. The output of the transimpedance amplifier input to the lock-in amplifier is then demodulated and the demodulated results are transferred to a PC.

Instrument Synchronization

The Ramsey method requires the AOM ON/OFF control and microwave control to operate in ∼nanoseconds; the Keysight AWG board and Digitizer board are integrated into the PXI chassis in the Ramsey system. The boards are synchronized in real-time by the Keysight KS2201A PathWave Test Sync Executive. The KS2201A is capable of real-time synchronization of the corresponding boards with a time interval of 10ns. On the other

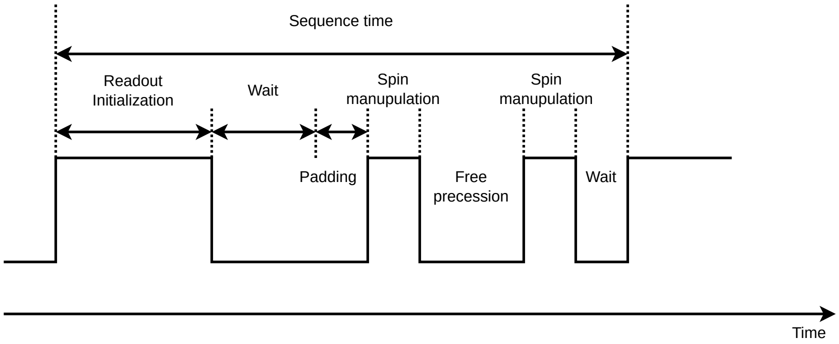

Figure 4.11: Ramsey fundamental sequence design. The length of a single sequence is determined from the sum of the following components. Read out and initialization time, post-initialization wait time, spin operation time, free precession time, spin operation time, and read wait time. Padding time is added so that the sum of these components is an integer multiple of 10ns, which is the board synchronization time constraint.

hand, signal generators and lock-in amplifiers cannot be synchronized by the KS2201A. Therefore, we decided to synchronize the signal generator and Lock-in amplifier via the trigger port on each instrument. Hardware real-time synchronization of the entire Ramsey system was realized by linking the KS2201A with the trigger port on the instrument. Control of the instruments, AWG board, Digitizer board and KS2201A was implemented using Python.

Ramsey sequence

The basic sequence involved in the Ramsey measurement is shown in Figure 4.11. Synchronization between the AWG board and the Digitizer board is performed when the AOM is turned on and fluorescence is emitted from the diamond. Since the clock frequency of the FPGA on the board is 100 MHz, the time between the AOM turning on and the next AOM turning on must be an integral multiple of 10 ns. It is not desirable to change the spin manipulation time, the free precession time, or the time before readout, as this will affect the quantum state. On the other hand, after initialization, a waiting time of a few microseconds is required for the excited electrons to fall back to the ground state. By adjusting this time, the above constraints are realized. The Padding shown in Figure 4.11 is this adjustment time.

Figures 4.12 - 4.15 show the Single Quantum Ramsey sequence for Dig-

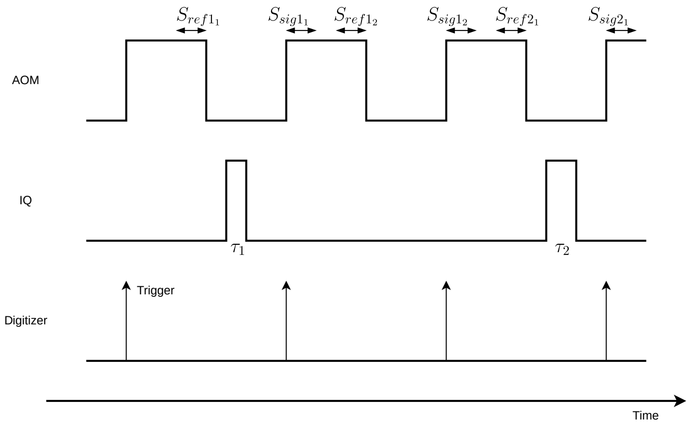

Figure 4.12: Digitizer detection Rabi sequence. The Rabi sequence sweeps the microwave application time. The microwave irradiation time is determined by the pulse input time to the IQ modulation.

itizer detection.

As shown in Figure 4.12, the Rabi sequence sweeps the microwave irradiation time. Taking the microwave sweep time on the horizontal axis and the normalized fluorescence intensity on the vertical axis, an oscillatory waveform is obtained. The reciprocal of the oscillation waveform period is the Rabi frequency, and 1/4 of a cycle time is the $\pi/2$ pulse time.

As shown in Figure 4.13, the Ramsey sequence sweeps free precession time. Taking the free precession time on the horizontal axis and the normalized fluorescence intensity on the vertical axis, a decaying oscillatory waveform is obtained. The envelope of the decaying waveform represents the dephasing time, which is the time it takes for the waveform to decay to $1/e$. The frequency of the waveform is the difference between the applied microwave frequency and the NV center resonance frequency.

As shown in Figure 4.14, the Detuning sweep sequence sweeps the microwave frequency. Taking the microwave frequency on the horizontal axis and the normalized fluorescence intensity on the vertical axis, an oscillatory waveform is obtained. The oscillation waveform represents the change in fluorescence signal in response to changes in the external magnetic field. The frequency at which the slope of the tangent line of the oscillation waveform is at its maximum is the most sensitive to changes in the external magnetic field.

As shown in Figure 4.15, in the Sensing sequence, the microwave fre-

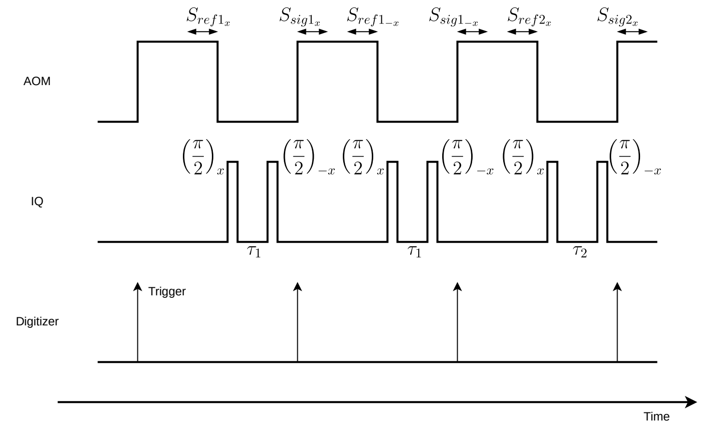

Figure 4.13: Digitizer detection Ramasey sequence. Ramsey sequence sweeps free precession time. The phase of the microwave is changed using IQ modulation to adjust the axis along which the spins are rotated.

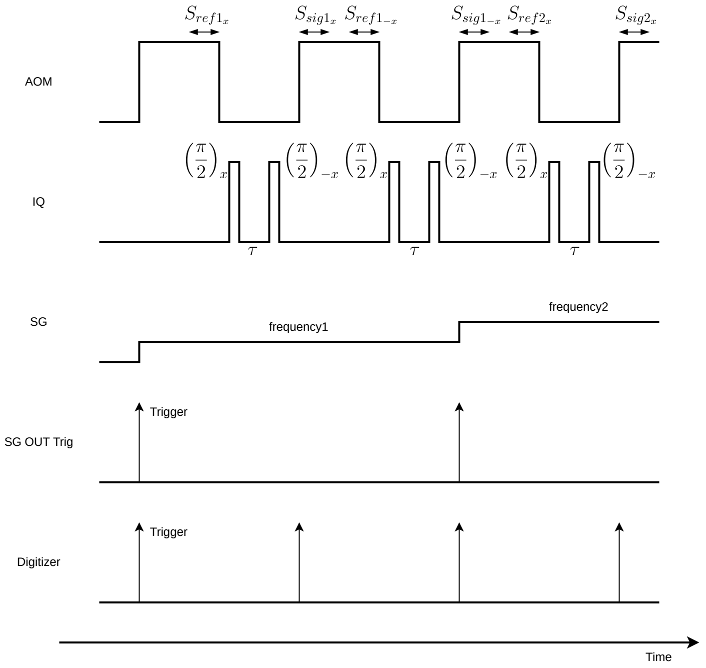

Figure 4.14: Digitizer detection Detuning sweep sequence. Detuning sweep sequences sweep the microwave frequency while keeping the free age difference time fixed. The phase of the microwave is changed using IQ modulation to adjust the axis along which the spins are rotated.

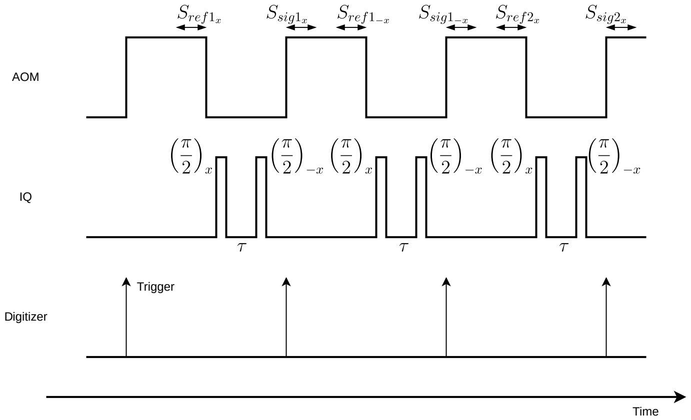

Figure 4.15: Digitizer detection Sensing sequence. In the Sensing sequence, microwave frequency and free precession time are fixed. The same sequence is repeated throughout the measurement time to measure the magnetic field. The phase of the microwave is changed using IQ modulation to adjust the axis along which the spins are rotated.

quency and free precession time are fixed and the same sequence is repeated. The above sequence is repeated for the time period for which the magnetic field is to be measured, and the fluorescence is recorded. The change in normalized fluorescence intensity for each sequence is converted to a change in frequency using the slope obtained from the Detuning sweep sequence. The frequency change can be converted to magnetic field using the gyromagnetic ratio. The value of the magnetic field can be obtained for each sequence time interval.

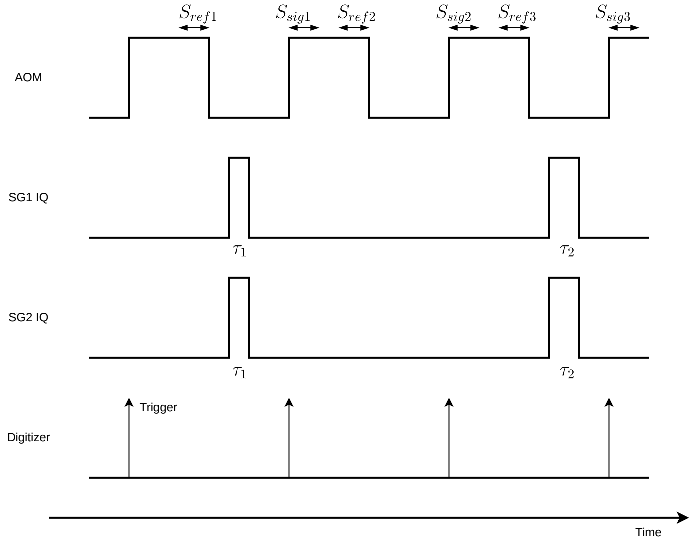

Figure 4.16: Digitizer detection Double Quantum Rabi sequence. The Rabi sequence sweeps the microwave application time. The microwave irradiation time is determined by the pulse input time to the IQ modulation.

Figures 4.16 - 4.19 show the Double Quantum Ramsey sequence for Digitizer detection. The difference between Single Quantum and Double Quantum is that Double Quantum uses both microwave frequencies of ms=±1. In order for Double Quantum Rabi to work, the Rabi frequency of Single Quantum must be the same at $m_s = \pm 1$. Therefore, align the Rabi frequencies in Single Quantum and perform Double Quantum Rabi under those conditions. The frequency sweep direction of Double Quantum Detuning sweep is opposite for $m_s = -1$ and $m_s = +1$. Otherwise, it is the same as Single Quantum.

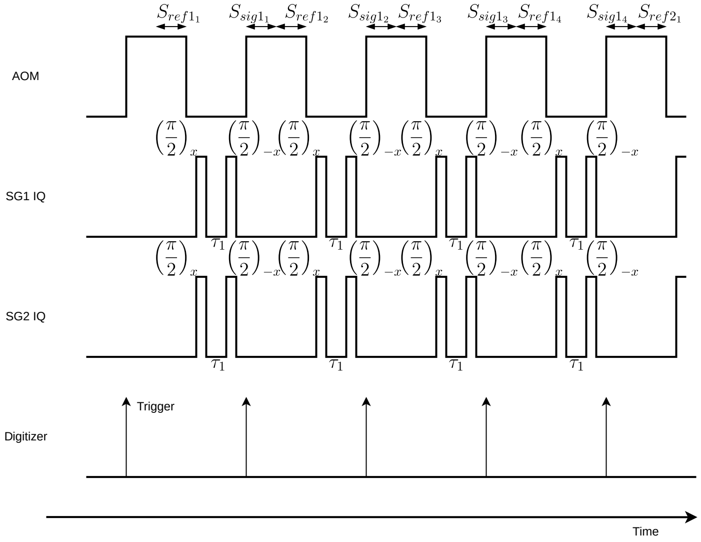

Figure 4.17: Digitizer detection Double Quantum Ramasey sequence. Ramsey sequence sweeps free precession time. The phase of the microwave is changed using IQ modulation to adjust the axis along which the spins are rotated.

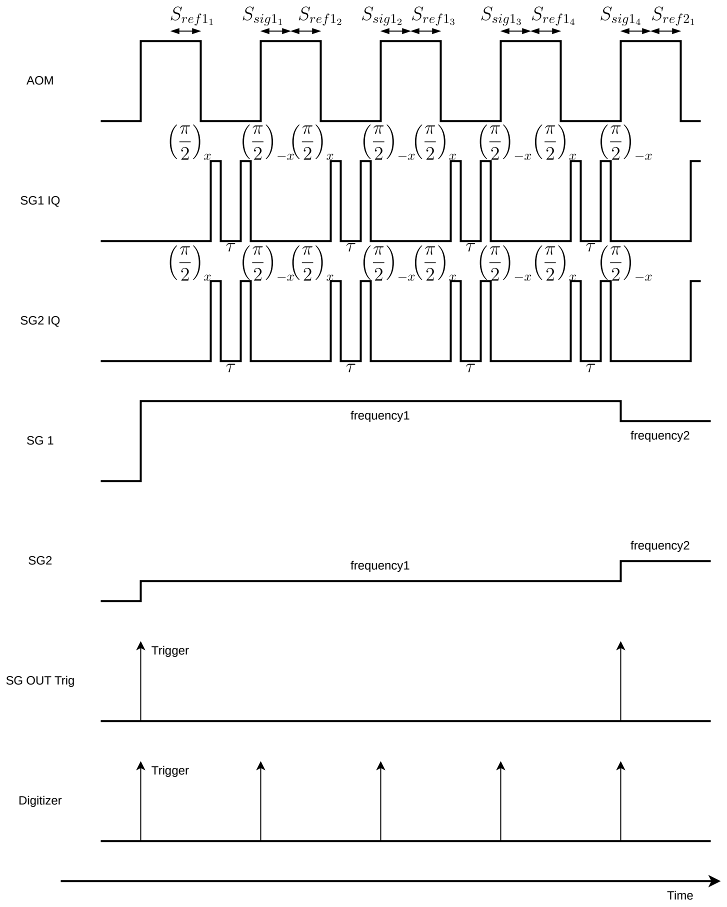

Figure 4.18: Digitizer detection Double Quantum Detuning sweep sequence. Detuning sweep sequences sweep the microwave frequency while keeping the free age difference time fixed. The phase of the microwave is changed using IQ modulation to adjust the axis along which the spins are rotated.

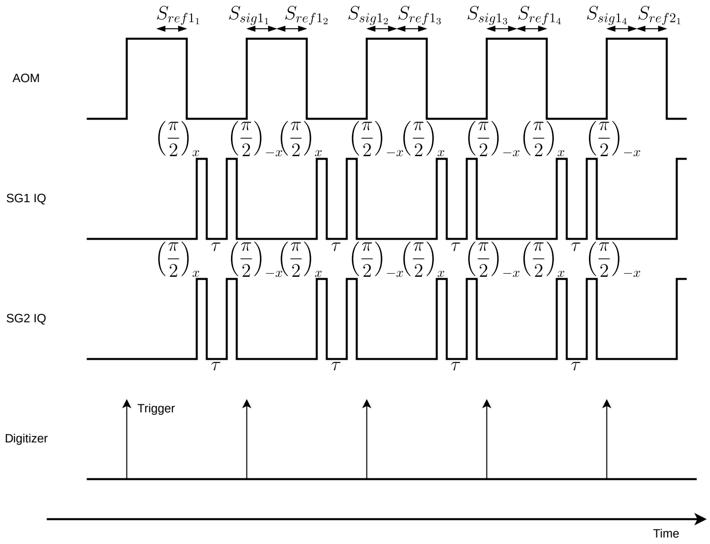

Figure 4.19: Digitizer detection Double Quantum Sensing sequence. In the Sensing sequence, microwave frequency and free precession time are fixed. The same sequence is repeated throughout the measurement time to measure the magnetic field. The phase of the microwave is changed using IQ modulation to adjust the axis along which the spins are rotated.

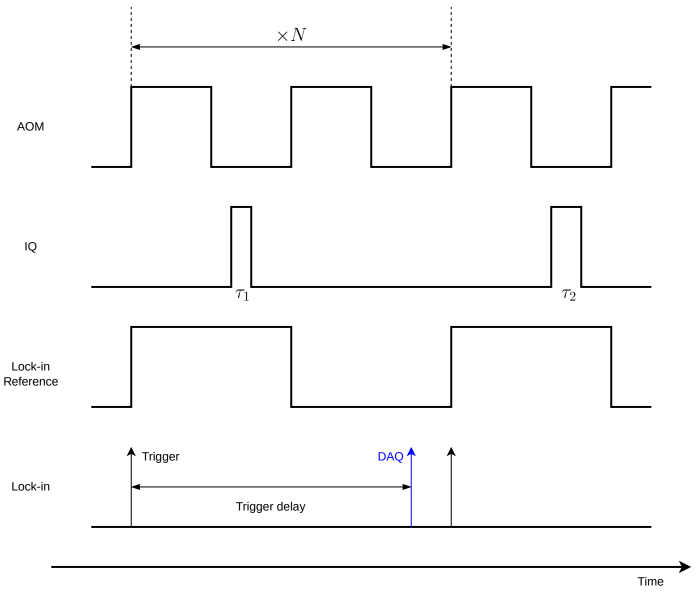

Figure 4.20: Lock-in detection Rabi sequence. The Rabi sequence sweeps the microwave application time. The microwave irradiation time is determined by the pulse input time to the IQ modulation.

Figures 4.20 - 4.23 show the Single Quantum Ramsey sequence with Lock-in detection applied, and Figures 4.24 - 4.27 show the Double Quantum Ramsey sequence with Lock-in detection applied.

The difference between Lock-in detection and Digitizer detection is that the same sequence is repeated for one sweep parameter; in Lock-in detection, the same sequence must be repeated until the transient response converges because of the response delay caused by the low-pass filter after phase sensitive detector. Since the time for the transient response to converge depends on the setting of the lock-in amplifier, it is programmed to change automatically according to the setting value. The trigger signal is input to the Lock-in amplifier immediately after the start of the sequence of each sweep parameter. The trigger delay is set to the time when the transient response of the Lock-in amplifier converges. Since the same sequence is repeated in the Sensing sequence, data is collected at time intervals set by the timer in the Lock-in amplifier. In this case, the frequency bandwidth of the Lock-in detection is equal to the equivalent noise bandwidth determined by the time constant of the Lock-in amplifier and the order of the low-pass filter.

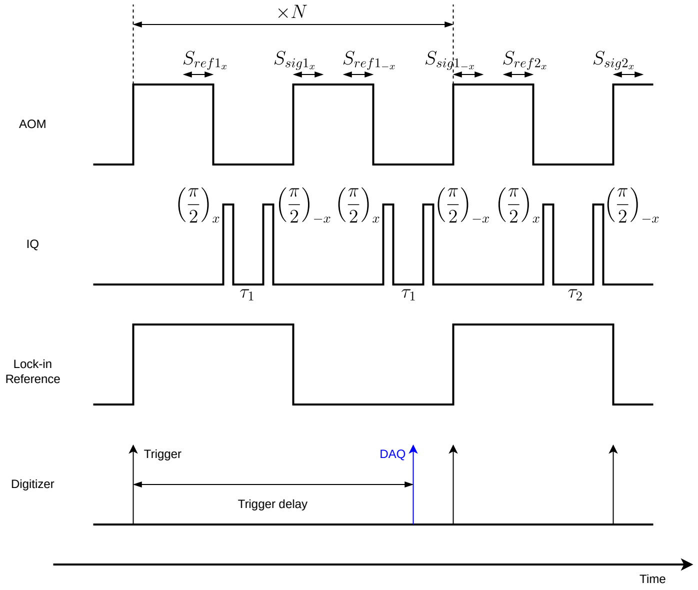

Figure 4.21: Lock-in detection Ramasey sequence. Ramsey sequence sweeps free precession time. The phase of the microwave is changed using IQ modulation to adjust the axis along which the spins are rotated.

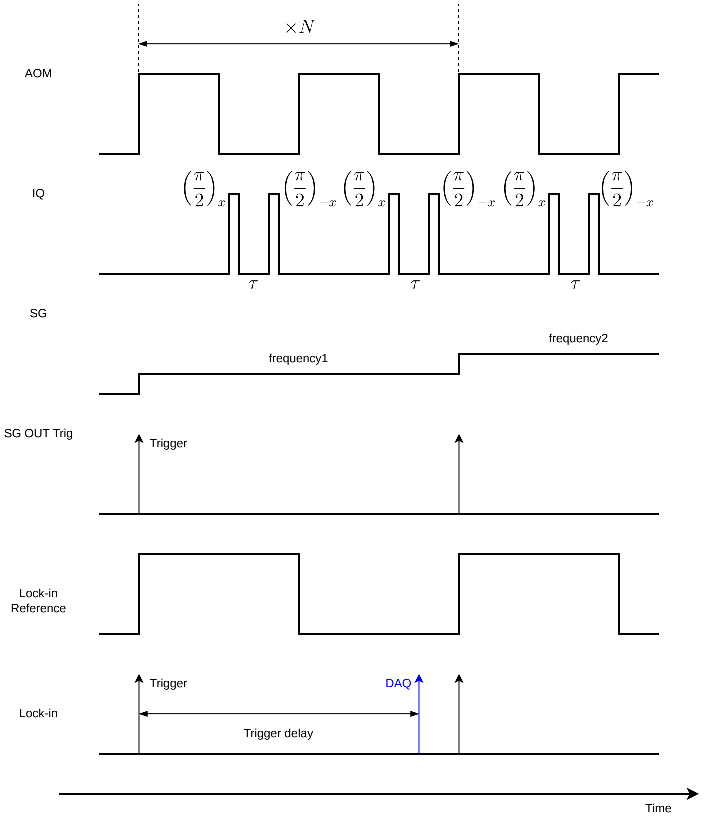

Figure 4.22: Lock-in detection Detuning sweep sequence. Detuning sweep sequences sweep the microwave frequency while keeping the free age difference time fixed. The phase of the microwave is changed using IQ modulation to adjust the axis along which the spins are rotated.

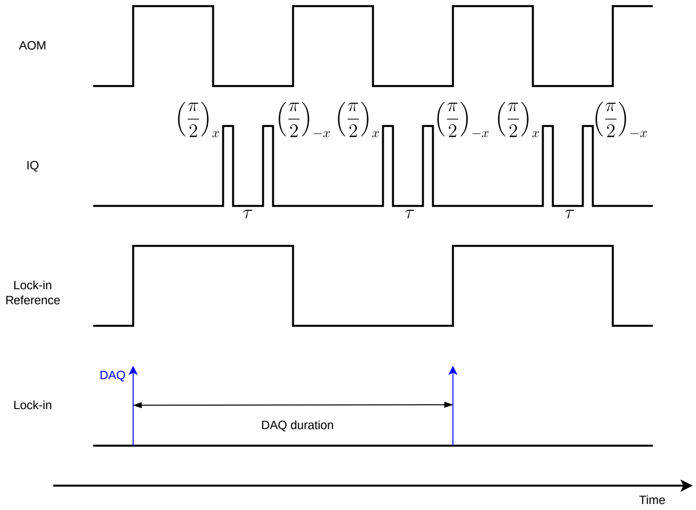

Figure 4.23: Lock-in detection Sensing sequence. In the Sensing sequence, microwave frequency and free precession time are fixed. The same sequence is repeated throughout the measurement time to measure the magnetic field. The phase of the microwave is changed using IQ modulation to adjust the axis along which the spins are rotated.

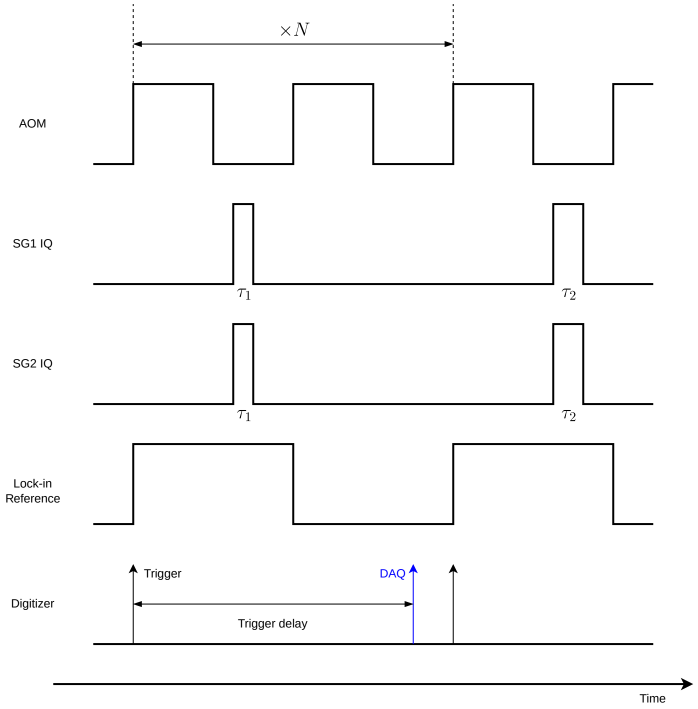

Figure 4.24: Lock-in detection Double Quantum Rabi sequence. The Rabi sequence sweeps the microwave application time. The microwave irradiation time is determined by the pulse input time to the IQ modulation.

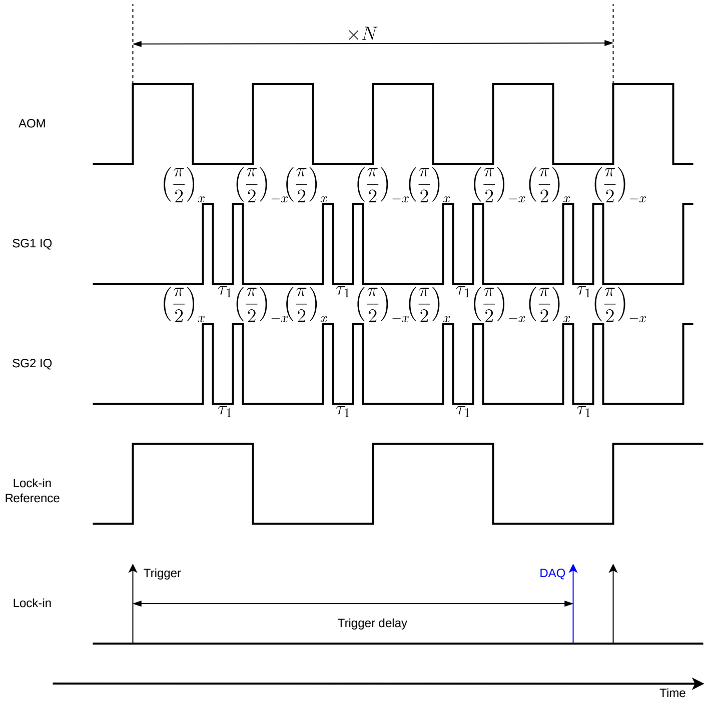

Figure 4.25: Lock-in detection Double Quantum Ramasey sequence. Ramsey sequence sweeps free precession time. The phase of the microwave is changed using IQ modulation to adjust the axis along which the spins are rotated.

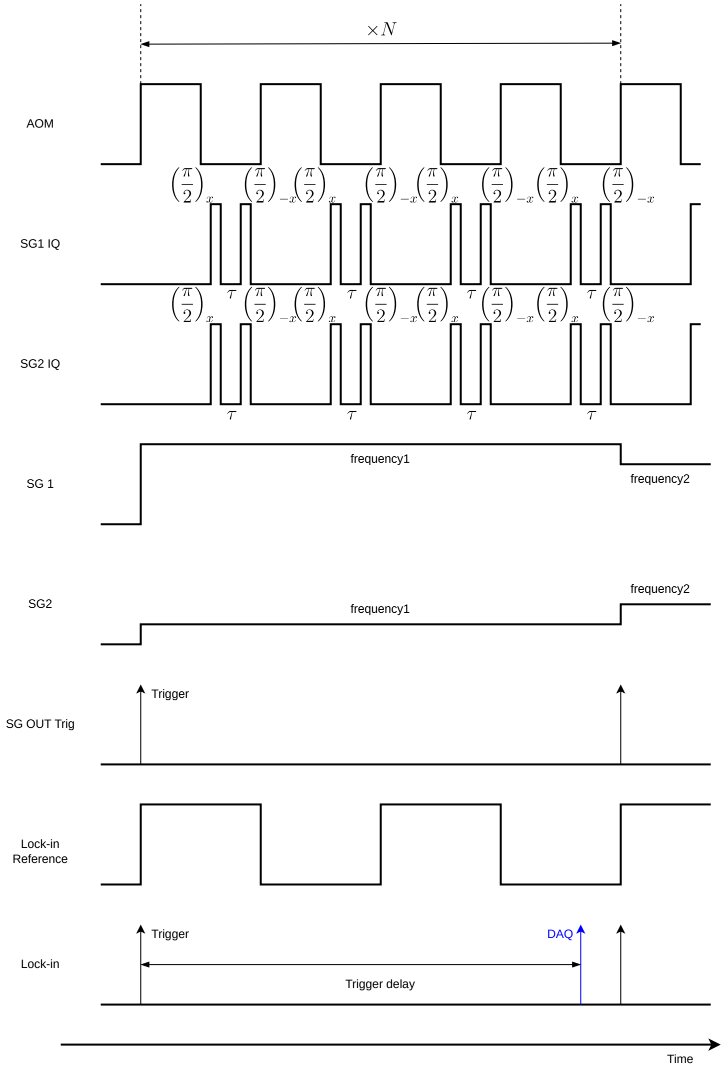

Figure 4.26: Lock-in detection Double Quantum Detuning sweep sequence. Detuning sweep sequences sweep the microwave frequency while keeping the free age difference time fixed. The phase of the microwave is changed using IQ modulation to adjust the axis along which the spins are rotated.

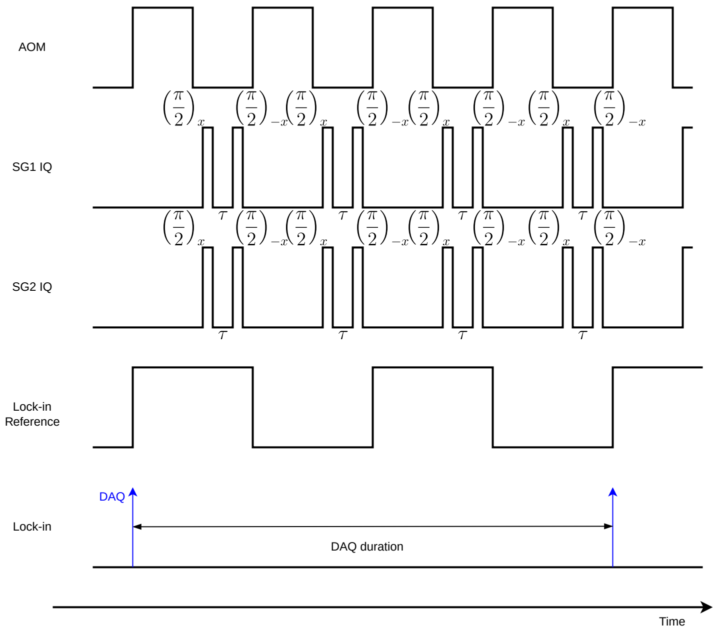

Figure 4.27: Lock-in detection Double Quantum Sensing sequence. In the Sensing sequence, microwave frequency and free precession time are fixed. The same sequence is repeated throughout the measurement time to measure the magnetic field. The phase of the microwave is changed using IQ modulation to adjust the axis along which the spins are rotated.

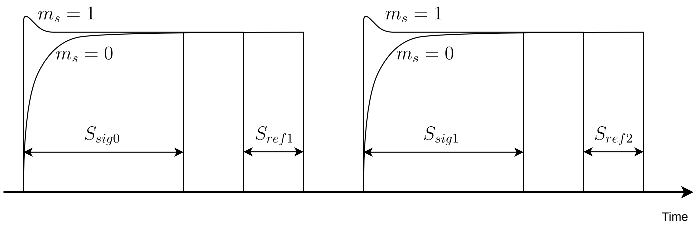

Figure 4.28: Digitizer detection signal analysis. The time that AOM is ON serves as spin state readout and initialization. The spin state is determined by the ratio of the value obtained by integrating a fixed time from the beginning of the time that AOM is ON to the value obtained by integrating a fixed time from the end of the time that spin initialization is complete.

Signal Analysis

Here we show how to detect spin states in Digitizer detection. Figure 4.28 shows the procedure for data detected by Digitizer. Let S_{sig} be the value obtained by integrating a certain time from the beginning of the time when AOM is turned on among the data recorded by Digitizer; let S_{ref} be the value obtained by integrating the time from the time when spin initialization is completed to the time when AOM is turned off among the data recorded by Digitizer. The spin state is obtained by S_{sig}/S_{ref}. At the start of the sequence, the data recorded by the Digitizer when the first AOM is turned on is only meaningful for S_{ref}, so S_{ref} and S_{sig} will shift the sequence by one. By performing this procedure for each sequence, the Rabi and Ramsey data described earlier can be obtained.

Sensing parameter determination

Figure 4.29 shows the parameter determination method performed before the sensitivity measurement. The parameters required for sensing are determined as follows. Determine the resonance frequency by using the CW-ODMR method as shown in Figure 4.29(a). Measure Rabi at the resonance frequency as shown in Figure 4.29(b), and determine the $\pi/2$ pulse from the Rabi frequency. As shown in Figure 4.29(c), Ramsey is measured using the parameters determined in (a) and (b), and T_2^* and the free precession time at sensing are determined. As shown in Figure (d), Ramsey is measured while sweeping the microwave frequency with the parameters determined in (b) and (c) to determine the microwave frequency and slope to be used for

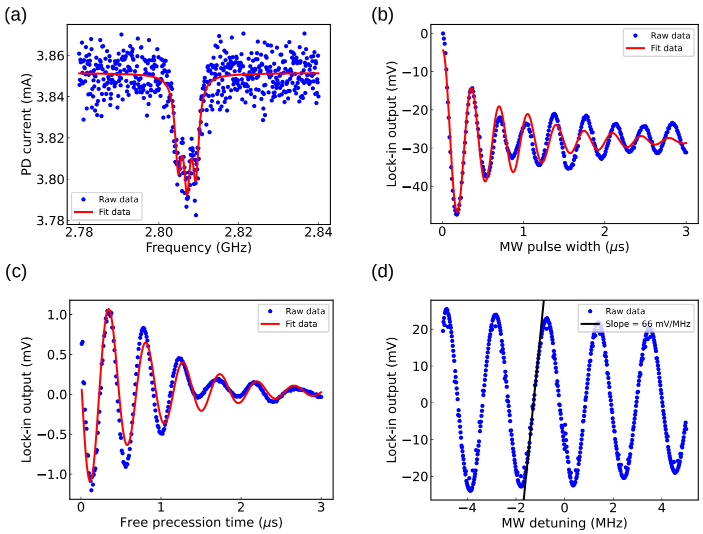

Figure 4.29: Method of sensing paramter determination. (a)CW-ODMR method: determination of resonance frequency. (b)Rabi measurement: Determination of $\pi/2$ pulse. (c)Ramsey measurement: Determination of T_2^* and free age difference time. (d)Detuning sweep: Determination of sensing frequency and slope.

sensing. During sensing, Ramsey measurements are made using these parameters for the measurement time. The results are converted to a magnetic field using the slope, and the system can operate as a magnetic sensor.

4.2.3 Result and discussion

Figure 4.30 shows the results of sensing using the parameters determined in the procedure described in section 4.2.2 Sensing parameter determination. Laser power was measured at 1W. Figure 4.30(a) shows the Lock-in Single Quantum Ramsey sensing results. It can be seen that the fluctuation below 10 Hz is large. This is due to the fact that the temperature fluctuation of the diamond at the beginning of the sequence is seen as a magnetic field fluctuation, since Single Quantum cannot distinguish between magnetic field fluctuation and temperature fluctuation. This means that Single Quantum is not robust against temperature fluctuations of diamond due to changes in environmental temperature or fluctuations in laser power. Figure 4.30(b) shows the Lock-in Double Quantum Ramsey sensing result, which shows that the fluctuations below 10 Hz that were visible with Single Quantum Ramsey sensing have disappeared. This is because Double Quantum uses

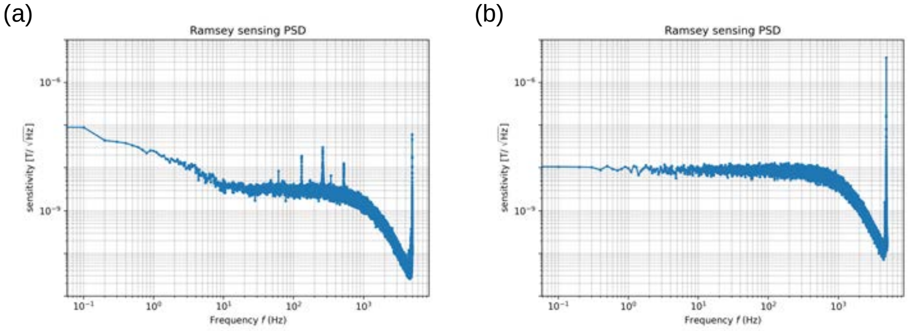

Figure 4.30: Lock-in sensing result. (a) Lock-in Single Quantum Ramsey sensing results. (b) Lock-in Double Quantum Ramsey sensing result.

both $m_s = \pm 1$, which cancels out changes in resonance frequencies that shift in the same direction, such as temperature and strain. This means that Double Quantum is robust to temperature fluctuations in diamond due to changes in ambient temperature or fluctuations in laser power.

As can be seen from the results in Figure 4.30, the sensitivity is not as high as expected. Furthermore, the sensitivity of Double Quantum is $10\,\mathrm{nT}/\sqrt{\mathrm{Hz}}$, which is worse than Single Quantum's sensitivity of $3\,\mathrm{nT}/\sqrt{\mathrm{Hz}}$. There are two possible causes.

1. The residual Single Quantum component in Double Quantum is large and the Double Quantum signal is weak.

2. Weak Lock-in signal due to long initialization time.

Figure 4.31 shows the Double Quantum and Single Quantum contributions in the Double Quantum Ramsey. Figure 4.31(a) shows the results of combining the addition and subtraction of signals $S_1 \sim S_4$ of the four sequences of Double Quantum Ramsey shown in Figure 4.17 to emphasize Double Quantum and Single Quantum or cancel the signals. It can be seen that the Double Quantum enhancement in the blue line oscillates faster than the Single Quantum enhancement in the orange line. Figure 4.31(b) is the FFT result of the emphasis waveform in (a). It can be seen that the Double Quantum enhancement (blue line) oscillates twice as fast as the Single Quantum enhancement (orange line). Comparing the magnitudes of the spectra, Double Quantum and Single Quantum are about the same. Therefore, the residual Single Quantum in the Double Quantum-enhanced line reduces the slope, which is thought to deteriorate the sensitivity. To solve

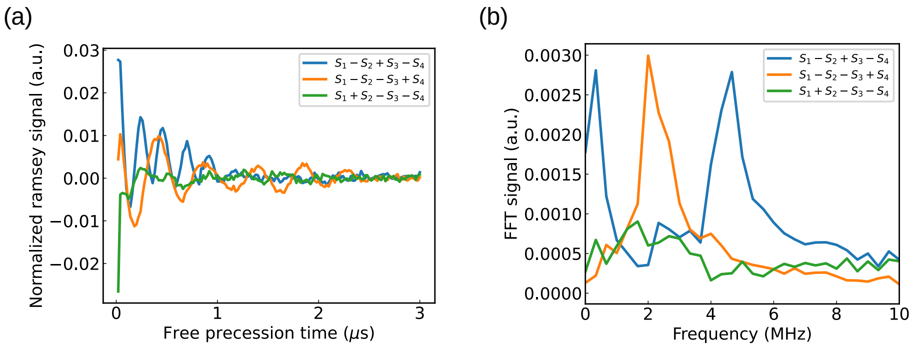

Figure 4.31: Double Quantum Ramsey included in Residual Single Quantum Ramsey. (a) Single Quantum component in Double Quantum Ramsey. The blue line is Double Quantum enhancement. The orange line is Single Quantum enhancement. The green line shows pre-signal cancellation. (b) FFT results for each enhancement component.

this problem, the tuning method using Tomograpy proposed by Hart should be implemented to reduce the residual Single Quantum component.

We determined the initialization time as follows. First, we recorded the transient response of the fluorescence for the spin states $m_s = 0$ and $m_s = 1$. The difference between the transient responses was fitted with an exponential-decaying curve. The difference signal is shown in Figure 4.32. The time at which the difference signal decays to $1/e$ was defined as the initialization time constant, and the initialization time was twice the initialization time constant.

To ensure the effect of laser power density on the initialization time, the initialization time was measured for different laser powers and focal lengths of the lens that focuses the excitation light. The results are shown in Figure 4.33. The laser power was set in the range 1-5 W and the focal lengths were used at f=200 mm and f=50 mm. Regardless of the focal length, the initialization time became shorter as the laser power was increased. For the same laser power, the shorter the focal length, the shorter the initialization time. However, the shortest initialization time was 16 us, which is 4-5 times slower than the excitation power density in previous studies [76].

In a similar Ramsey measurement [76], the initialization time was 3 us at 1 W laser power. Based on our results, we estimate that a laser power of about 14W is required. One possible reason for this is that the beam shape is Gaussian. The saturation pumping rate for NV center initialization is 66 MHz, which is very high, and the pumping rate in the ensemble is

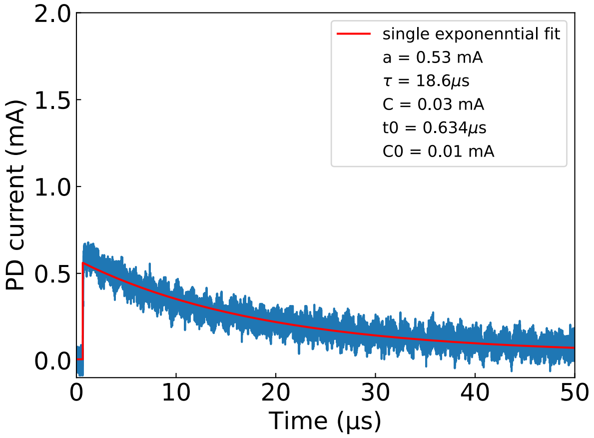

Figure 4.32: Initialization time constant definition. Spin state-dependent fluorescence remains the same over time. Where the difference signal reaches zero, the spin state is fully initialised to $m_s = 0$.

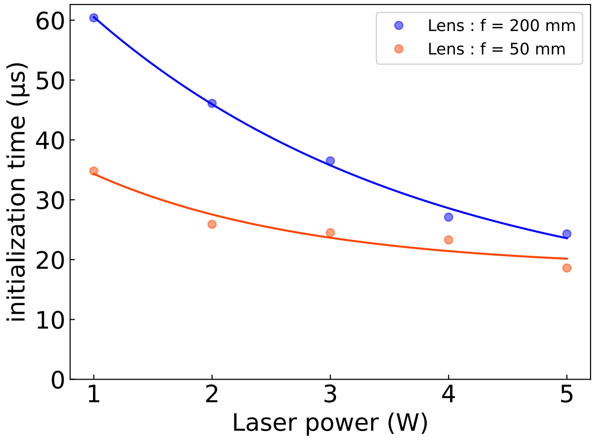

Figure 4.33: Initialization time dependence on laser power and focal length. The higher the laser power and the shorter the focal length of the focusing lens, the shorter the initialization time, but the initialization time can only be reduced to 16 us at the shortest.

proportional to the laser intensity. Therefore, in Gaussian, the excitation rate depends on the distance from the beam center. The peripheral area with low laser intensity is large in terms of area, so its effect is seen in the entire ensemble. It has been reported that the intra-beam variation in initialization time can be as much as 10 times or more depending on the Gaussian shape, and the use of a top-hat shaped beam has been proposed as a solution to this problem. The initialization time could not be less than 10 us even when the laser intensity was increased to 16 times of the current intensity with a short focal length lens. This indicates that the beam shape is likely to be the cause of the inability to shorten the initialization time. Therefore, we decided to use a beam with a top-hat shape by using a beam shaper.

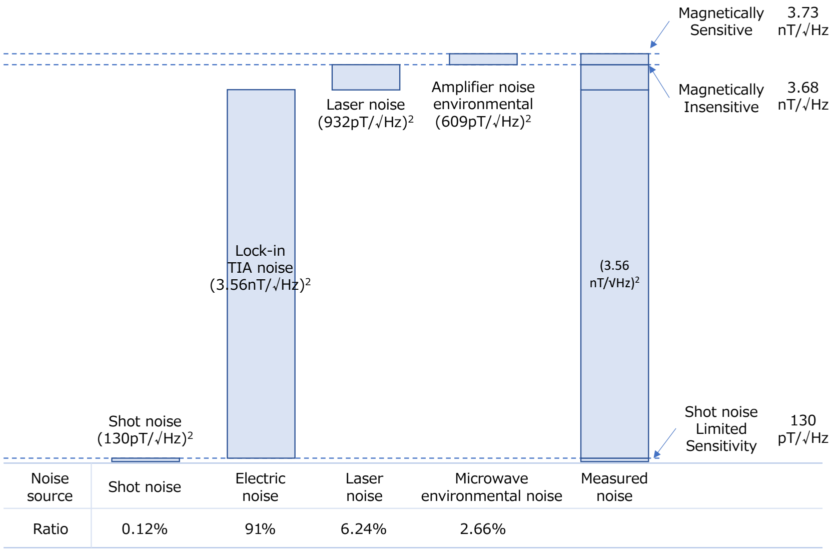

Noise source	Shot noise	Electric noise	Laser noise	Microwave environmental noise	Measured noise
Ratio	0.12%	91%	6.24%	2.66%	

Figure 4.34: Gap between measured sensitivity and shot noise sensitivity is back-calculated from measured sensitivity, sensitivity with microwave off, and sensitivity with microwave and laser off.

The gap between the measured sensitivity and the shot noise sensitivity was analyzed. The conditions under which the measured sensitivity was obtained were as follows. Laser output power 1 W, fluorescence current 5.62 mA, reference current 3.93 mA, initialization time 30 us, $\pi/2$ pulse 71 ns, and free precession time 460 ns. The slope was 4.88 mV/MHz. The shot noise sensitivity under these conditions is $130\,\mathrm{pT}/\sqrt{\mathrm{Hz}}$. The measured sensitivity was $3.73\,\mathrm{nT}/\sqrt{\mathrm{Hz}}$, $3.68\,\mathrm{nT}/\sqrt{\mathrm{Hz}}$ without microwaves applied, and $3.56\,\mathrm{nT}/\sqrt{\mathrm{Hz}}$ with the laser turned off. The magnitude of noise from each noise source was estimated from these measurements in Figure 4.34. The largest noise source is electrical noise. Later measurements revealed that the main source of electrical noise was the lock-in amplifier. Since the magnitude of this noise is large compared to the input equivalent noise voltage density of the lock-in amplifier, it is strongly suspected that noise is being transmitted to the lock-in amplifier. The unbalanced laser intensity noise was also found to have an effect. This can be reduced by adjusting the time constant of the auto-balanced transimpedance amplifier.

The extent to which the gap between shot noise and measured sensitivity can be reduced was investigated. It was assumed that electrical noise, the main noise source, could be reduced to twice the square root of the sum of the squares of the input equivalent noise voltage density of the lock-

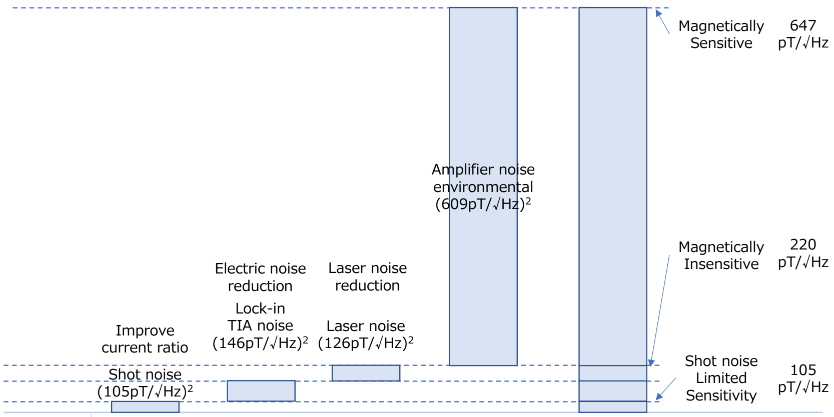

Noise source	Shot noise	Electric noise	Laser noise	Microwave environmental noise	Measured noise
Ratio	2.65%	5.1%	3.81%	88.4%	

Figure 4.35: Result of noise reduction for each noise source and building them up. Measured sensitivity improved by a factor of 6 compared to shot noise.

in amplifier and the noise voltage density of the transimpedance amplifier. Laser intensity noise was also assumed to be reduced to 1.2 times the shot noise. Amplifier noise was left unchanged as the effectiveness of the countermeasure was unknown. The measured sensitivity of the noise reduction measures is shown in Figure 4.35, which was calculated by adding up the noise. These results show that the measured sensitivity can be improved to about six times the shot noise sensitivity.

From these results, the parameters required to achieve a measured sensitivity of $1\,\mathrm{pT}/\sqrt{\mathrm{Hz}}$ were re-estimated. The results are shown in Figure 4.36. To achieve a measured sensitivity of $1\,\mathrm{pT}/\mathrm{h}\sqrt{\mathrm{Hz}}$, a T_2^* of 28 us is required. This value is above the limit determined from the P1 and ^{13}C concentrations in the material. This value can be achieved by combining a new quantum protocol called P1 decoupling.

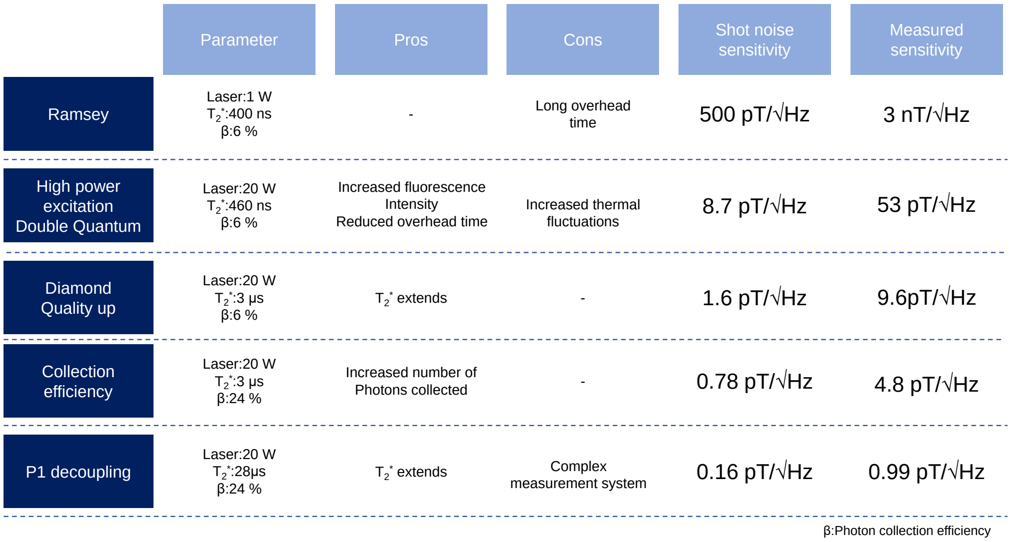

	Parameter	Pros	Cons	Shot noise sensitivity	Measured sensitivity
Ramsey	Laser:1 W T_2^*:400 ns β:6 %	-	Long overhead time	500 pT/√Hz	3 nT/√Hz
High power excitation Double Quantum	Laser:20 W T_2^*:460 ns β:6 %	Increased fluorescence Intensity Reduced overhead time	Increased thermal fluctuations	8.7 pT/√Hz	53 pT/√Hz
Diamond Quality up	Laser:20 W T_2^*:3 μs β:6 %	T_2^* extends	-	1.6 pT/√Hz	9.6pT/√Hz
Collection efficiency	Laser:20 W T_2^*:3 μs β:24 %	Increased number of Photons collected	-	0.78 pT/√Hz	4.8 pT/√Hz
P1 decoupling	Laser:20 W T_2^*:28μs β:24 %	T_2^* extends	Complex measurement system	0.16 pT/√Hz	0.99 pT/√Hz

β:Photon collection efficiency

Figure 4.36: Result of noise reduction for each noise source and building them up. Measured sensitivity improved by a factor of 6 compared to shot noise.

4.3 Conclusion

In this chapter, an antenna for Double Quantum is developed and a measurement system combining the Ramsey method with Double Quantum and Lock-in detection is constructed. With a view to biomagnetic field measurement, we have proposed an antenna that can generate a uniform and strong magnetic field in a wide bandwidth for Double Quantum, where $\{111\}$ diamond, which is advantageous for biomagnetic field measurement, is available, and Double Quantum operation is actually confirmed. Although the microwave field strength and uniformity are inferior to those of three-dimensional loop-gap resonators and dielectric resonators, the antenna achieves both strong optical excitation and highly efficient light focusing and a wide bandwidth. In addition, the microwave magnetic field is generated parallel to the antenna, so $\{111\}$ diamond can be used, which is advantageous for biomagnetic field measurements. This makes it suitable for biomagnetic field measurements using the Ramsey method with Double Quantum. Furthermore, the combination of the Ramsey method with Double Quantum and Lock-in detection has enabled long-time real-time magnetic field measurements of over 600 seconds. Although the measured sensitivity was low at $3\,\mathrm{nT}/\sqrt{\mathrm{Hz}}$, the main noise sources and their magnitudes were analysed and countermeasures were proposed. This method is suitable for ecological magnetic field measurements, as the sensitivity can be further improved as T_2^* improves and the magnetic field can be detected in real-time.

Chapter 5

Conclusion and outlook

Biomagnetic fields are known to be more advantageous for identifying signal sources than those using bioelectric potentials, as the magnetic permeability is constant regardless of the biological tissue. However, the magnitude of the biomagnetic field is so small that it must be measured using a SQUID in a magnetically shielded room, and the use of SQUIDs has not become widespread despite their usefulness. Magnetic sensors based on NV centres in diamond are attracting attention as quantum sensors that are solid, operate at room temperature and pressure, and exhibit high linearity and high theoretical magnetic sensitivity.

At first, the author proposed a stable measurement system in which the biomagnetic field can be measured. The CW-ODMR method using laser noise cancellation and paired NV centres, combined with lock-in detection and feedback against temperature fluctuations, enabled a magnetic sensitivity of $140\,\mathrm{pT}/\sqrt{\mathrm{Hz}}$ and measurement times longer than one hour.

The author applied this measurement system to the measurement of rat cardiac magnetism and succeeded in the world's first biomagnetic measurement of rat cardiac magnetism using NV centres. Two-dimensional magnetic field imaging of cardiac magnetism was performed by changing the measurement position, and cardiac currents were successfully reconstructed. An antenna that can use a large sensor volume in this CW-ODMR method was proposed, and it was shown that a volume of $1\,\mathrm{mm}^3$ can be used as a sensor. These results will provide a guideline for biomagnetic field measurements using NV centres.

The CW-ODMR method is a simple method that can achieve a reasonable sensitivity with a simple configuration, but it has not been able to update the sensitivity of $15\,\mathrm{pT}/\sqrt{\mathrm{Hz}}$ achieved in 2016 [20]. Therefore, the author proposed to apply Double Quantum to the Ramsey method, which is expected to have higher sensitivity than the CW-ODMR method, and to combine it with lock-in detection. The author also proposed an antenna for the Ramsey method using Double Quantum, which requires the generation of a uniform and strong microwave magnetic field for biomagnetic measurements. The antenna differs from conventional loop-gap resonators [113] and dielectric resonators [104] in that the 111 diamond is placed close to the living body. Real-time magnetic field detection was successfully achieved using this antenna and a lock-in detection system that applies Double Quantum to the Ramsey method. The achieved magnetic field sensitivity is about $3\,\mathrm{nT}/\sqrt{\mathrm{Hz}}$, but its noise component is analysed and suggestions for improvement are presented. The Ramsey method is expected to improve sensitivity with longer T_2^*, and further improvement of sensitivity can be expected by improving the material. It is also possible to extend the T_2^* beyond the limit determined by the material by combining quantum protocols such as P1 decoupling.

For automotive applications, a 38 dB reduction in the common mode noise of the magnetic field has been reported by using two NV magnetometers in a gradiometer configuration [50]. Our company measured the magnetic field noise by actually driving a car, and found that a noise reduction of 80 dB is necessary to acquire the driver's magnetoencephalogram in a car. We are working on extracting the magnetoencephalography from the noisy environment by combining multiple NV magnetic field sensors configured as a gradiometer with AI.

Bibliography

[1] Milan Vošta and Aleš Kocourek. Competitiveness of the european automobile industry in the global context. *Politics in Central Europe*, 13:69–86, 2017.

[2] Tamitza Toroyan. Global status report on road safety. *Injury Prevention*, 15:286, 8 2009.

[3] World Health Organization. *Global status report on road safety 2018*. World Health Organization, 2018.

[4] . 2015-2016 , 2015.

[5] Ekim Yurtsever, Jacob Lambert, Alexander Carballo, and Kazuya Takeda. A survey of autonomous driving: Common practices and emerging technologies.

[6] Toshio Fujimura. ev 7 | pwc japan , 2018.

[7] Juan Guerrero-Ibáñez, Sherali Zeadally, and Juan Contreras-Castillo. Sensor technologies for intelligent transportation systems. *Sensors 2018, Vol. 18, Page 1212*, 18:1212, 4 2018.

[8] Arief Koesdwiady, Ridha Soua, Fakhreddine Karray, and Mohamed S Kamel. Recent trends in driver safety monitoring systems: State of the art and challenges. *IEEE Transactions on Vehicular Technology*, 66, 2017.

[9] Zehong Cao, Chun Hsiang Chuang, Jung Kai King, and Chin Teng Lin. Multi-channel eeg recordings during a sustained-attention driving task. *Scientific Data 2019 6:1*, 6:1–8, 4 2019.

[10] Yunchan Shin, Jeonggyun Ham, and Honghyun Cho. Investigation on thermal comfort using driver's bio-signals depend on vehicle cabin

and vent exit air temperature. *Journal of Mechanical Science and Technology 2019 33:7*, 33:3585–3596, 7 2019.

[11] Yaming Hu, Shun Nakamura, Tsuyoshi Yamanaka, and Toshihisa Tanaka. Physiological signals responses to normal and abnormal brake events in simulated autonomous car. *2019 Asia-Pacific Signal and Information Processing Association Annual Summit and Conference, APSIPA ASC 2019*, pages 736–740, 11 2019.

[12] Khald Ali I. Aboalayon, Miad Faezipour, Wafaa S. Almuhammadi, and Saeid Moslehpour. Sleep stage classification using eeg signal analysis: A comprehensive survey and new investigation. *Entropy 2016, Vol. 18, Page 272*, 18:272, 8 2016.

[13] Neil Schaul. The fundamental neural mechanisms of electroencephalography. *Electroencephalography and Clinical Neurophysiology*, 106:101–107, 2 1998.

[14] Marco Ferrari and Valentina Quaresima. A brief review on the history of human functional near-infrared spectroscopy (fnirs) development and fields of application. *NeuroImage*, 63:921–935, 11 2012.

[15] Matti Hämäläinen, Riitta Hari, Risto J. Ilmoniemi, Jukka Knuutila, and Olli V. Lounasmaa. Magnetoencephalography—theory, instrumentation, and applications to noninvasive studies of the working human brain. *Reviews of Modern Physics*, 65:413, 4 1993.

[16] D. Drung, C. Aßmann, J. Beyer, A. Kirste, M. Peters, F. Ruede, and Th Schurig. Highly sensitive and easy-to-use squid sensors. *IEEE Transactions on Applied Superconductivity*, 17:699–704, 6 2007.

[17] I. K. Kominis, T. W. Kornack, J. C. Allred, and M. V. Romalis. A subfemtotesla multichannel atomic magnetometer. *Nature 2003 422:6932*, 422:596–599, 4 2003.

[18] C. L. Degen. Scanning magnetic field microscope with a diamond single-spin sensor. *Applied Physics Letters*, 92:243111, 6 2008.

[19] J. M. Taylor, P. Cappellaro, L. Childress, L. Jiang, D. Budker, P. R. Hemmer, A. Yacoby, R. Walsworth, and M. D. Lukin. High-sensitivity diamond magnetometer with nanoscale resolution. *Nature Physics 2008 4:10*, 4:810–816, 9 2008.

[20] John F. Barry, Matthew J. Turner, Jennifer M. Schloss, David R. Glenn, Yuyu Song, Mikhail D. Lukin, Hongkun Park, and Ronald L. Walsworth. Optical magnetic detection of single-neuron action potentials using quantum defects in diamond. *Proceedings of the National Academy of Sciences of the United States of America*, 113:14133–14138, 12 2016.

[21] Dmitry Budker and Michael Romalis. Optical magnetometry. *Nature Physics 2007 3:4*, 3:227–234, 4 2007.

[22] MEGIN. Triux neo technical specifications, 2021.

[23] QuSpin. Qzfm gen-3, 2021.

[24] S. Steinert, F. Dolde, P. Neumann, A. Aird, B. Naydenov, G. Balasubramanian, F. Jelezko, and J. Wrachtrup. High sensitivity magnetic imaging using an array of spins in diamond. *Review of Scientific Instruments*, 81:043705, 4 2010.

[25] B. J. Maertz, A. P. Wijnheijmer, G. D. Fuchs, M. E. Nowakowski, and D. D. Awschalom. Vector magnetic field microscopy using nitrogen vacancy centers in diamond. *Applied Physics Letters*, 96:092504, 3 2010.

[26] Hannah Clevenson, Linh M. Pham, Carson Teale, Kerry Johnson, Dirk Englund, and Danielle Braje. Robust high-dynamic-range vector magnetometry with nitrogen-vacancy centers in diamond. *Applied Physics Letters*, 112:252406, 6 2018.

[27] C L Degen, F Reinhard, and P Cappellaro. Quantum sensing. 2017.

[28] J. H.N. Loubser and J. A. Van Wyk. Electron spin resonance in the study of diamond. *Reports on Progress in Physics*, 41:1201, 8 1978.

[29] V. M. Acosta, E. Bauch, M. P. Ledbetter, A. Waxman, L. S. Bouchard, and D. Budker. Temperature dependence of the nitrogen-vacancy magnetic resonance in diamond. *Physical Review Letters*, 104:070801, 2 2010.

[30] Neil B. Manson, Xing-Fei He, and Peter T. H. Fisk. Raman heterodyne detected electron-nuclear-double-resonance measurements of the nitrogen-vacancy center in diamond. *Optics Letters, Vol. 15, Issue 19, pp. 1094-1096*, 15:1094–1096, 10 1990.

[31] Neil B. Manson, Xing Fei He, and Peter T.H. Fisk. Raman heterodyne studies of the nitrogen-vacancy centre in diamond. *Journal of Luminescence*, 53:49–54, 1 1992.

[32] S. Felton, A. M. Edmonds, M. E. Newton, P. M. Martineau, D. Fisher, D. J. Twitchen, and J. M. Baker. Hyperfine interaction in the ground state of the negatively charged nitrogen vacancy center in diamond. *Physical Review B - Condensed Matter and Materials Physics*, 79:075203, 2 2009.

[33] Michael S.J. Barson, Phani Peddibhotla, Preeti Ovartchaiyapong, Kumaravelu Ganesan, Richard L. Taylor, Matthew Gebert, Zoe Mielens, Berndt Koslowski, David A. Simpson, Liam P. McGuinness, Jeffrey McCallum, Steven Prawer, Shinobu Onoda, Takeshi Ohshima, Ania C. Bleszynski Jayich, Fedor Jelezko, Neil B. Manson, and Marcus W. Doherty. Nanomechanical sensing using spins in diamond. *Nano Letters*, 17:1496–1503, 3 2017.

[34] Péter Udvarhelyi, V. O. Shkolnikov, Adam Gali, Guido Burkard, and András Pályi. Spin-strain interaction in nitrogen-vacancy centers in diamond. *Physical Review B*, 98:075201, 8 2018.

[35] A. Barfuss, M. Kasperczyk, J. Kölbl, and P. Maletinsky. Spin-stress and spin-strain coupling in diamond-based hybrid spin oscillator systems. *Physical Review B*, 99:174102, 5 2019.

[36] Matthew James Turner. *Quantum Diamond Microscopes for Biological Systems and Integrated Circuits*. PhD thesis, Harvard University, 2020.

[37] Connor Hart. *Experimental Realization of Improved Magnetic Sensing and Imaging in Ensembles of Nitrogen Vacancy Centers in Diamond*. PhD thesis, Harvard University, 2020.

[38] Eric Van Oort, Paul Stroomer, and Max Glasbeek. Low-field optically detected magnetic resonance of a coupled triplet-doublet defect pair in diamond. *Physical Review B*, 42:8605, 11 1990.

[39] Julia Michl, Jakob Steiner, Andrej Denisenko, André Bülau, André Zimmermann, Kazuo Nakamura, Hitoshi Sumiya, Shinobu Onoda, Philipp Neumann, Junichi Isoya, and Jörg Wrachtrup. Robust and accurate electric field sensing with solid state spin ensembles. *Nano Letters*, 19:4904–4910, 8 2019.

[40] Marcus W. Doherty, Neil B. Manson, Paul Delaney, Fedor Jelezko, Jörg Wrachtrup, and Lloyd C.L. Hollenberg. The nitrogen-vacancy colour centre in diamond. *Physics Reports*, 528:1–45, 7 2013.

[41] Lucio Robledo, Hannes Bernien, Toeno Van Der Sar, and Ronald Hanson. Spin dynamics in the optical cycle of single nitrogen-vacancy centres in diamond. *New Journal of Physics*, 13:025013, 2 2011.

[42] J. P. Tetienne, L. Rondin, P. Spinicelli, M. Chipaux, T. Debuisschert, J. F. Roch, and V. Jacques. Magnetic-field-dependent photodynamics of single nv defects in diamond: An application to qualitative all-optical magnetic imaging. *New Journal of Physics*, 14:103033, 10 2012.

[43] J. Harrison, M. J. Sellars, and N. B. Manson. Measurement of the optically induced spin polarisation of n-v centres in diamond. *Diamond and Related Materials*, 15:586–588, 4 2006.

[44] John F. Barry, Jennifer M. Schloss, Erik Bauch, Matthew J. Turner, Connor A. Hart, Linh M. Pham, and Ronald L. Walsworth. Sensitivity optimization for nv-diamond magnetometry. *Reviews of Modern Physics*, 92, 3 2020.

[45] Jennifer May. Schloss. *Optimizing nitrogen-vacancy diamond magnetic sensors and imagers for broadband sensitivity.* PhD thesis, Massachusetts Institute of Technology, 2019.

[46] Erik Bauch. *Optimizing Solid-State Spins in Diamond for Nano- to Millimeter-Scale Magnetic Field Sensing.* PhD thesis, Harvard University, 2018.

[47] A Dréau, M Lesik, L Rondin, P Spinicelli, O Arcizet, J.-F Roch, and V Jacques. Avoiding power broadening in optically detected magnetic resonance of single nv defects for enhanced dc magnetic field sensitivity. *PHYSICAL REVIEW B*, 84:195204, 2011.

[48] Hannah Clevenson, Matthew E. Trusheim, Carson Teale, Tim Schröder, Danielle Braje, and Dirk Englund. Broadband magnetometry and temperature sensing with a light-trapping diamond waveguide. *Nature Physics*, 11:393–397, 4 2015.

[49] K. Jensen, N. Leefer, A. Jarmola, Y. Dumeige, V. M. Acosta, P. Kehayias, B. Patton, and D. Budker. Cavity-enhanced room-temperature

magnetometry using absorption by nitrogen-vacancy centers in diamond. *Physical Review Letters*, 112:160802, 4 2014.

[50] Yuji Hatano, Jaewon Shin, Junya Tanigawa, Yuta Shigenobu, Akimichi Nakazono, Takeharu Sekiguchi, Shinobu Onoda, Takeshi Ohshima, Keigo Arai, Takayuki Iwasaki, and Mutsuko Hatano. High-precision robust monitoring of charge/discharge current over a wide dynamic range for electric vehicle batteries using diamond quantum sensors. *Scientific Reports 2022 12:1*, 12:1–10, 9 2022.

[51] H. Kanda. Large diamonds grown at high pressure conditions. *Braz. J. Phys.*, 30:482–489, 2000.

[52] Hisao Kanda, Minoru Akaishi, Nobuo Setaka, Sinobu Yamaoka, and Osamu Fukunaga. Surface structures of synthetic diamonds. *J. Mater. Sci.*, 15:2743–2748, 11 1980.

[53] Jennifer M Schloss, John F Barry, Matthew J Turner, and Ronald L Walsworth. Simultaneous broadband vector magnetometry using solid-state spins. *Physical Review Applied*, 10:34044, 2018.

[54] Tse Luen Wee, Yan Kai Tzeng, Chau Chung Han, Huan Cheng Chang, Wunshain Fann, Jui Hung Hsu, Kuan Ming Chen, and Eh Chung Yu. Two-photon excited fluorescence of nitrogen-vacancy centers in proton-irradiated type ib diamond. *J. Phys. Chem. A*, 111:9379–9386, 9 2007.

[55] Elisabeth Fraczek, Vasili G. Savitski, Matthew Dale, Ben G. Breeze, Phil Diggle, Matthew Markham, Andrew Bennett, Harpreet Dhillon, Mark E. Newton, and Alan J. Kemp. Laser spectroscopy of nv- and nv0 colour centres in synthetic diamond. *Opt. Mater. Express*, 7:2571, 7 2017.

[56] A Gupta, L Hacquebard, , and L Childress. Efficient signal processing for time-resolved fluorescence detection of nitrogen-vacancy spins in diamond. 2016.

[57] Bas J Boukens, Mark G Hoogendijk, Arie O Verkerk, Andre Linnenbank, Peter Van Dam, Carol-Ann Remme, Jan W Fiolet, Tobias Opthof, Vincent M Christoffels, and Ruben Coronel. Early repolarization in mice causes overestimation of ventricular activation time by the qrs duration.

[58] Chang S. Shin, Claudia E. Avalos, Mark C. Butler, David R. Trease, Scott J. Seltzer, J. Peter Mustonen, Daniel J. Kennedy, Victor M. Acosta, Dmitry Budker, Alexander Pines, and Vikram S. Bajaj. Room-temperature operation of a radiofrequency diamond magnetometer near the shot-noise limit. *J. Appl. Phys.*, 112:124519, 12 2012.

[59] James Luke Webb, Luca Troise, Nikolaj Winther Hansen, Christoffer Olsson, Adam M. Wojciechowski, Jocelyn Achard, Ovidiu Brinza, Robert Staacke, Michael Kieschnick, Jan Meijer, Axel Thielscher, Jean François Perrier, Kirstine Berg-Sørensen, Alexander Huck, and Ulrik Lund Andersen. Detection of biological signals from a live mammalian muscle using an early stage diamond quantum sensor. *Scientific Reports*, 11:1–11, 1 2021.

[60] Antti J. Mäkinen, Rasmus Zetter, Joonas Iivanainen, Koos C.J. Zevenhoven, Lauri Parkkonen, and Risto J. Ilmoniemi. Magnetic-field modeling with surface currents. part i. physical and computational principles of bfieldtools. *J. Appl. Phys.*, 128:063906, 8 2020.

[61] Rasmus Zetter, Antti J. Mäkinen, Joonas Iivanainen, Koos C.J. Zevenhoven, Risto J. Ilmoniemi, and Lauri Parkkonen. Magnetic field modeling with surface currents. part ii. implementation and usage of bfieldtools. *J. Appl. Phys.*, 128:063905, 8 2020.

[62] P Konopelski and M Ufnal. Electrocardiography in rats: a comparison to human. *Physiol. Res*, 65:717–725, 2016.

[63] Roy M. John, Usha B. Tedrow, Bruce A. Koplan, Christine M. Albert, Laurence M. Epstein, Michael O. Sweeney, Amy Leigh Miller, Gregory F. Michaud, and William G. Stevenson. Ventricular arrhythmias and sudden cardiac death. *The Lancet*, 380:1520–1529, 2012.

[64] Masatoshi Yamazaki, Haruo Honjo, Harumichi Nakagawa, Yuko S. Ishiguro, Yusuke Okuno, Mari Amino, Ichiro Sakuma, Kaichiro Kamiya, and Itsuo Kodama. Mechanisms of destabilization and early termination of spiral wave reentry in the ventricle by a class iii antiarrhythmic agent, nifekalant. *American Journal of Physiology - Heart and Circulatory Physiology*, 292:539–548, 1 2007.

[65] Michel Haïssaguerre, Dipen C. Shah, Pierre Jaïs, Morio Shoda, Josef Kautzner, Thomas Arentz, Dietrich Kalushe, Alan Kadish, Mike Griffith, Fiorenzo Gaïta, Teiichi Yamane, Stephane Garrigue, Meleze

Hocini, and Jacques Clémenty. Role of purkinje conducting system in triggering of idiopathic ventricular fibrillation. *Lancet*, 359:677–678, 2 2002.

[66] D Le Sage, K Arai, D R Glenn, S. J. Devience, L M Pham, L Rahn-Lee, M D Lukin, A Yacoby, A Komeili, and R L Walsworth. Optical magnetic imaging of living cells. *Nature*, 496:486–489, 2013.

[67] Thomas Wolf, Philipp Neumann, Kazuo Nakamura, Hitoshi Sumiya, Takeshi Ohshima, Junichi Isoya, and Jörg Wrachtrup. Subpicotesla diamond magnetometry. *Physical Review X*, 5:041001, 10 2015.

[68] D Le Sage, L M Pham, N Bar-Gill, C Belthangady, M D Lukin, A Yacoby, and R L Walsworth. Efficient photon detection from color centers in a diamond optical waveguide. *Physical Review B - Condensed Matter and Materials Physics*, 85:121202–121203, 2012.

[69] Zongmin Ma, Shaowen Zhang, Yueping Fu, Hua Yuan, Yunbo Shi, Jian Gao, Li Qin, Jun Tang, Jun Liu, and Yanjun Li. Magnetometry for precision measurement using frequency-modulation microwave combined efficient photon-collection technique on an ensemble of nitrogen-vacancy centers in diamond. *Optics Express*, 26:382, 1 2018.

[70] Jennifer T. Choy, Birgit J.M. Hausmann, Thomas M. Babinec, Irfan Bulu, Mughees Khan, Patrick Maletinsky, Amir Yacoby, and Marko Loňar. Enhanced single-photon emission from a diamond-silver aperture. *Nature Photonics*, 5:738–743, 10 2011.

[71] J. P. Hadden, J. P. Harrison, A. C. Stanley-Clarke, L. Marseglia, Y. L.D. Ho, B. R. Patton, J. L. O'Brien, and J. G. Rarity. Strongly enhanced photon collection from diamond defect centers under microfabricated integrated solid immersion lenses. *Applied Physics Letters*, 97:241901, 12 2010.

[72] L. Marseglia, J. P. Hadden, A. C. Stanley-Clarke, J. P. Harrison, B. Patton, Y. L.D. Ho, B. Naydenov, F. Jelezko, J. Meijer, P. R. Dolan, J. M. Smith, J. G. Rarity, and J. L. O'brien. Nanofabricated solid immersion lenses registered to single emitters in diamond. *Applied Physics Letters*, 98:133107, 3 2011.

[73] D Riedel, D Rohner, M Ganzhorn, T Kaldewey, P Appel, E Neu, R J Warburton, and P Maletinsky. Low-loss broadband antenna for

efficient photon collection from a coherent spin in diamond. *Physical Review Applied*, 2, 2014.

[74] Donggyu Kim, Mohamed I. Ibrahim, Christopher Foy, Matthew E. Trusheim, Ruonan Han, and Dirk R. Englund. A cmos-integrated quantum sensor based on nitrogen–vacancy centres. *Nature Electronics 2019 2:7*, 2:284–289, 7 2019.

[75] Kai Mei C. Fu, Geoffrey Z. Iwata, Arne Wickenbrock, and Dmitry Budker. Sensitive magnetometry in challenging environments. *AVS Quantum Science*, 2:044702, 12 2020.

[76] Connor A Hart, Jennifer M Schloss, Matthew J Turner, Patrick J Scheidegger, Erik Bauch, and Ronald L Walsworth. Nv-diamond magnetic microscopy using a double quantum 4-ramsey protocol. *Physical Review Applied*, 15:44020, 2021.

[77] Chen Zhang, Farida Shagieva, Matthias Widmann, Michael Kübler, Vadim Vorobyov, Polina Kapitanova, Elizaveta Nenasheva, Ruth Corkill, Oliver Rhrle, Kazuo Nakamura, Hitoshi Sumiya, Shinobu Onoda, Junichi Isoya, and Jörg Wrachtrup. Diamond magnetometry and gradiometry towards subpicotesla dc field measurement. *Physical Review Applied*, 15:064075, 6 2021.

[78] Yuji Hatano, Jaewon Shin, Daisuke Nishitani, Haruki Iwatsuka, Yuta Masuyama, Hiroki Sugiyama, Makoto Ishii, Shinobu Onoda, Takeshi Ohshima, Keigo Arai, Takayuki Iwasaki, and Mutsuko Hatano. Simultaneous thermometry and magnetometry using a fiber-coupled quantum diamond sensor. *Appl. Phys. Lett.*, 118:1–7, 1 2021.

[79] Yuki Nakano, Essam A. Rashed, Tatsuhito Nakane, Ilkka Laakso, and Akimasa Hirata. Ecg localization method based on volume conductor model and kalman filtering. *Sensors*, 21:4275, 7 2021.

[80] Robert W. Roudijk, Machteld J. Boonstra, Rolf Brummel, Wil Kassenberg, Lennart J. Blom, Thom F. Oostendorp, Anneline S.J.M. te Riele, Jeroen F. van der Heijden, Folkert W. Asselbergs, Peter M. van Dam, and Peter Loh. Comparing non-invasive inverse electrocardiography with invasive endocardial and epicardial electroanatomical mapping during sinus rhythm. *Front. Physiol.*, 12:730736, 10 2021.

[81] Hans Hallez, Bart Vanrumste, Roberta Grech, Joseph Muscat, Wim De Clercq, Anneleen Vergult, Yves D'Asseler, Kenneth P. Camilleri, Simon G. Fabri, Sabine Van Huffel, and Ignace Lemahieu. Review on solving the forward problem in eeg source analysis. *J. NeuroEng. Rehab.*, 4:46, 2007.

[82] Sandeep V. Pandit and José Jalife. Rotors and the dynamics of cardiac fibrillation. *Circ. Res.*, 112:849–862, 3 2013.

[83] Rebecca A.B. Burton, Aleksandra Klimas, Christina M. Ambrosi, Jakub Tomek, Alex Corbett, Emilia Entcheva, and Gil Bub. Optical control of excitation waves in cardiac tissue. *Nat. Photonics*, 9:813–816, 11 2015.

[84] L. A. Geddes and L. E. Baker. The specific resistance of biological material—a compendium of data for the biomedical engineer and physiologist. *Med. Biol. Engng.*, 5:271, 5 1967.

[85] H Ahrens. The inverse problem of magnetocardiography.

[86] Wonryung Lee, Shingo Kobayashi, Masase Nagase, Yasutoshi Jimbo, Itsuro Saito, Yusuke Inoue, Tomoyuki Yambe, Masaki Sekino, George G. Malliaras, Tomoyuki Yokota, Masaru Tanaka, and Takao Someya. Nonthrombogenic, stretchable, active multielectrode array for electroanatomical mapping. *Sci. Adv.*, 4:2426, 10 2018.

[87] Christopher O'Shea, James Winter, S. Nashitha Kabir, Molly O'Reilly, Simon P. Wells, Olivia Baines, Laura C. Sommerfeld, Joao Correia, Ming Lei, Paulus Kirchhof, Andrew P. Holmes, Larissa Fabritz, Kashif Rajpoot, and Davor Pavlovic. High resolution optical mapping of cardiac electrophysiology in pre-clinical models. *Sci. Data*, 9:135, 12 2022.

[88] Christopher O'Shea, S. Nashitha Kabir, Andrew P. Holmes, Ming Lei, Larissa Fabritz, Kashif Rajpoot, and Davor Pavlovic. Cardiac optical mapping – state-of-the-art and future challenges. *Int. J. Biochem. Cell Biol.*, 126:105804, 9 2020.

[89] Christopher O'Shea, Andrew P. Holmes, James Winter, Joao Correia, Xianhong Ou, Ruirui Dong, Shicheng He, Paulus Kirchhof, Larissa Fabritz, Kashif Rajpoot, and Davor Pavlovic. Cardiac optogenetics and optical mapping – overcoming spectral congestion in all-optical cardiac electrophysiology. *Front. Physiol.*, 10:182, 2019.

[90] J. L. Cox, R. B. Schuessler, H. J. D'Agostino, C. M. Stone, B. C. Chang, M. E. Cain, P. B. Corr, and J. P. Boineau. The surgical treatment of atrial fibrillation iii. development of a definitive surgical procedure. *J. Thorac. Cardiovasc. Surg.*, 101:569, 1991.

[91] Shoji Kawakami, Hiroshi Takaki, Shuji Hashimoto, Yoshitaka Kimura, Takahiro Nakashima, Takeshi Aiba, Kengo F. Kusano, Shiro Kamakura, Satoshi Yasuda, and Masaru Sugimachi. Utility of high-resolution magnetocardiography to predict later cardiac events in non-ischemic cardiomyopathy patients with normal qrs duration. *Circ. J.*, 81:44, 2017.

[92] Erik Bauch, Connor A Hart, Jennifer M Schloss, Matthew J Turner, John F Barry, Pauli Kehayias, Swati Singh, and Ronald L Walsworth. Ultralong dephasing times in solid-state spin ensembles via quantum control. 2018.

[93] I. Lovchinsky, A. O. Sushkov, E. Urbach, N. P. De Leon, S. Choi, K. De Greve, R. Evans, R. Gertner, E. Bersin, C. Muller, L. McGuinness, F. Jelezko, R. L. Walsworth, H. Park, and M. D. Lukin. Nuclear magnetic resonance detection and spectroscopy of single proteins using quantum logic. *Science*, 351:836–841, 2 2016.

[94] B. J. Shields, Q. P. Unterreithmeier, N. P. De Leon, H. Park, and M. D. Lukin. Efficient readout of a single spin state in diamond via spin-to-charge conversion. *Phys. Rev. Lett.*, 114:136402, 3 2015.

[95] L. M. Pham, D. Le Sage, P. L. Stanwix, T. K. Yeung, D. Glenn, A. Trifonov, P. Cappellaro, P. R. Hemmer, M. D. Lukin, H. Park, A. Yacoby, and R. L. Walsworth. Magnetic field imaging with nitrogen-vacancy ensembles. *N. J. Phys.*, 13:045021, 4 2011.

[96] D. A. Broadway, S. E. Lillie, S. C. Scholten, D. Rohner, N. Dontschuk, P. Maletinsky, J. P. Tetienne, and L. C.L. Hollenberg. Improved current density and magnetization reconstruction through vector magnetic field measurements. *Phys. Rev. Appl.*, 14:024076, 8 2020.

[97] Khadijeh Bayat, Jennifer Choy, Mahdi Farrokh Baroughi, Srujan Meesala, and Marko Loncar. Efficient, uniform, and large area microwave magnetic coupling to nv centers in diamond using double split-ring resonators. *Nano Letters*, 14:1208–1213, 3 2014.

[98] Ning Zhang, Chen Zhang, Lixia Xu, Ming Ding, Wei Quan, Zheng Tang, and Heng Yuan. Microwave magnetic field coupling with nitrogen-vacancy center ensembles in diamond with high homogeneity. *Applied Magnetic Resonance*, 47:589–599, 6 2016.

[99] Y. Masuyama, K. Mizuno, H. Ozawa, H. Ishiwata, Y. Hatano, T. Ohshima, T. Iwasaki, and M. Hatano. Extending coherence time of macro-scale diamond magnetometer by dynamical decoupling with coplanar waveguide resonator. *Review of Scientific Instruments*, 89:125007, 12 2018.

[100] Andrew Horsley, Patrick Appel, Janik Wolters, Jocelyn Achard, Alexandre Tallaire, Patrick Maletinsky, and Philipp Treutlein. Microwave device characterization using a widefield diamond microscope. *PHYSICAL REVIEW APPLIED*, 10:44039, 2018.

[101] Felix M. Stürner, Andreas Brenneis, Thomas Buck, Julian Kassel, Robert Rölver, Tino Fuchs, Anton Savitsky, Dieter Suter, Jens Grimmel, Stefan Hengesbach, Michael Förtsch, Kazuo Nakamura, Hitoshi Sumiya, Shinobu Onoda, Junichi Isoya, and Fedor Jelezko. Integrated and portable magnetometer based on nitrogen-vacancy ensembles in diamond. *Advanced Quantum Technologies*, 4:2000111, 4 2021.

[102] B C Rose, A M Tyryshkin, H Riemann, N V Abrosimov, P Becker, H.-J Pohl, M L W Thewalt, K M Itoh, and S A Lyon. Coherent rabi dynamics of a superradiant spin ensemble in a microwave cavity.

[103] Jonathan D. Breeze, Enrico Salvadori, Juna Sathian, Neil McN. Alford, and Christopher W. M. Kay. Continuous-wave room-temperature diamond maser. *Nature 2018 555:7697*, 555:493–496, 3 2018.

[104] P Kapitanova, V V Soshenko, V V Vorobyov, D Dobrykh, S V Bolshedvorskii, V N Sorokin, and A V Akimov. 3d uniform manipulation of nv centers in diamond using a dielectric resonator antenna 1, 2. *JETP Letters*, 108:588–595, 2018.

[105] Andreas Angerer, Thomas Astner, Daniel Wirtitsch, Hitoshi Sumiya, Shinobu Onoda, Junichi Isoya, Stefan Putz, and Johannes Majer. Collective strong coupling with homogeneous rabi frequencies using a 3d lumped element microwave resonator. *Applied Physics Letters*, 109:033508, 7 2016.

[106] Jason R. Ball, Yu Yamashiro, Hitoshi Sumiya, Shinobu Onoda, Takeshi Ohshima, Junichi Isoya, Denis Konstantinov, and Yuimaru Kubo. Loop-gap microwave resonator for hybrid quantum systems. *Applied Physics Letters*, 112:204102, 5 2018.

[107] W. N. Hardy and L. A. Whitehead. Split-ring resonator for use in magnetic resonance from 200-2000 mhz. *Review of Scientific Instruments*, 52:213–216, 6 1981.

[108] Maddalena Violetti, Matthieu Pellaton, Christoph Affolderbach, Francesco Merli, Jean François Zürcher, Gaetano Mileti, and Anja K. Skrivervik. The microloop-gap resonator: A novel miniaturized microwave cavity for double-resonance rubidium atomic clocks. *IEEE Sensors Journal*, 14:3193–3200, 2014.

[109] W. Froncisz and James S. Hyde. The loop-gap resonator: a new microwave lumped circuit esr sample structure. *Journal of Magnetic Resonance (1969)*, 47:515–521, 5 1982.

[110] Tokuyuki Teraji, Takashi Yamamoto, Kenji Watanabe, Yasuo Koide, Junichi Isoya, Shinobu Onoda, Takeshi Ohshima, Lachlan J. Rogers, Fedor Jelezko, Philipp Neumann, Jörg Wrachtrup, and Satoshi Koizumi. Homoepitaxial diamond film growth: High purity, high crystalline quality, isotopic enrichment, and single color center formation. *Physica Status Solidi (A) Applications and Materials Science*, 212:2365–2384, 11 2015.

[111] Adam M. Wojciechowski, Alexander Huck, Haitham A. R. El-Ella, Sepehr Ahmadi, and Ulrik L. Andersen. Optimised frequency modulation for continuous-wave optical magnetic resonance sensing using nitrogen-vacancy ensembles. *Optics Express, Vol. 25, Issue 13, pp. 14809-14821*, 25:14809–14821, 6 2017.

[112] Kento Sasaki, Yasuaki Monnai, Soya Saijo, Ryushiro Fujita, Hideyuki Watanabe, Junko Ishi-Hayase, Kohei M. Itoh, and Eisuke Abe. Broadband, large-area microwave antenna for optically detected magnetic resonance of nitrogen-vacancy centers in diamond. *Review of Scientific Instruments*, 87:053904, 5 2016.

[113] E. R. Eisenach, J. F. Barry, L. M. Pham, R. G. Rojas, D. R. Englund, and D. A. Braje. Broadband loop gap resonator for nitrogen vacancy centers in diamond. *Review of Scientific Instruments*, 89:094705, 9 2018.

[114] Lahcen Yechou, Abdelwahed Tribak, Mohamed Kacim, Jamal Zbitou, and Angel Mediavilla Sanchez. A novel wideband bandpass filter using coupled lines and t-shaped transmission lines with wide stop-band on low-cost substrate. *Progress In Electromagnetics Research C*, 67:143–152, 2016.